Turbulent Noise Sources in Vocal Tract Models

by

Leah Marie Pfeifer Pastel

B.S., Cornell University (1980)
M.S., Rensselaer Polytechnic Institute (1983)

Submitted to the department of
Electrical Engineering and Computer Science
in partial fulfillment of
the requirements for the degrees of

Electrical Engineer

and

Master of Science

at the

Massachusetts Institute of Technology

October, 1987

©Leah Marie Pfeifer Pastel, 1987

The author hereby grants to MIT permission to reproduce and
to distribute copies of this thesis document in whole or part.

Signature of Author .....
Department of Electrical Engineering and Computer Science
October 19, 1987

Certified by .....
Kenneth N. Stevens
Clarence J. LeBel Professor of Electrical Engineering
Thesis Supervisor

Accepted by ..
Arthur C. Smith
Chairman, Department Committee on Graduate Students

MASSACHUSETTS INSTITUTE
OF TECHNOLOGY

MAR 2 2 1988

LIBRARIES
Archives

Turbulent Noise Sources in Vocal Tract Model

by

Leah Marie Pfeifer Pastel

Submitted to the Department of Electrical Engineering and Computer Science on October 19, 1987 in partial fulfillment of the requirements for the degrees of Master of Science and Electrical Engineer.

Abstract

Turbulent noise sources produced in the vocal tract during frication and aspiration were studied. The objectives of this thesis were to characterize the noise sources and their distribution in the vocal tract during aspiration. A series of mechanical models of the vocal tract articulatory configuration of the speech sound /h/ followed by the vowel /ɹ/ or /ɑ/ were constructed. The models differed in the entry angle of the air flow at the mode inlet (jet angle) and in the presence of and location of an obstacle inside the tube representing the vocal tract. Radiated sound pressure at a distance of 26 cm from the mouth of each model was recorded and processed using an averaged periodogram algorithm.

The vocal tract was considered from acoustic and aerodynamic points of view. For the frequency range of interest, only uniform plane waves propagate in the vocal tract. The vocal tract was modeled acoustically as a linear distributed system, mathematically analogous to electrical transmission line circuits. The aerodynamics of noise source production was included in the analysis by introducing distributed sound sources into the transmission line network. Flow-obstacle interactions create dipole sources within the vocal tract model. A dipole can be modeled as series pressure (voltage) source in the transmission line circuit for the frequency range under consideration. The vocal tract was assumed to be passive and source-tract interactions were assumed not to exist. The radiated sound pressure at a distance of 26 cm from the mouth of each model was related to the sound pressure source produced at a particular location inside of the model. From this analysis, the spectra of pressure sources produced under different conditions of jet angle and longitudinal location in the model were calculated from the experimental data for each model.

The spectrum of an /h/-like sound was determined by modeling the distribution of pressure sources within the vocal tract for the speech sound /h/ preceding /ɹ/ or /ɑ/. The spectra of the pressure sources produced during aspiration were represented by the previously derived source spectra from the 27° jet angle models. The sound pressure radiated due to the sources was then calculated.

Thesis supervisor: Kenneth N. Stevens, Sc.D.
Title: Clarence J. LeBel Professor of Electrical Engineering

To Paul for his patience and humor.

Acknowledgements

I would like to thank Ken Stevens for his advice, encouragement, and friendship while I was working on this thesis. I especially appreciate his talent of making me think for myself and his patience listening to the results.

I am grateful for the technical support of the Speech Communications Group as well as their willingness to discuss technical questions. In particular, I would like to thank Keith North for providing technical assistance, advice, and equipment all at a moment's notice. Thanks also to Joe Perkell for sharing equipment, which was in heavy demand.

Thanks to Bill Rabinowitz for his time and help.

I would like to thank Abeer Alwan, Corine Bickley, Marc Cohen, Wil Howitt, Caroline Huang, Ann Forestell, Sharon Manuel, John Pitrelli, Carol Ringo, Marie Southwick, and Rohit Vishnoi for their support. Marc Cohen deserves special thanks for his help editing the first three chapters of this thesis.

Thanks to Chris Shadle not only for the example her research provided, but for her help and advice.

Thanks to Peter and Lois Norton for laser printing the final draft of this thesis.

I especially wish to thank Paul, my husband, for his unfailing support and for his wizardry on the MacIntosh computer, converting many of my hand drawn figures to computer drawings.

Finally, thanks to NIH for funding this project under grant NS 04322.

Contents

Abstract 2

Acknowledgements 4

List of Figures 7

List of Tables 9

List of Symbols 10

1 Introduction and Background

1.1 Introduction 12
1.2 Theory of Jets 13
1.3 Acoustic Sources Produced by Turbulent Flow 21
1.4 Source-Tract Model 22
1.5 Modeling Aspiration and Frication 24
1.6 Fluid Mechanics References 30
1.7 Plan of Thesis 30

2 A Jet in a Tube: Acoustic Measurements

2.1 Introduction 32
2.2 Materials, Methods and Calibration 32
2.3 Experimental Procedure: Pressure Sources at Obstacle 38
2.4 Results: Pressure Sources at Obstacle 40
2.5 Experimental Procedure: Dipole Orientation 49
2.6 Results: Dipole Orientation 49
2.7 Discussion 51

3 Theoretical Analysis of Vocal Tract Models

3.1 Aerodynamic Analysis of Vocal Tract Models 58

3.2 Acoustic Analysis of Mechanical Models 62

3.3 Analysis of the Corrected Data 73

3.4 Discussion 80

4 /h/-like Sound Spectra

4.1 The Speech Sound /h/ 86

4.2 Calculation of /h/-like Spectrum 87

4.3 Discussion 90

5 Conclusions 93

Appendix A: Calibration Set-ups and Curves 95

Appendix B: Tables of Data, Transfer Functions and Source Spectra 101

Bibliography 108

List of Figures

1.1 Schematic of a free jet 14
1.2 The impinging jet: flow regions and velocity profiles. 17
1.3 Pressure and velocity in the impingement zone. 18
1.4 The intersection of a jet and its image. 19
1.5 Nearby walls affect the entrainment of a jet. 20
1.6 A schematic fluid switching device. 20
1.7 The vocal tract and equivalent pressure source models. 23
1.8 Flow regions in the vocal tract (uniform tube). 25
1.9 Pressure and volume velocity envelopes. 26
1.10 Coupling of a pressure source in a tube. 27
1.11 Dipole directivity pattern in units of radiated power. 28
1.12 The anatomy of the vocal tract. 29
2.1 System block diagrams. 33
2.2 Air line system and mechanical model. 33
2.3 Constriction geometries. 35
2.4 90° jet inlet. 36
2.5 Annular obstacle. 36
2.6 Air line inlet structure. 39
2.7 Data for the 0° jet angle configuration. 41
2.8 Data for the 10° jet angle configuration. 42
2.9 Data for the 19° jet angle condiguration. 43
2.10 Data for the 27° jet angle condiguration. 44
2.11 Data for the 90° jet angle condiguration. 45
2.12 Determination of the distributed source region of F4 in the 0° jet models. 47
2.13 Distributed source regions and maxima. 48
2.14 0° and 90° tube configurations. 49
2.15 Radiated sound pressure for 0° and 90° configurations. 50
2.16 Differences in SPL for configurations with respect to the 0° jet. no-obstacle model. 51
2.17 Radiated sound pressure peak magnitude versus jet angle. 52

2.18 Positions of inlet monopole and free jet quadrupoles. 54

2.19 Difference in SPL for the 90° configuration corrected for coupling loss with respect to the 0° jet no-obstacle model 56

2.20 Spectral density due to normal dipole sources produced in the 0° configuration. 57

3.1 Free jet axial velocity and half radius. 59

3.2 Angled jet impact. 60

3.3 General model of the vocal tract. 63

3.4 An incremental length of transmission line 64

3.5 Complex pole - zero plane. 66

3.6 Inlet circuit and model. 70

3.7 Source spectra for 0° jet models. 77

3.8 Source spectra for the 10° jet models. 78

3.9 Source spectra for19° jet models 79

3.10 Source spectra for 27° jet models 79

3.11 Source spectra for 90° jet models 80

3.12 Comparison of the source spectra of Shadle's model and the 0° jet model. 82

3.13 Source spectra peak magnitude versus jet angle. 83

3.14 Source spectra data for F1 versus axial source location. 84

3.15 Source spectra data for F2 versus axial source location. 84

3.16 Source spectra data for F3 versus axial source location. 85

3.17 Source spectra data for F4 versus axial source location. 85

4.1 The glottal jet superimposed on a sagittal view of the larynx. 88

4.2 Dimensions of the glottal region of an adult male. 89

4.3 Modeled Source Spectra. 90

4.4 Radiated sound pressure versus frequency due to pressure sources located at different axial positions along the tract. 91

4.5 /h/-like Spectra. 92

A.1 Flowmeter circuit for calibration. 95

A.2 Schematic of the system and microphone/mixer calibration set-up. . 97

A.3 The relationship between tone frequencies recorded and played . . . 98

A.4 The system offset curve. 99

A.5 The frequency response of the microphone and mixer. 100

List of Tables

3.1 Impingement zone velocities using effective height. 61
3.2 Poles and bandwidths for the mechanical models. 68
3.3 Zeroes and Bandwidths for the mechanical models. 72
3.4 Average magnitude (dB SPL in 50 Hz bins) for the no-obstacle models. 73
B.1 Corrected Data, 0° jet models, magnitude (dB SPL in 50 Hz bins). . . 101
B.2 Corrected Data, 10° jet models, magnitude (dB SPL in 50 Hz bins). . 102
B.3 Corrected Data, 19° jet models, magnitude (dB SPL in 50 Hz bins). . 102
B.4 Corrected Data, 27° jet models, magnitude (dB SPL in 50 Hz bins). . 103
B.5 Corrected Data, 90° jet models, magnitude (dB SPL in 50 Hz bins). . 103
B.6 Log magnitude $|T_i'(f)|$ (dB). 104
B.7 Log magnitude source spectra, $|S_i(f)|$ (dB), 0° jet models. 104
B.8 Log magnitude source spectra, $|S_i(f)|$ (dB), 10° jet models. 105
B.9 Log magnitude source spectra, $|S_i(f)|$ (dB), 19° jet models. 105
B.10 Log magnitude source spectra, $|S_i(f)|$ (dB), 27° jet models. 106
B.11 Log magnitude source spectra, $|S_i(f)|$ (dB), 90° jet models. 106
B.12 Parameters of regression fits to source spectra. 107

List of Symbols

c	Speed of sound, 34480 cm/s for dry air (1 atmos, 23°C).
ν	Kinematic viscosity of air, = 0.156 cm^2/sec.
ρ	Density of dry air, = 1.19×10^{-3} g/cm^3 (1 atmos, 23°C).
f	Frequency
Δf	Bandwidth
ω	Angular frequency
s	Complex frequency
M	Mach number, dimensionless speed normalized to c.
γ	Complex wavenumber
k	Wavenumber, = ω/c.
Re	Reynolds number, dimensionless constant of flow.
p	Pressure different from ambient pressure.
P	Complex amplitude of differential pressure, p.
P_s	Complex amplitude of a series pressure source.
U	Volume velocity different from ambient volume flow velocity.
A	Cross-sectional area of a tube or opening.
$S(\omega)$	Complex magnitude of the spectrum of a pressure source.
$R(\omega)$	Complex radiation characteristic
$T(\omega)$	Transfer function between a source in the tract and the volume velocity at the mouth of the tract or tube.
Z	Complex magnitude of impedance, = P/U.
Z_0	Characteristic impedance of a tube of area A, = $\rho c/A$.
R	Resistance of a tube (may represent a per unit length quantity); also correlation coefficient.
G	Conductance per unit length of a tube.
L	Inductance per unit length of a tube.
C	Capacitance of a tube (may represent a per unit length quantity); also an empirical flow constant.
l	Length of a section of tubing or transmission line.
Q	Quality factor, a measure of the sharpness of a resonance.
θ	Angle between the axes of the tube and jet.

z	Axial distance from the nozzle.
r	Radial distance from the jet axis; also distance between the mouth of the tube and the microphone.
z_c	Distance the airflow travels up to the point where the mixing zone completely covers the jet core.
$r_{1/2}$	Half radius, the transverse distance between the jet axis and the point where the axial velocity has been halved for a round jet.
U_o	Initial jet volume velocity at the nozzle.
u_o	Initial jet velocity at the nozzle.
$u(\cdot)$	Axial jet velocity.
$v(\cdot)$	Radial jet velocity.
h	Distance from a nozzle of an impinging jet to the impact surface.
δ_o	Boundary layer thickness.
/f/	Unvoiced labiodental fricative as in the bold part of **life**.
/v/	Voiced labiodental fricative as in the bold part of **live**.
/θ/	Unvoiced dental fricative as in the bold part of **thigh**.
/ð/	Voiced dental fricative as in the bold part of **thee**.
/s/	Unvoiced alveolar fricative as in the bold part of **sea**.
/z/	Voiced alveolar fricative as in the bold part of **zeal**.
/ʃ/	Unvoiced palatal fricative as in the bold part of **shore**.
/ʒ/	Voiced palatal fricative as in the bold part of **azure**.
/x/	Unvoiced velar fricative as in the bold part of the German word **ach**.
/h/	Unvoiced glottal fricative or aspiration as in the bold part of **hand**.
/ʌ/	Back unrounded vowel as in the bold part of **but**.
/ə/	Mid-central unstressed vowel as in the bold parts of **about** and **famous**.
vh	When used as a subscript, refers to viscous and heat conduction losses.
R, r	When used as subscripts, refer to radiation loss.
n	When used as a subscript, refers to mode number (ie. F_n); also refers to radiation loss when used in this context Δf_n.
cg	When used as a subscript, refers to losses at the glottal constriction.
c	When used as a subscript, refers to the glottal constriction.
tot	When used as a subscript, refers to the net total of the quantity in question.

Chapter 1
Introduction and Background

1.1 Introduction

Speech sounds can be classified into a number of distinct and mutually exclusive groups. These groups comprise the basic linguistic units of a language and are called phonemes. Although one speaker may pronounce a phoneme differently from another speaker, the meaning perceived by a native listener of the language will be the same. There is some speaker variation in the acoustic manifestations of a particular phoneme. Individual tokens of a phoneme spoken by a single speaker may vary acoustically depending on the context and speed of their delivery. Each phoneme, however, has its own set of articulatory parameters, which describe the position and shape of the articulators, such as the jaw and tongue, when the phoneme is spoken. There exist acoustic correlates of the articulatory patterns or vocal tract configurations [Fant, 1960; Stevens, 1972].

Phonemes can be grouped into several broad classes which describe the kind of acoustic correlates necessary to differentiate them. For example, vowels and consonants make up the most familar classes and exist to some extent in all languages. Consonants can be broken down into several manner classes, distinguished by the mechanism of sound production, such as fricatives (including /h/), stops, nasals, glides and semivowels. Fricatives are produced by a noise excitation in the vocal tract. The noise is generated by turbulent air flow from a constriction in the vocal tract. Often the air flow strikes an obstacle in its path such as the teeth, resulting in an increased amplitude of the noise source. The objectives of this thesis are to learn about these noise sources and their distribution in the vocal tract.

Important linguistic features of fricatives are the place of articulation, the voiced or voiceless distinction, and the strident or mellow distinction [Fant, 1960; Flanagan, 1972]. The place of articulation describes the location of the constriction in the vocal tract. For example, the fricatives with labiodental place of articulation are /v/ and /f/. Their constriction is located between the upper teeth and lower lip. They can be differentiated from each other by the voiced-unvoiced feature: /v/ has a periodic glottal source due to vibration of the vocal cords in addition to the noise sources of /f/. Therefore, /v/ is voiced and /f/ is unvoiced. If a consonant is voiced, at least part of the vocal folds are vibrating, producing a harmonic volume velocity source located at the glottis opening.

Turbulent noise sources are produced by a jet of air passing through the glottis or a more anterior constriction. If the source is in the vicinity of the glottis, it is called aspiration; noise produced at a constriction in the vocal tract is called frication noise. A

turbulent jet of air contains eddies, where velocity fluctuates relative to the ambient flow velocity. These fluctuations generate free sound sources near the constriction, as well as producing fluctuating forces on the vocal tract walls and at obstacles, such as the teeth and lips, and these forces may also generate sound. In the production of strident fricatives, an obstacle is placed in the air stream providing a large random noise source. Strident fricatives have a large amount of high frequency energy, while mellow fricatives have weaker energy and usually a wider frequency distribution. For example, compare the word "breeze" containing [+ strident] /ʒ/ with "breathe" containing [- strident] /ð/ [Jakobson, 1969; Catford, 1977].

In order to understand more fully the mechanisms of sound production during aspiration and frication, it is necessary to have some knowledge of jets and the flows associated with them.

1.2 Theory of Jets

A jet occurs whenever there is a fluid stream moving at a different velocity from the surrounding fluid. A tangential separation surface delineates the boundary between the different flows. Flows may differ in several variables such as flow velocity, temperature and chemical composition. The flows we are interested in differ in velocity. Turbulent eddies form in the flow due to instabilities in the flow. Eddies penetrate the flow separation surface thus mixing the two flows and creating a boundary layer between them. The boundary layer is a transition region between the flows. Flow variables are exchanged across the boundary layer, widening it as more fluid is incorporated in to it. This process is called entrainment [Abramovich, 1963]. Figure 1.1a illustrates a free jet. The cross hatched region marks the associated boundary layer. Through entrainment, the boundary layer moves in toward the center of the jet until the entire core has been consumed. The distance the flow travels up to the point where the mixing zone completely covers the jet core is defined as the core length z_c. At z_c, the jet core has been replaced by fully turbulent flow. From the nozzle to this point, the axial velocity in the jet is constant [Hinze, 1959]. At distances greater than z_c, the boundary layer absorbs the surrounding fluid, widening the jet. z_c has been determined empirically for many jet flow situations.

Jet characteristics are very well behaved when represented by time averaged or by bulk averaged quantities. Most engineering results are from empirical studies. No one definitive theory exists for all boundary layer flow problems, though there are several theories which are good for particular geometries of flow. If the jet is entering a still medium, the boundary layers meet, having completely swallowed the core approximately

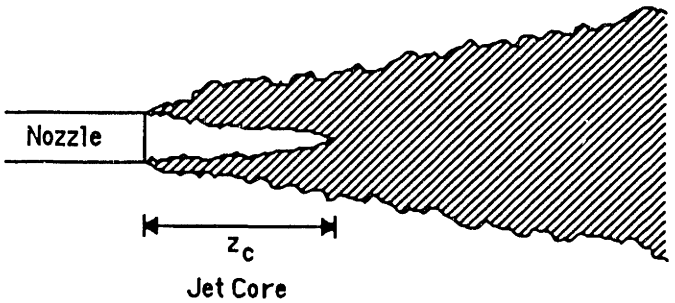

a)

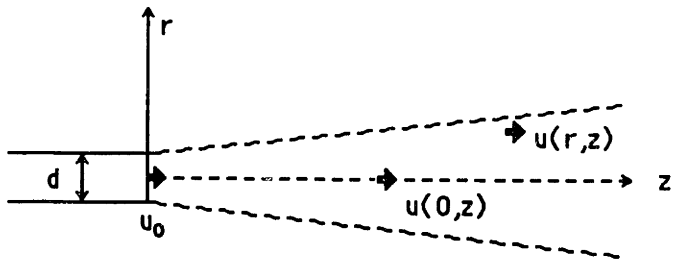

b)

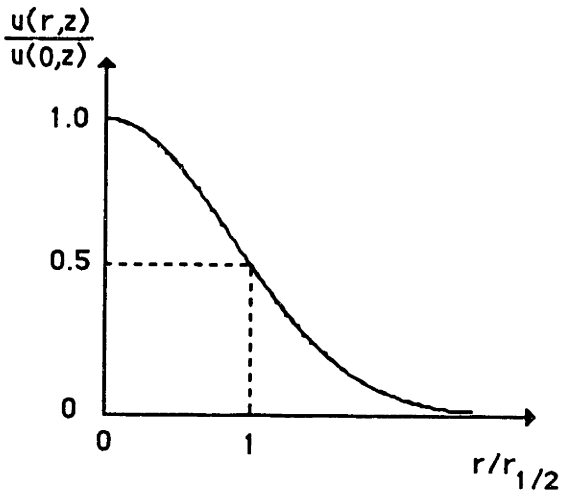

c)

Figure 1.1 A free jet.
a) Schematic of a free jet. The shaded region indicates the boundary layer associated with this jet. b) Geometry and variables used in analyzing a free jet. u(r,z) is the axial velocity of the fluid located at the points (r,z) in the jet. c) Example of the velocity profile across a free jet at location z. u(r,z) and r are normalized by u(0,z) and $r_{1/2}$, the half radius, respectively.

four to eight nozzle diameters from the nozzle [Hinze,1959]. For a well rounded jet nozzle or planar jet nozzle, the core length is usually four diameters or four slit widths long, respectively [Martin, 1977]. The jet width is often characterized by the transverse distance between the jet axis and the point where the axial velocity has been halved. For a round jet, this distance is the half radius, $r_{1/2}$. For a planar jet, it is called the halfwidth, b. Flow from a planar jet can be typified as the flow from a long slit and b is defined as the halfwidth in the dimension across the slit. For a rectangular opening of area A, the jet width may be roughly approximated from $r_{1/2}$ of a round jet of nozzle diameter $d = 2\ [A/\pi]^{1/2}$ [Beranek, 1986].

A fluid flow problem can often be described by characteristic variables such as characteristic lengths, time constants, or characteristic frequencies. The flow can be scaled by its characteristic variables to provide a dimensionless description of the flow. Many flow situations scaled in this way result in the same description even though the original variables may be many orders of magnitude different. When scaling results in the same dimensionless description, the flows are said to be similar. The usefulness of dimensionless analysis can be seen in the following example. A civil engineer would like to test his design for a long pier to be built on an ocean bay. Building the project to test the design is costly and may be embarrassing. Instead a model of the bay can be designed which has the same dimensionless description, but is constructed with different characteristic variables. His project is built on the scale of the new characteristic lengths, so proportions are retained. The pattern of water flow is created using the characteristic time constants and flow dimensions scaled in the same way. Dimensionless constants such as Reynolds number are preserved.

Jets of different sizes scale through dimensionless analysis. In addition, they are also self-preserving or similar along their main axes, such that dimensionless profiles taken at different axial locations of the jet will be identical. When the jet has become fully developed, two things begin to happen: one, the axial velocity begins to decay; two, the jet becomes appreciably wider. The width increases linearly as a function of z, the axial distance from the nozzle. These events are related to one another and result in flow patterns that have similar consecutive sections. Plots of axial velocity versus transverse distance from the axis normalized to axial velocity on the axis and halfwidth respectively, will overlay each other for various axial distances from the nozzle. The empirical relationships amongst these parameters for a round jet can be written in several forms. Hinze cites the following equations for axial velocity and $r_{1/2}$:

$$\frac{u(z)}{u_o} = \frac{z_c}{z} \qquad ,\text{for } z > z_c$$

$$\frac{2\,r_{1/2}}{d} = \frac{z}{z_c}$$

where u_o is the initial jet velocity and u(z) the on-axis jet velocity a distance z from the nozzle [Hinze, 1959]. Martin cites the following equations for free jet flow from a round nozzle:

$$\frac{u(0,z)}{u_o} = \{\, 1 - \exp[-(\frac{d/z}{\sqrt{2}\,C})^2]\,\}^{1/2} \qquad ,z \geq 0$$

$$\frac{u(r,z)}{u(0,z)} = \exp[-(\frac{r}{Cz})^2]$$

where r is the radial distance from the jet axis and C is a constant defined by setting z equal to the core length and setting the pressure drop over z_c to 95% of the total pressure drop which is equivalent to $\{u(0,z_c)/u_o\}^2 = 0.95$. For a core length of four diameters, C = 0.102 [Martin, 1977]. The relationship between the variables used in these equations and the free jet geometry is shown in figure 1.1.

The flow associated with one or more jets colliding with a surface is called impinging flow. Momentum and force balance equations for an impinging water jet in air can be solved in a straightforward manner for the force exerted on the surface by the jet and the volume velocites of the resultant flows. The density difference between water and air makes such solution possible by allowing certain terms in the equations to be neglected. Equations for an air into air jet retain these terms and are much more difficult to solve [Streeter, 1962]. All impinging jet flows, however, can be divided up into the same three regions: 1) the free jet region, 2) the impingement zone or region of stagnation flow and 3) the wall jet region [Martin, 1977; Russell and Hatton, 1972]. Figure 1.2 is a schematic diagram indicating the flow regions and representative velocity profiles for the case of a single round or planar jet impinging perpendicularly on a flat surface. The free jet region is that part of the flow which can be described by a free jet and is not influenced by the surface. A free jet has been described earlier in this chapter.

In the impingement zone or region of stagnation flow, the normal velocity component is decelerated and channeled into an accelerated parallel component. This flow occurs relatively close to the surface. For a single round jet, the region may begin as close as 1.2

nozzle diameters above the surface [Martin, 1977]. Stagnation occurs at the point where velocity becomes zero; maximum pressure occurs at this point. If the jet is angled in

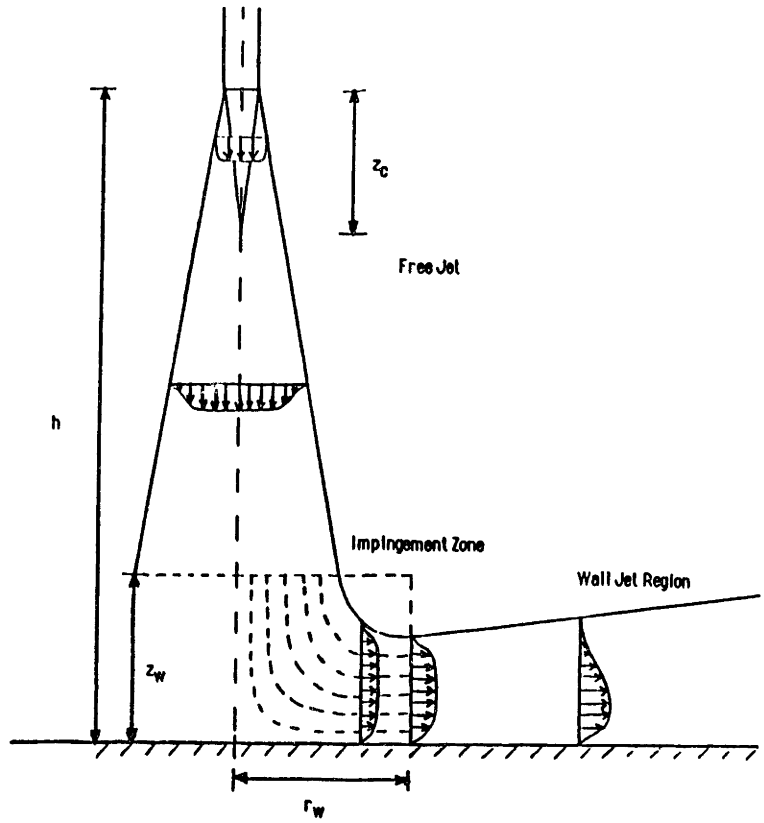

Figure 1.2 The impinging jet.
The flow regions and typical velocity profiles are indicated. z_c is the core length of the free jet. h is the minimum distance between the jet nozzle and the impact surface. The spatial extent of the impingement zone of a perpendicular impinging jet is indicated by z_w and r_w. z_w is the perpendicular distance from the surface to the point in space where the jet is first influenced by the surface. r_w is the radial distance from the jet axis to the beginning of the wall jet. After [Martin,1977; Russell and Hatton, 1972].

relation to the surface, a stagnation line may actually occur, rather than a single stagnation point [Birkhoff and Zarantonello, 1957]. Figure 1.3 shows schematically the relationship between dimensionless pressure, $p/(\rho u_0^2/2)$ and dimensionless velocity, u/u_0 in the impingement zone and indicates the point of stagnation in the flow. The boundary layer next to the wall is very thin relative to other flow dimensions. The viscosity of air does not greatly affect the shape of the velocity profile except at the surface of the wall where the no slip condition is in effect. The no slip condition states that at the boundary between a solid and a fluid, the fluid must have the same velocity as the surface of the solid. For example, if the solid is at rest, the fluid must also be at rest. The velocity components outside the wall boundary layer and the boundary layer thickness for axisymmetric flow are given by

$$u(z) = 2a_R z'$$
$$v(r) = a_R r$$
$$\delta_o = 1.95\ (\nu/a_R)^{1/2}$$

where z' is the perpendicular distance from the impact surface to a point within the impingement zone and r is the radial distance measured from the stagnation point, u(z') and v(r) are the axial and radial velocities, respectively, δ_o is the boundary layer thickness, and a_R is an empirically derived constant. A formula for a_R has been found for the case (h/d ≤10), where h is the minimum distance from surface to nozzle [Martin, 1977].

$$a_R = (u_o/d)(1.04 - 0.034h/d)$$

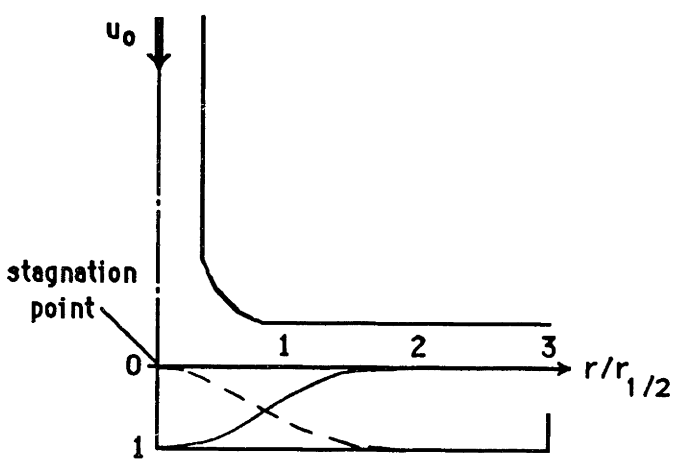

Figure 1.3 Pressure, p and velocity, u in the impingement zone.
Dimensionless pressure and velocity profiles are shown for the case of an impinging perpendicular jet. The jet is schematically represented by the curved line, which indicates the boundary layer on the right side of the jet. The impact surface is superimposed on the $r/r_{1/2}$ axis. u_o is the jet inlet velocity. $r_{1/2}$ is the half radius of the jet at the surface location if no surface was present. (u/u_o - - - · $p/\rho u_o^2/2$ ——) After [Rouse, 1959].

The velocity component parallel to the wall accelerates from zero reaching a maximum at the impingement zone-wall jet boundary, labeled r_w in figure 1.2. As the flow moves from the impingement zone to the wall jet region, the boundary layer near the wall and the flow velocity change markedly. The acceleration stabilizes the boundary layer at the wall producing laminar flow in the layer until maximum radial velocity is reached. Then the layer transitions to a turbulent boundary layer in the wall jet and the velocity begins to

decrease [Martin, 1977]. For axisymmetric flow, the resulting wall jet can be visualized by the intersection of two jets as pictured in figure 1.4. A wall jet is formally defined as the flow produced "by ejecting fluid along a solid surface bounding a fluid at rest or in uniform motion" [Reynolds, 1974]. The velocity of the wall jet decelerates towards zero inversely with the distance traveled from the stagnation point.

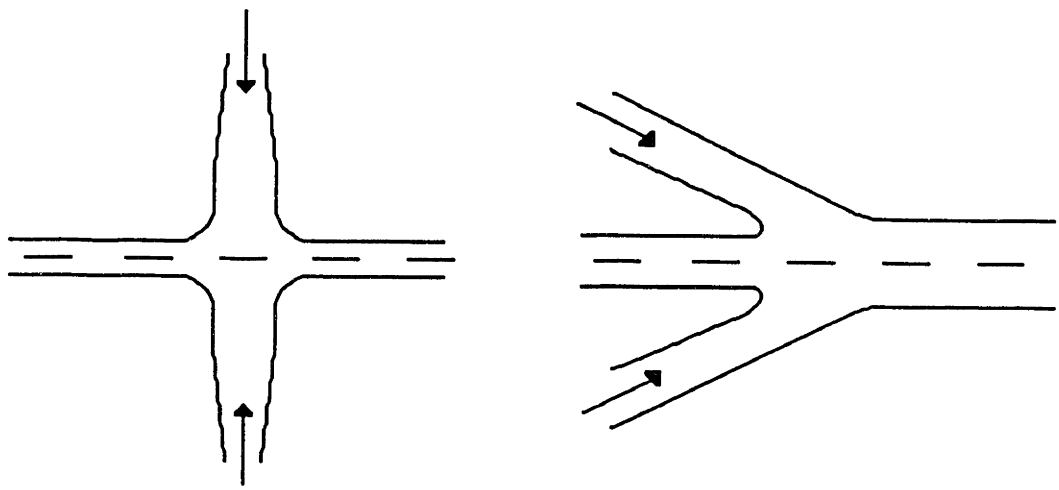

Figure 1.4 Impinging jets. The intersection of the jet and its image can be used to construct the flow due to a jet and a flat surface.

A wall jet may form from a flow either parallel to or at a shallow angle to the wall. A jet will be attracted to a nearby wall through an entrainment-attraction mechanism. Figure 1.5 illustrates these flows. If on one side of the jet there is an unlimited amount of fluid to be captured by the jet, while on the other side there is not, recirculation will result upstream and the jet will bend towards the wall. A demonstration can be made by placing a finger near a stream of water from a faucet [Reynolds, 1974]. In the context of a jet entering a tube, a wall jet will only form downstream of the attachment. It probably will not remain centered in the tube, since a small difference in entrainment will shift the jet off-center. If a finger is placed on either side of a stream of water, the flow spreads between the fingers attaching to both; however, it is very difficult to balance the stream between the fingers. In addition, the curvature of the surface placed near the jet will influence the attachment. For instance, a wall jet will readily adhere to a convex surface, but it will separate from a concave surface. The position of a jet can be controlled by adjusting the amounts of flow and fluid in recirculation areas and placing properly curved surfaces near the jet. Fluid switching devices, such as the one pictured in figure 1.6, are constructed using these principles [Reynolds, 1974]. These devices are used to channel a

jet in a desired direction. Additional fluid can be added to the jet from either side through the flow control ports. By increasing or decreasing the amount of fluid available for entrainment on either side of the jet, control can be exerted on the position of the jet in the pipe. The jet will move in the direction of decreased entrainment for unbalanced control flows.

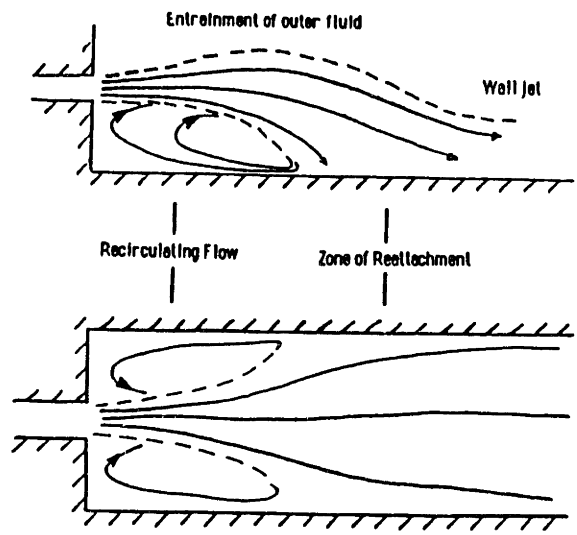

Figure 1.5 Nearby walls affect the entrainment of a jet, causing recirculation regions to form.

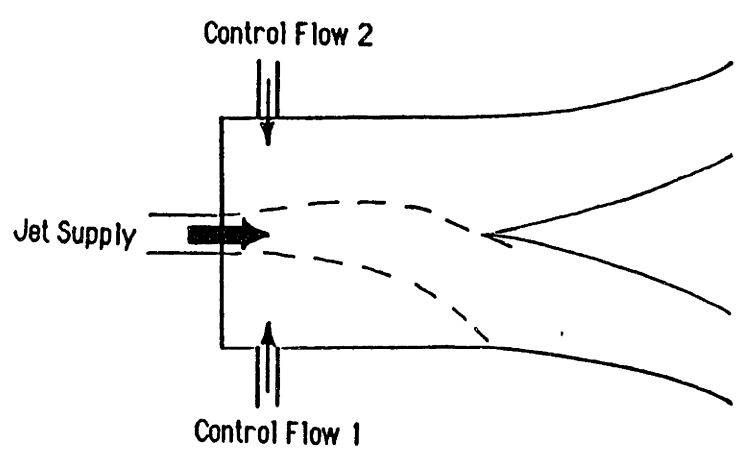

Figure 1.6 A schematic fluid switching device. After [Reynolds, 1974].

1.3 Acoustic Sources Produced by Turbulent Flow

Sound produced by turbulent flow may be represented by a combination of three different idealized sound sources. They are simple sources or monopoles, dipoles and quadrupoles. A monopole is a compact spherical source which alternately expands and contracts isotropically. A dipole is made up of two monopoles relatively close together pulsing in opposite phase. As one monopole releases mass the other absorbs it. A net dipole implies a fluctuating force with no net change in mass. A quadrupole is an arrangement of four monopoles. It has no net change in mass and zero net force, but it does have a net moment. A monopole exists where a net fluctuation in mass occurs such as at the nozzle of a jet. Dipole sources occur at hard boundaries, while quadrupoles exist in free turbulence such as that of a free jet. The sound produced by a jet impinging on a surface or obstacle may be modeled by dipole and quadrupole sources [Dyer, 1986; Morse and Ingard, 1968; Shadle, 1985].

The radiated sound power due to a source depends on how well it converts kinetic energy into sound per unit time. The ratio of acoustic power to mechanical power is defined as acoustic efficiency. The efficiencies of conversion for monopole, dipole, and quadrupole sources are M, M^3, and M^5, respectively, where M is the Mach number. For subsonic speeds, $M > M^3 > M^5$. In order of decreasing relative magnitude, the sources are monopole, dipole, and quadrupole [Morse and Ingard, 1968; Ribner, 1964].

Turbulent flows have a wide range of length and frequency scales representing the size of turbulent disturbances. Energy transfers occur between different scales of turbulence. The largest scale corresponds to the width of the flow. Basically, the energy extracted from the initial flow velocity creates broad low frequency fluctuations in velocity and pressure. The extracted energy fuels the maintenance and growth of turbulence. The largest scale fluctuations are therefore determined by the mean flow velocity. Smaller and more local high frequency events arise from interference between large scale disturbances. These small scale events dissipate the energy they extract through viscous effects or channel it into smaller events. The scale of the smallest fluctuations is determined by the viscosity of the fluid [Reynolds, 1974].

In a jet, high frequency fluctuations decay more quickly than low frequency ones, and thus they are damped out closer to the nozzle of the jet. Spectra of turbulence taken farther from the nozzle have less high-frequency and more low-frequency energy relative to spectra at closer locations [Shadle, 1985]. For a jet, the highest frequency component of turbulence introduced at the nozzle is on the order of c/d, where c is the speed of sound and d the nozzle diameter. It has been found, for a jet in an organ pipe, that disturbances grow

most rapidly when their wavelength is about six times the jet width. If the wavelength is less than the width of the jet, it does not grow and may decay. As the jet widens, high frequency components in the turbulence die out [Thwaites and Fletcher, 1979, 1980, 1982, 1983]. The rate of decay depends on the presence of boundaries and the viscosity of the fluid. The spectra for a particular axial location in the jet are generally convex in shape with less energy at high and very low frequencies. The spectral energy shifts toward low frequencies in jet spectra for locations farther downstream from the nozzle.

1.4 Source-Tract Model

Most speech sounds are produced by air flowing through the vocal tract. In order to analyze the acoustic properties corresponding to articulatory parameters, a model of the vocal tract must be formulated. The vocal tract can be considered from an acoustic or from an aerodynamic view point. For the audio frequency range, the vocal tract can be modeled acoustically as a linear distributed system, mathematically analogous to electrical transmission line circuits. The aerodynamics of noise source production can be included in the model by introducing distributed sound sources into the tract network. In this model, the tract is passive and there is no source-tract interaction [Fant, 1960; Stevens, 1987].

For frequencies from 0 Hz to approximately 8000 Hz and dimensions on the order of the adult human vocal tract (15 to 17 cm in length and 60 cm^3 in volume), the vocal tract supports one-dimensional sound fields equivalent to uniform plane wave propagation. The variables, p (pressure different from ambient pressure) and U (volume velocity different from ambient volume flow velocity) behave as voltage and current on a transmission line. Thus the vocal tract may be modeled as a transmission line circuit with an input impedance equal to the glottis impedance and a load impedance equal to the radiation impedance. The cross-sectional area function of the vocal tract is incorporated in the model by breaking the circuit into segments of transmission line each with a characteristic impedance inversely proportional to the area of the vocal tract it represents. Turbulence produces a fluctuating force on obstacle surfaces, and the resulting sound sources can be modeled by a distribution of dipoles. For frequencies below the first cross mode, a dipole can be represented by two opposing current sources separated by an acoustic mass or inductance. The circuit can be replaced by a series pressure source equivalent to the pressure drop across the acoustic mass. Turbulent sound sources may be modeled as series pressure (voltages) sources on a transmission line. Figure 1.7 shows a representative tract and its circuit. The sound pressure due to a distributed sound source in the model can be found by solving the circuit with several locations of series pressure sources and summing the results.

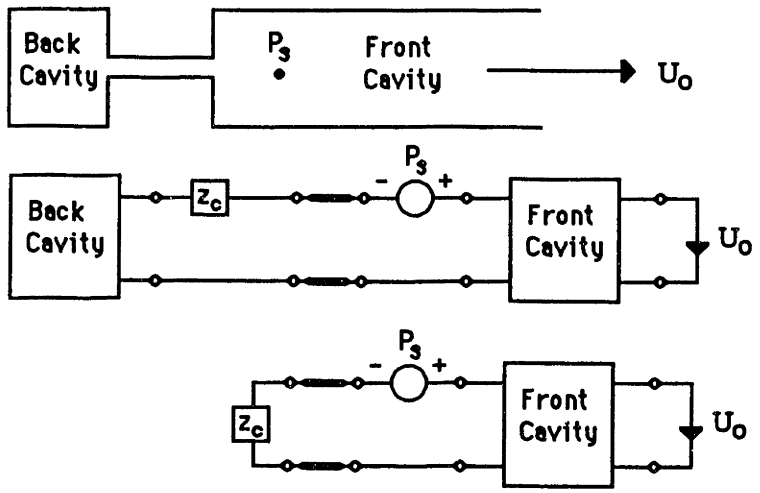

Figure 1.7 A sample vocal tract configuration and equivalent pressure source models. The last circuit is valid where the constriction is small enough to ignore back cavity effects. Z_C represents the impedance of the constriction between back and front cavities. P_S is the series pressure source and U_O is the volume velocity at the mouth of the tube.

The sound pressure at a point in space located a distance from the mouth of the tube can be calculated by specifying the source spectra $S(\omega)$, the transfer function from source to volume velocity at the mouth of the tube or load on the transmission line (i.e. the coupling function) $T(\omega)$, and the radiation characteristic $R(\omega)$. The sound pressure at a distance from the mouth of the tube $P(\omega)$ is related to the source by

$$P(\omega) = S(\omega)\, T(\omega)\, R(\omega) \quad \text{[Fant, 1960].}$$

Sound pressure spectra recorded at a distance from a mechanical model can be related back to the sound source distribution by using an approximation of the radiation characteristic and the transfer function which relates the pressure source in a tube to the volume velocity at the mouth of the tube. Often a point source approximation for sound radiation from the mouth of the tube is used, but a more accurate approximation could be used as well. The pressure source can be calculated from

$$S(\omega) = P(\omega) / R(\omega)\, T(\omega).$$

The model of the vocal tract and turbulent noise sources provides a good frame of

reference in which to study the noise produced by a jet in a mechanical model and make some predictions about it. A uniform tube is chosen as it is the simplest system to investigate. The model allows freedom to change the jet orientation to the tube's main axis and to introduce obstacles or microphones into the tube without having to take into consideration a complicated cross-sectional area function.

1.5 Modeling Aspiration and Frication

For aspiration or frication, the airstream can be modeled as a turbulent jet with Reynolds number greater than 2000. Reynolds number, Re, is a dimensionless constant used in flow analysis and gives a measure of the turbulence of the flow. There are several other dimensionless constants similar to Reynolds number which indicate the relative importance of certain terms in the Navier-Stokes equations describing flow. These constants are the basis of dimensionless analysis. Reynolds number for a round pipe is

$$Re = 4\,U/\pi\nu d$$

where U is the volume velocity of the flow, ν the kinematic viscosity, and d the pipe diameter [Reynolds, 1974]. For a uniform tube with dimensions on the order of an adult vocal tract, the flow produced at the glottis or at an anterior constriction of similar size has a turbulent Re. However, the flow at the mouth of the tube usually does not. For instance during aspiration, flow from the glottis opening has a Re of about 9000 for $U = 440\ cm^3/sec$, $\nu = 0.156\ cm^2/sec$ and $d = 0.4$ cm. Re at the mouth is usually less than 2000. From the glottis or constriction to the tube mouth, the flow passes through several stages. These are depicted in figure 1.8. The airstream enters the tube and becomes fully turbulent within a few nozzle diameters of the inlet. The jet grows until it is wide enough to be influenced by tube walls or it encounters an obstacle. How far down the tube this occurs depends on the orientation of the jet to the tube and on the curvature of the tube. As the jet broadens, its velocity decreases until it can no longer feed enough energy to the turbulent fluctuations to offset energy dissipating processes. At this point, the turbulent fluctuations that occur are damped out within a short distance of their origins and the flow becomes laminar. If the length of the tube between the constriction and the mouth is short enough, this point is not reached. In this case, flow is still somewhat turbulent at the tube mouth and can be represented by a monopole source located there.

Due to the anatomy of the vocal tract, surfaces and obstacles are oriented at different

angles to the jet and are located in different parts of the jet. A fluctuating force at the surface or obstacle face can be resolved into a shear force component and a perpendicular component. The magnitude of the resulting pressure source depends on the proportion of these two components and the location of the interaction in the jet. Surface sources are produced at the edges of the jet profile along the wall, where the jet has spread away from its main axis and has lost velocity, assuming that the nozzle is in the middle of the tube. Obstacles more often protude into the main jet stream where velocity is higher and the source magnitude is proportional to the the cross-sectional area interacting with the jet. Sound sources also exist within the free jet portion of the flow. These sources are modeled as quadrupole sources and for subsonic air speeds are weaker than the dipole sources produced at obstacles in the jet [Morse and Ingard, 1968]. In the source-tract model, the free quadrupoles can be represented as a distributed line source, coupling into the tract like a volume velocity source [Shadle, 1985]. Turbulent sources do not move with the flow and therefore are confined to a particular volume of the tube.

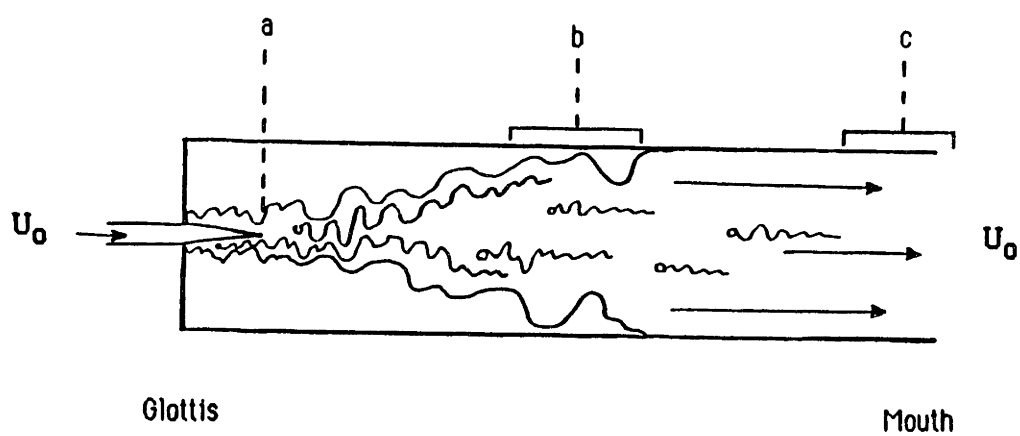

Figure 1.8 Flow regions in the vocal tract (uniform tube).
a) Jet core has become fully turbulent
b) Jet broadens and is influenced by boundaries
c) Turbulence is damped out-laminar flow results.

A transfer function can be found between a source in the tract and the volume velocity at the tract mouth, $T(\omega)$. This is the source coupling function. One may estimate how well a mode will couple to the radiated sound field by considering the pressure or volume velocity standing wave pattern in the tract for that frequency. In figure 1.9, the pressure and

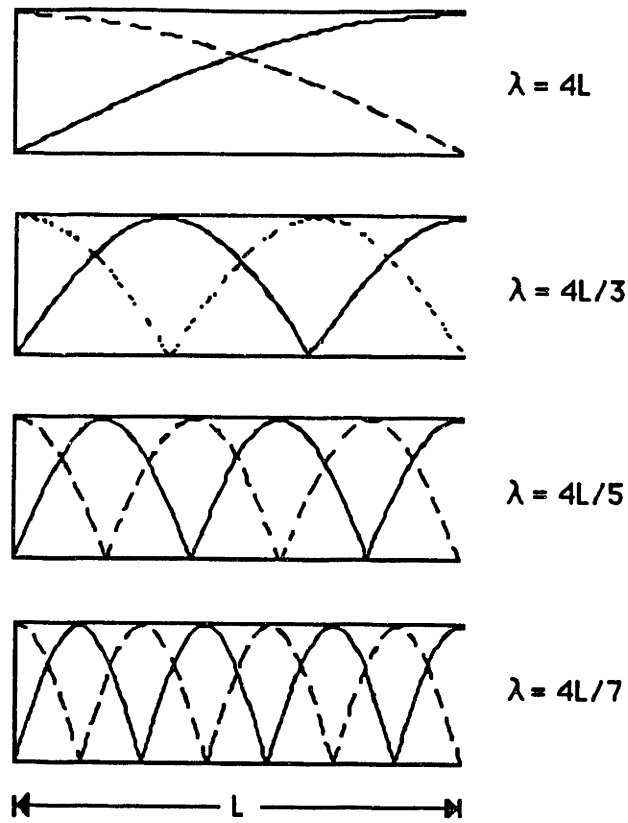

Figure 1.9: Pressure, p, and volume velocity, U, envelopes for the first four resonant frequencies in an ideal tube, where λ is the wavelength and L is the tube length. (p is - - -, U is ——).

volume velocity envelopes for the first few resonant frequencies are shown. The energy density of a certain mode depends on the power in the standing waves of the mode, which is proportional to the product pU, differential pressure times differential volume velocity [Staelin and Kong, 1985]. For instance, the local volume velocity determines how well a pressure source will convert mechanical power to acoustic power and the local pressure on how well a volume velocity source will do the same. If a pressure source with a uniform power spectrum is placed at the glottis end of the tract, little sound will be produced because a null in volume velocity is located there for all frequencies. On the other hand, a volume velocity source placed at the glottis will couple at all frequencies equally, since pressure is maximum there. The pressure source located in the tube in figure 1.10 will couple well at frequencies where the volume velocity is near a maximum and not so well near a null in volume velocity. The radiated sound pressure resulting from it will contain the first resonant frequency and not the second [Shadle, 1985; Stevens, 1987].

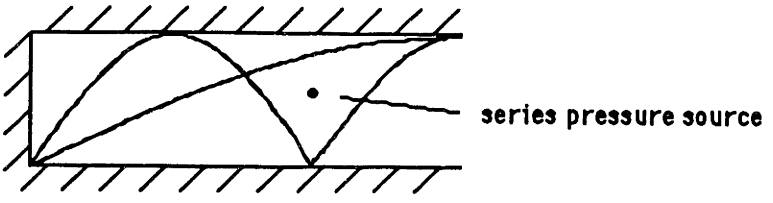

Figure 1.10 Coupling of a pressure source in a tube.
The source couples well to the first mode , but is located at a null in the second mode volume velocity standing wave and does not couple well.

The sound pressure due to a complicated source can be represented mathematically by the sum of sound pressures due to a combination of simple sources. The sound pressure at a point in space due to a complicated source depends on the source's orientation to and distance from the point. The spatial dependence of the sound pressure field is depicted by the directivity pattern. For example, a dipole source (a combination of two monopoles) has the directivity pattern shown in figure 1.11. A dipole oriented perpendicularly to the axis of a tube will not couple into the longitudinal plane wave modes of the tube. But if it is rotated by 90°, it will couple completely [Morse and Ingard, 1968]. The orientations of dipoles that make up a pressure source determine how well the sources will couple to the plane wave modes of the tube.

In order to model actual fricative configurations, knowledge of vocal tract anatomy and articulatory configuration are important. The vocal tract is not a straight uniform tube. It has some overall curvature from glottis to mouth and it has compliant walls. The jaw and tongue can be used to modulate the cross-sectional area of the tract, although the volume remains fairly constant in all configurations.

Fricatives can be grouped according to where the constriction is placed in the tract:

labiodental -- between a lip and teeth (/f/, /v/)
dental -- between the teeth and tongue (/θ/, /ð/)
alveolar -- between the gum ridge and tongue (/z/, /s/)
palatal -- between the hard palate and tongue (/ʒ/, /ʃ/)
velar -- between soft palate and tongue (/x/)
glottal -- between the vocal cords (/h/).

A small constriction in any of these regions of the vocal tract may decouple the acoustics of the vocal tract on either side of the constriction. To a first approximation, the length of the

front part of the tract determines the first pole of the transfer function not associated with a pole-zero pair. As the constriction moves forward in the tract, the frequency of the pole becomes higher. For example, for a vocal tract with a length of about 17 cm, the first pole is located at about 500 Hz for /h/ and at about 4000 Hz for /s/ [Stevens, 1971]. Anatomical structures in front of the constriction may be responsible for important sources of additional sound when a jet of air interacts with these structures.

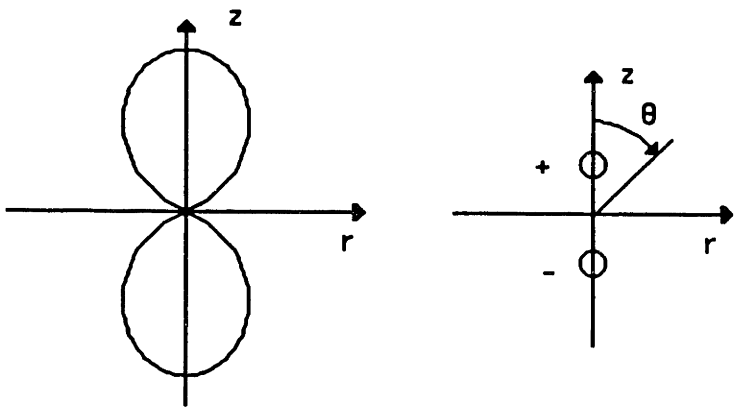

Figure 1.11 Dipole directivity pattern in units of radiated power. The radiated power is proportional to $\cos^2 \theta$ and the z-axis is an axis of rotational symmetry.

Different regions of the vocal tract present different structures for possible interaction with turbulent flow. Figure 1.12 illustrates these structures. Near the glottis, the vestibular fold or false vocal folds can protrude into the turbulent flow as can the tip of the epiglottis. For palatal and velar fricatives, air impinges on the wall of the vocal tract at a greater angle due to the curvature of the tract in that region. The alveolar and labiodental portions of the tract contain a wealth of flow obstacles such as the tongue, teeth and lips. The sound sources produced by frication at an obstacle and in the free jet are the subject of C. H. Shadle's Ph. D. Thesis, MIT March 1985. The sources produced at the wall are the topic of this thesis.

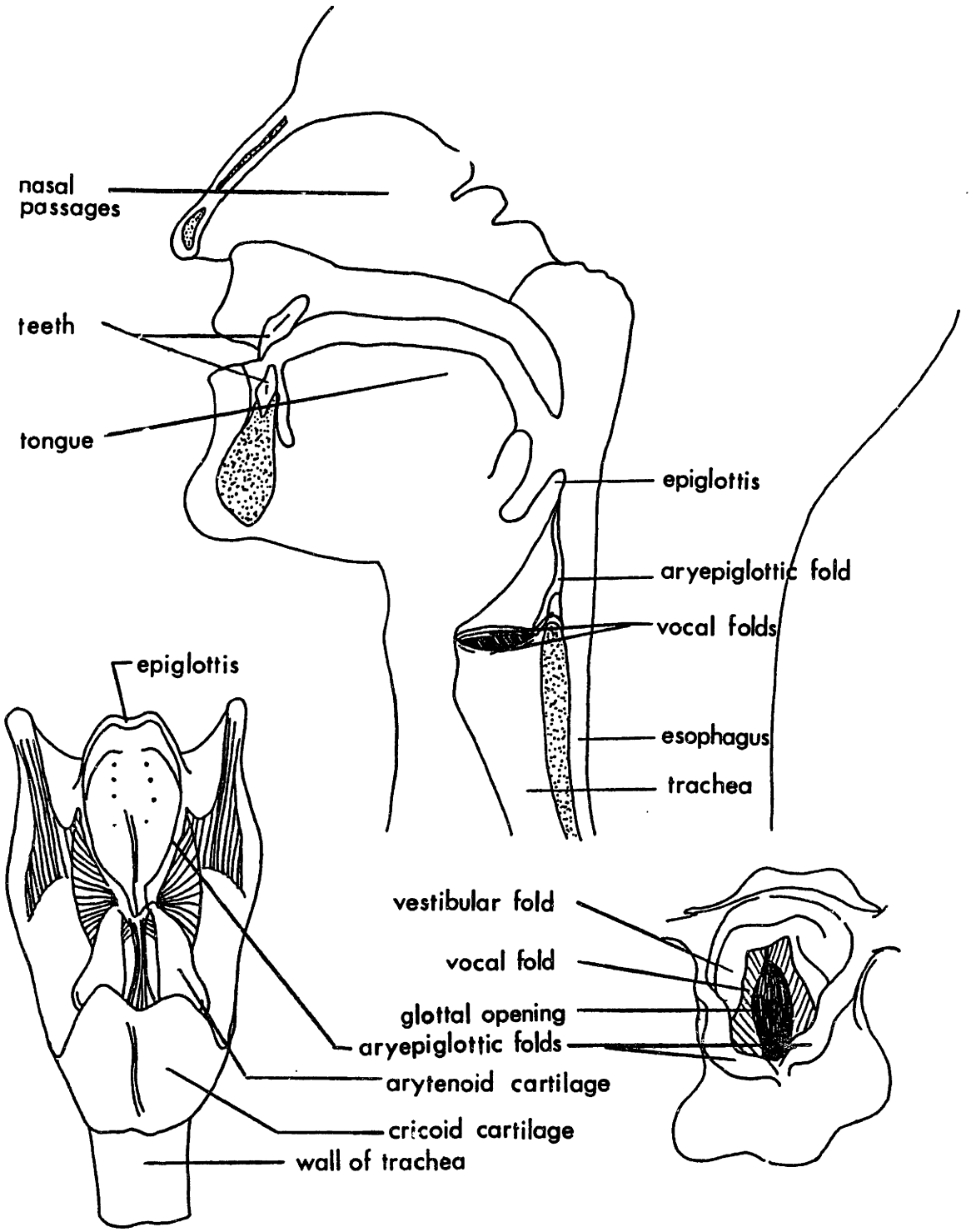

Figure 1.12 The anatomy of the vocal tract.

1.6 Fluid Mechanics References

In the course of this study, the following references to research in the fluid mechanics literature have been used. These sources are mentioned here with a brief description.

"Heat and Mass Transfer between Inpinging Gas Jets and Solid Surfaces": H. Martin discusses heat and mass transfer using gas jets. There is also a short, but clear and complete description of the hydrodynamics of impinging flow included at the beginning of his article [Martin, 1977].

"A Review of Experimental Data of Uniform Density Free Turbulent Boundary Layers": W. Rodi has compiled a complete review of empirical data on free turbulent boundary layers including free jets, wakes, and mixing layers. The article also contains a discussion of the reliability of the data and identification of the most reliable data for each type of flow [Rodi, 1975].

"On Noise Generated by Turbulence in a Pipe Downstream of a Discontinuous Area Enlargement": B. Stahl and A. Michalke present their measurements of pressure fluctuations at the wall of a circular pipe downstream from a jet inlet. They find that the wall pressure is dominated by turbulence in a section of the pipe close to the jet. Farther away from the inlet, it is influenced by the acoustic properties of the tube. They give information concerning the size of and coherence of turbulent fluctuations at the wall of the tube [Stahl and Michalke, 1985].

1.7 Plan of Thesis

The properties of turbulence noise sources will be investigated experimentally with mechanical models. The vocal tract will be modeled as a straight tube and the glottal air supply by a jet of air entering the tube at a variable angle. The models will be experimentally tested and theoretically analyzed from aerodynamic and acoustic points of view.

For each value of jet angle, sound recordings will be made with and without a small annular obstacle present in the tube. Sound pressure spectra will be calculated from the recordings. The spectral make-up of a point source at the obstacle location may be estimated from comparison of the recorded spectra for models with and without obstacles. Finally, the output spectrum for a particular distribution of sources appropriate for the speech sound /h/ will be calculated from the transmission line model of the tube and the experimentally derived point source spectra. The anatomy of the vocal tract and articulatory configuration for the speech sound /h/ in the context of the vowels /ʌ/ and

/ə/ suggest a distributed source along the wall near the glottis.

The paper consists of four chapters. Chapter 1 has introduced the topic of the study and provides an overview of the principles of fluid dynamics necessary to characterize subsonic turbulent jets. Chapter 2 describes experiments performed on mechanical versions of the vocal tract models. Chapter 3 contains the theoretical aerodynamic and acoustic analyses of the models resulting in estimates of the source spectra for various obstacle locations in the tube. In Chapter 4, the radiated sound spectrum for a possible distribution of point sources, which may exist during the production of /h/ sounds, is calculated. In Chapter 5, final conclusions are then made. Calibration curves and data are compiled in the appendices.

Chapter 2
A jet in a Tube: Acoustic Measurements

2.1 Introduction

In this chapter, the acoustic and aerodynamic effects of a jet in a tube are investigated. A jet in a tube is of interest as a model of aspiration and frication noise production. Several acoustic sources may be produced by a jet in a tube. In the free flow airstream of the jet, turbulent velocity fluctuations give rise to quadrupole sources which are coupled to the sound field like volume velocity sources. Jet flow angled to impinge on the tube walls produces fluctuating shear stresses along the wall which are coupled as series pressure sources. Jet flow impinging on an obstacle produces fluctuating forces which are analogous to wall sources, and form a combination of dipoles and quadrupoles. Fluctuations in mass flow at the jet nozzle and tube mouth may produce monopole sources that are large enough to make a significant contribution to the output. The size of the monopole at the mouth will depend on how well the jet has been damped when it reaches the tube mouth; thus, it depends on the total tube length. The various sources correspond to several fluid dynamic situations, such as impinging jets and wall jets. The mechanical models of these experiments are used to study the sound sources produced by jet interactions in a vocal-tract sized tube. They provide information for understanding speech sound production.

The first series of experiments described here investigates pressure sources produced by velocity fluctuations in a model of the vocal tract with a single jet at one end of the model. The second series compares the sources produced when the jet in the model impinges on obstacles with different orientations. The dipole sources in this case are oriented in different directions, and hence are expected to couple differently to the modes of the tube.

2.2 Materials, Methods and Calibration

The general structure of the experimental system is shown in the block diagram of figure 2.1. The system consists of an air flow generating system, a mechanical model to be tested, a sound pressure recording system, and a data processing system.

The air flow generating system consists of a pressurized tank of dry air, 1/4" x 1/16" Vincon clear PVC tubing, a Manostat flowmeter (cat. no. 36-541-31 with 3/8" steel ball), a T-junction, quick release connectors, and a manometer. The air line system and mechanical model are shown in figure 2.2. Air is fed from the pressurized tank through an AIRCO needle valve regulator and a 7 m length of tubing to the flowmeter. Quick release pressure fittings are used to join air line tubing to other apparatus in the line. The

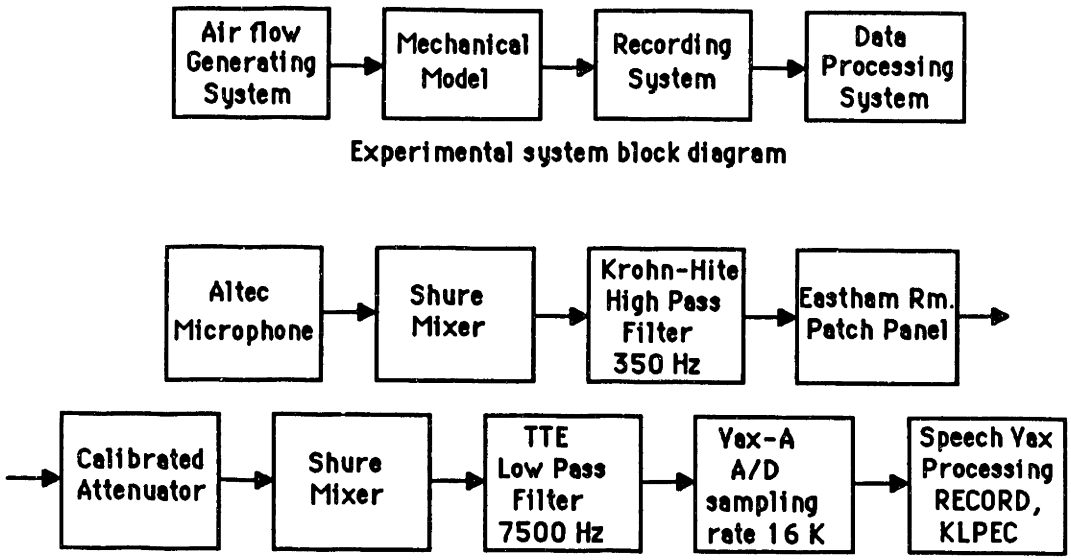

Figure 2.1 System block diagrams.

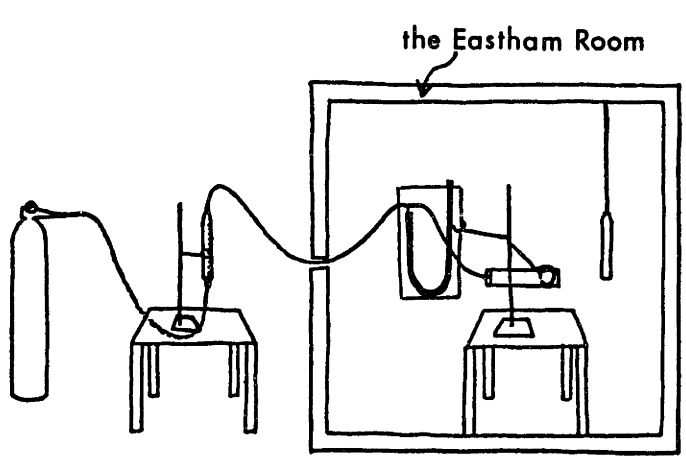

Figure 2.2 Air line system and mechanical model.

flowmeter was calibrated by placing a calibrated Fischer & Porter flowmeter (tube no. FP-318-25-G-5136 with 3/8" steel ball), in series with it and the air tank. The second flowmeter emptied into the room; no load was used in the calibration circuit in keeping with the method Fischer & Porter use to calibrate their flowmeters. The volume velocity flow through the two flowmeters was varied and the value on each flowmeter was recorded. A diagram of the flowmeter circuit and the resulting calibration curve are included in figure A.1 Appendix A. Air flow from the flowmeter was connected to a second 7 m length of Vincon tubing which entered the recording room (the Eastham Room) through the doorway or an open cable panel in a side wall. In the recording room, the tubing was connected to a static pressure manometer via a T-junction. The mechanical model was connected to the third port of the T-junction. A volume velocity of 442 cm^3/sec was used in all experiments.

A mechanical model of the vocal tract configuration for the speech sound /h/ spoken before the vowels, /ʌ/ or /ə/ was constructed. The vocal tract configuration for this sound is uniform to a first approximation. An 18 cm section of 3/4" x 1/8" Vincon clear PVC tubing was used to model the vocal tract walls. It will be called the tube in this discussion. Several interchangeable metal or wooden constrictions were available and could be placed in the glottis end of the tube. The tube was elastic and the metal constrictions fit snugly into the tube. Wooden constrictions were sealed with plasticene at the tube-constriction junction to insure an airtight fit. With a constriction capping the tube, the length of the tube became 17 cm, the typical length of a man's vocal tract. The diameter of the tube was chosen to make the tube volume as close to 60 cm^3 as possible within material limitations and the above length constraint. The cross-sectional area and volume of the model were 2.85 cm^2 and 48.5 cm^3, respectively. The tube was supported at both ends. The mouth of the tube rested in a clamp attached to a ringstand with the mouth of the tube protruding slightly from the clamp. The constriction end of the tube was suspended by the air line connecting the tube to the T-junction. Each constriction had a hole machined or drilled through it of the proper diameter to accept a 2.2 cm long piece of #7 gauge stainless steel needle tubing with inner diameter of 0.15" corresponding to a cross-sectional area of 0.114 cm^2. The constrictions were 1 cm in length. The constriction geometries are shown in figure 2.3. They differ in the angle the needle tubing makes with the tube axis, θ. The set includes a solid plug. The hole entered the tube at the center of the constriction, except for the 90° degree configuration. The 90° configuration was constructed as shown in figure 2.4. The plug at the glottis end was sealed into the tube with silicon bathroom

cement. A piece of needle tubing inserted flush with one side of the opening in a constriction protruded 1.2 cm from the opposite side of the constriction. A 9.3 cm section of airline was placed over the protruding needle tubing and glued in place with silicon cement. The other end of the air line tubing was used to connect the model to the T-junction at the manometer. A moveable annular obstacle was machined from an aluminum plug to the dimensions indicated in figure 2.5. The obstacle could be placed at any location in the tube, except the location of the air inflow in the 90° model.

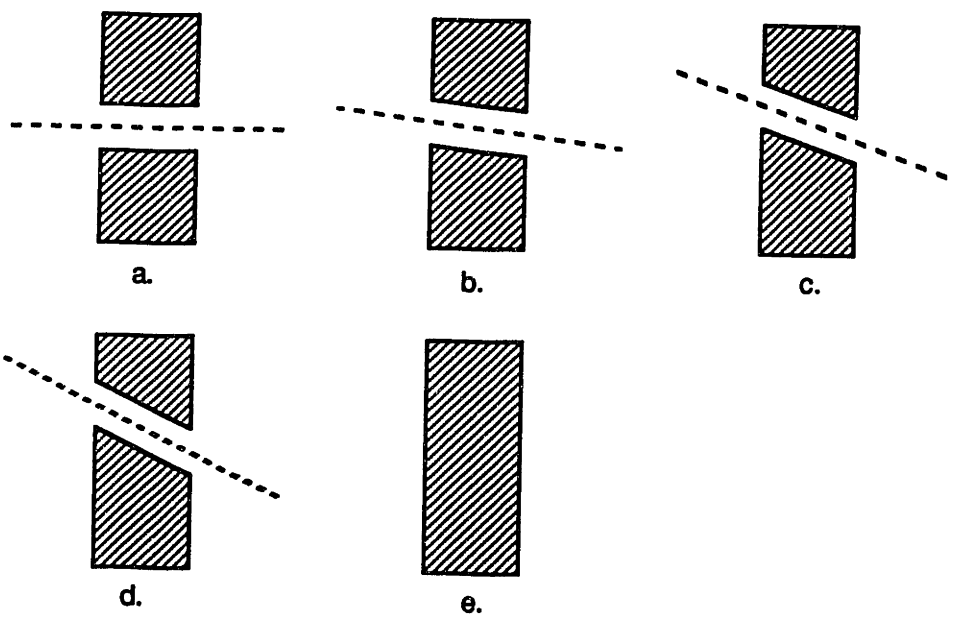

Figure 2.3 Constriction geometries. a) 0° jet, b) 10° jet, c) 19° jet, d) 27° jet, e) plug.

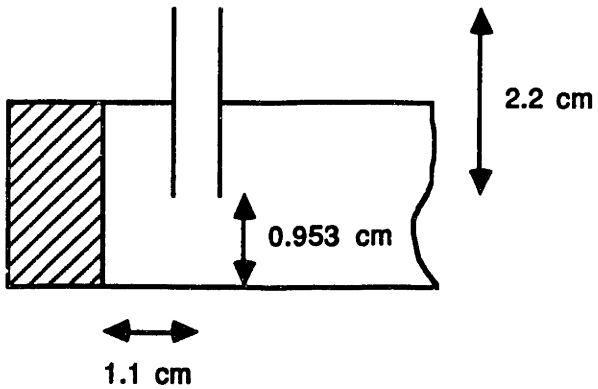

Figure 2.4 90° jet inlet.

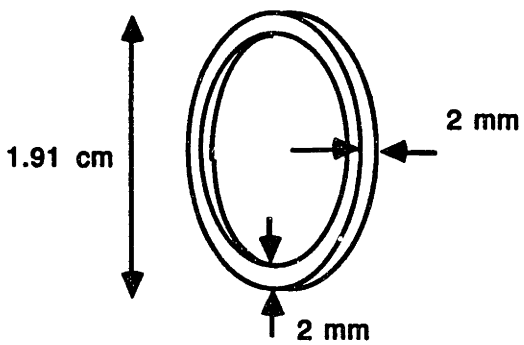

Figure 2.5 Annular obstacle.

Sound produced by the mechanical model was recorded in the Eastham Room facility of the MIT Speech Group. The room has a low frequency noise signature, which influenced the choice of high pass filter cutoff used in the experiment. Some external noise leakage may have occurred at the entry point of the air line. Additional noise leakage from the open cable panel in the recording room was minimized by loosely packing the hole with foam rubber. Room noise recordings made with and without open air line entry points were negligibly different.

A block diagram of the recording system is included in figure 2.1. Sound pressure was recorded with an Altec 684A omnidirectional microphone and a balanced output Shure

mixer Model M67 as pre-amp. The microphone was placed 26 cm from the mouth of the tube at an angle of 28° from the axis of the tube. The directivity pattern is uniform for angles 0° to 30° in the range of frequencies of interest [Beranek,1986]. A Krohn-Hite Model 3202R filter was used in highpass filter mode with 350 Hz cutoff to partially offset the presence of the low frequency room noise. The signal from the Krohn-Hite was passed through the Eastham Room Cannon connector(XLR-3) patch panel to a coaxial cable connected to a calibrated attenuator box and from there to the MIT Speech Vax-A station. The Vax-A station is equipped with circuitry to drive the A/D cable with low impedance, alleviating the problem of high frequency attenuation for input cable lengths up to 100 feet long and properly terminated by 600 ohms [Klatt, 1984]. It also is equipped with a patch panel to facilitate making the proper connections in front of the A/D. For our purposes, recordings were made with the Vax-A line-in connected to a Shure mixer Model M267, a TTE Model J97E 7500 Hz antialiasing lowpass filter and the A/D in that order. The signal was sampled at a rate of 16,000 samples per second. The attenuator box provided flexible gain, since the Shure mixers could not be adjusted to intermediate values of gain with accuracy.

The frequency response of the recording system from microphone to Vax was measured using a series of tones: 250, 500, 1000, 2000, 3000, 4000, and 5000 Hz. The tones were synthesized using KLSYN software and recorded on a cassette tape with a Yamaha K-1000 cassette tape deck at the Vax-A station [Klatt, 1984]. In the Eastham Room, the tones were played back on a Nakamichi LX-5 tape deck through a Crown D-75 amplifier and out of a AR-2ax speaker. Each tone was recorded by the system and then replayed with the Altec microphone replaced by the microphone of a General Radio Type No. 1551-0 sound level meter using C weighting. A cable was inserted between the SPL microphone and meter which added 6 dB of attenuation. Figure A.2 of Appendix A shows the calibration set-up. Several points were taken at each frequency over a range of SPL from 60 to 80 dB. The tone frequencies recorded on the Yamaha and played back on the Nakamichi were not the same. The differences were attributed to inaccurate head speed of one or both of the decks. Figure A.3 of Appendix A contains a curve relating recorded tone frequency on the Yamaha to that played on the Nakamichi.

The frequency response of the system could be broken into frequency dependent and constant parts. Frequency dependence was associated with the microphone and mixer. The rest of the system provided a constant gain independent of frequency. The microphone and pre-amp frequency response was determined using the pre-recorded tones and a digital volt meter to measure the output voltage at the mixer. It has the same shape as the system

curve. The system and microphone/mixer calibration curves are included in figures A.4 and A.5 of Appendix A.

The recordings were processed using KLSPEC software [Klatt, 1984]. Approximately 900 ms of each recorded signal was analyzed by KLSPEC using the averaged periodogram option. Its algorithm uses 512 point overlapping cosine windows and discrete Fourier transforms to calculate the positive half of the averaged spectrum for each recording, in the frequency range of 0 to 8000 Hz. The amplitudes in dB of each spectrum at the first six resonant frequencies were read from the plots provided by KLSPEC and corrected for microphone frequency response and system offset by adding the number of dB indicated on the system calibration curve (figure A.4), to yield sound pressure levels in dB re 20 μPa. The resulting numbers in units of absolute sound presssure in dB re 20 μPa will be called the corrected data and can be found in Appendix B, Tables B.1-B.5.

2.3 Experimental Procedure: Pressure Sources at Obstacle

In this experiment, the jet entry angle was varied and data were recorded for five values of angle, θ: 0°, 10°, 19°, 27°, and 90°. For all except 90°, the flow entered from the center of the plug. In the 90° case, flow entered through a short piece of tubing inserted in the side of the tube such that the flow would impact the wall 1.1 cm from the end of the tubing. The volume velocity of tne flow was 442 cm^3/sec. The static pressure drop from manometer to the mouth of the tube was 7 to 8 cm H_2O for all jet angles, except 90°. The pressure drop for 90° models was 10 to 11 cm H_2O. For a particular jet angle, the small annular obstacle was placed in the tube with its surface closest to the tube inlet at a given axial location, z. The nozzle end of the tube was located at z = 0 cm; the mouth at z = 17 cm. Sound was recorded without the obstacle, and with the obstacle at sixteen axial locations in the tube. Thus, seventeen recordings were made for each jet angle. The recordings were processed as discussed previously and resulted in an averaged spectrum for each particular obstacle location, yielding seventeen spectra for each jet angle.

A jet of air impinging upon an obstacle generates more and stronger sound sources than the same jet passing the region with no obstacle. By inserting a small obstacle perpendicular to the wall of the tube, the sound created by the shear force along the wall is amplified and can be measured. By changing the obstacle location, a relative measure of the fluctuation in shear force with location is obtained. The small obstacle located at the tube wall in these experiments provides information on the relative strength of shear forces generated in certain flow situations and on the various sound pressures that can be produced by the correct orientation and location of an obstacle. This information is important in

understanding the production mechanisms of speech sounds such as /h/ and /x/.

The connections between the air line, manometer and mechanical model created a baseline of noise in the experimental system. In order to determine this noise baseline, sound recordings were made for the 0° jet constriction without the tube. Two configurations of the air line inlet were examined: that used for the experiments above and shown in figure 2.6a, and a set-up with no manometer. In the latter case, the air line was directly attached to the constriction air line tubing as depicted in figure 2.6b.

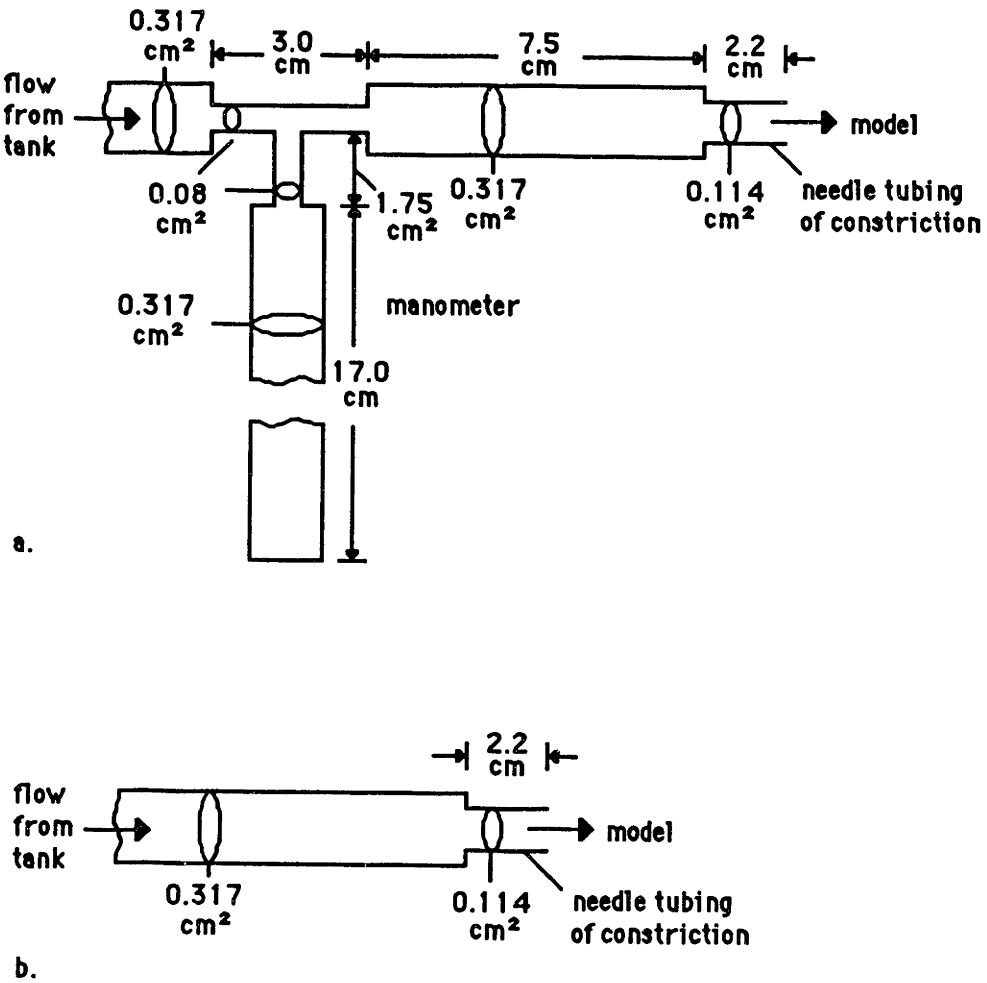

Figure 2.6 Air line inlet structure. a) Experimental inlet, b) No manometer connections.

2.4 Results: Pressure Sources at Obstacle

The sound recordings for the two air line inlet configurations yielded fairly flat average spectra. The spectrum corresponding to the experimental set-up had a spectral density of 25 to 30 dB in 50 Hz bins. The overall SPL was about 47 dB. The spectrum from the second configuration was identical to that of the first in the 350 to 750 Hz range (approximately 27 dB in 50 Hz bins) and 6 dB less for 1000 to 7500 Hz. The information provided by the spectra indicates that the SPL (dB in 50 Hz bins) produced by the sound sources of the free jet is at least 6 dB less than that due to the noise sources in the experimental inlet and manometer connections. The sound pressure due to the free jet sources could be significantly less than 6 dB, if the no manometer inlet connections produce noise sources in addition to those of the free jet. The noise sources produced during flow interactions with the manometer connections can be represented by a monopole source located at the jet nozzle.

When the free jet is placed in a tube as in the 0° jet no-obstacle model, the monopole source will be located at the tube inlet and the free jet quadrupoles will be spread along the tube. If the tube is assumed to be wide enough, no significant jet-wall interactions will occur, and thus no other sound sources will be present in the tube. The monopole is stronger than the quadrupole sources. The monopole will couple to the uniform plane wave modes of the tube more efficiently than the quadrupole sources, especially to the low-frequency modes. Therefore, the radiated sound pressure a distance from the mouth of the tube will be primarily due to the monopole at the inlet. The radiated sound pressure due to the connection noise monopole can be used as a threshold to compare with the radiated sound pressure from other models.

The corrected data are plotted in figures 2.7 to 2.11 for each jet angle. Room noise did not significantly contribute to the spectral densities of the sound recorded from the models during the experiments. Each corrected data point represents the amplitude of the spectral density at a particular resonant frequency. The value of a point depends on the contributions from two sets of sources: the sources in the model with no-obstacle present, such as the connection noise monopole and sources produced by an impinging jet at the tube walls, and the dipole sources produced by the flow interactions with an obstacle. From these data, it is possible to characterize the length and position of the distributed source created by the jet of air in a given model and to approximate the location of the greatest amplitude point sources in it.

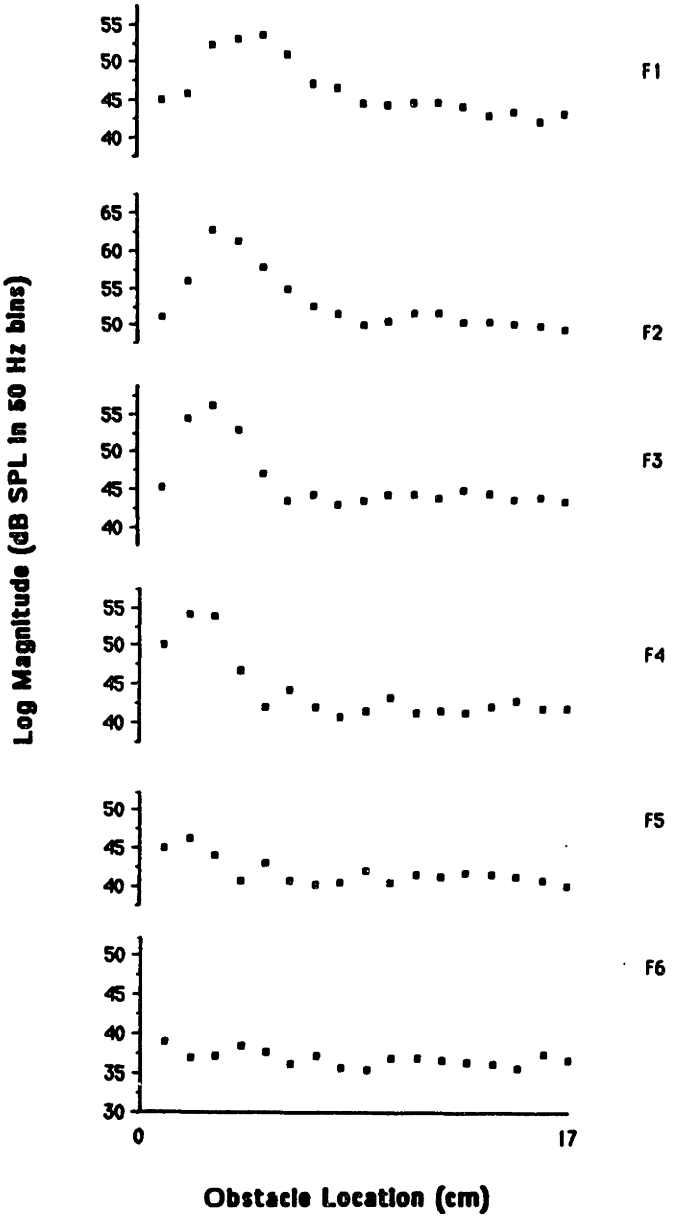

Figure 2.7 Data for the 0° jet models recorded at a distance of 26 cm from the mouth of the tube. The no-obstacle data points are plotted at 17 cm.

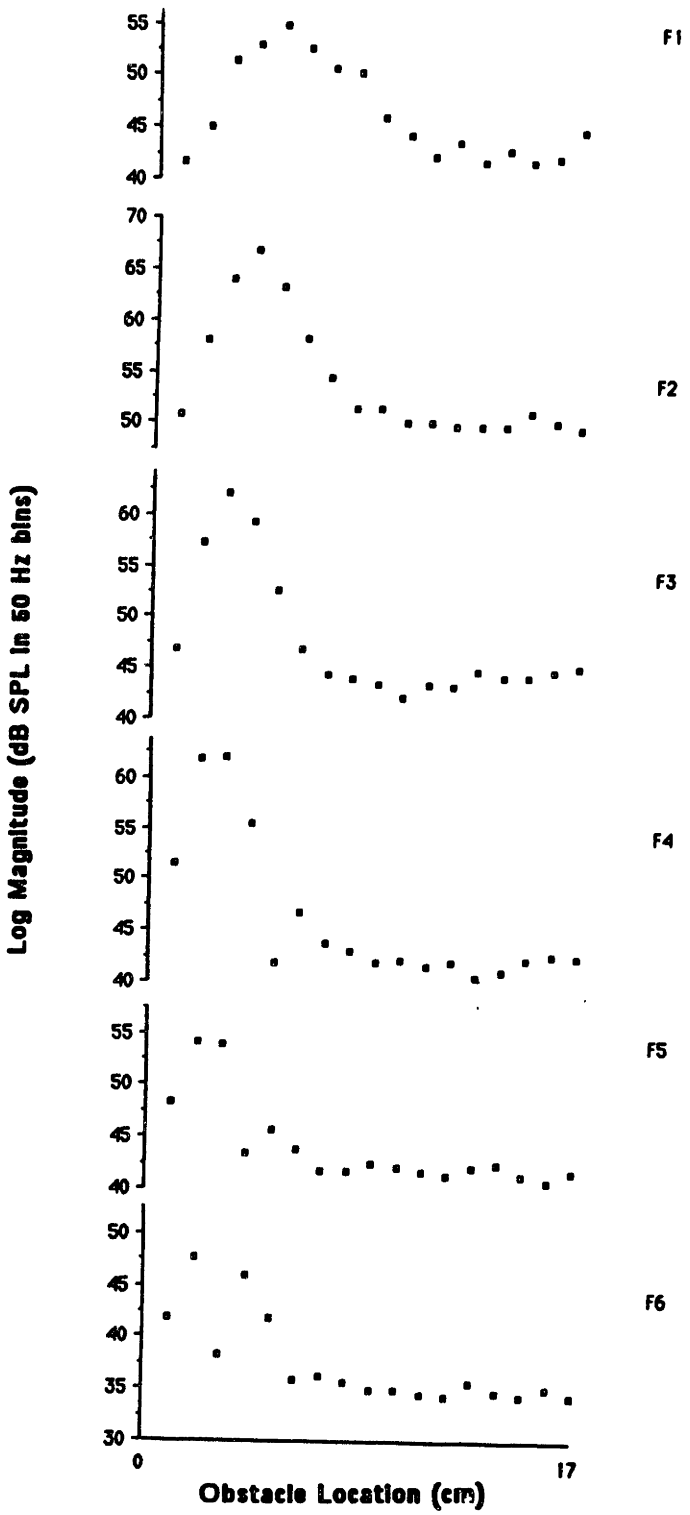

Figure 2.8 Data for the 10° jet models recorded at a distance of 26 cm from the mouth of the tube. The no-obstacle data points are plotted at 17 cm.

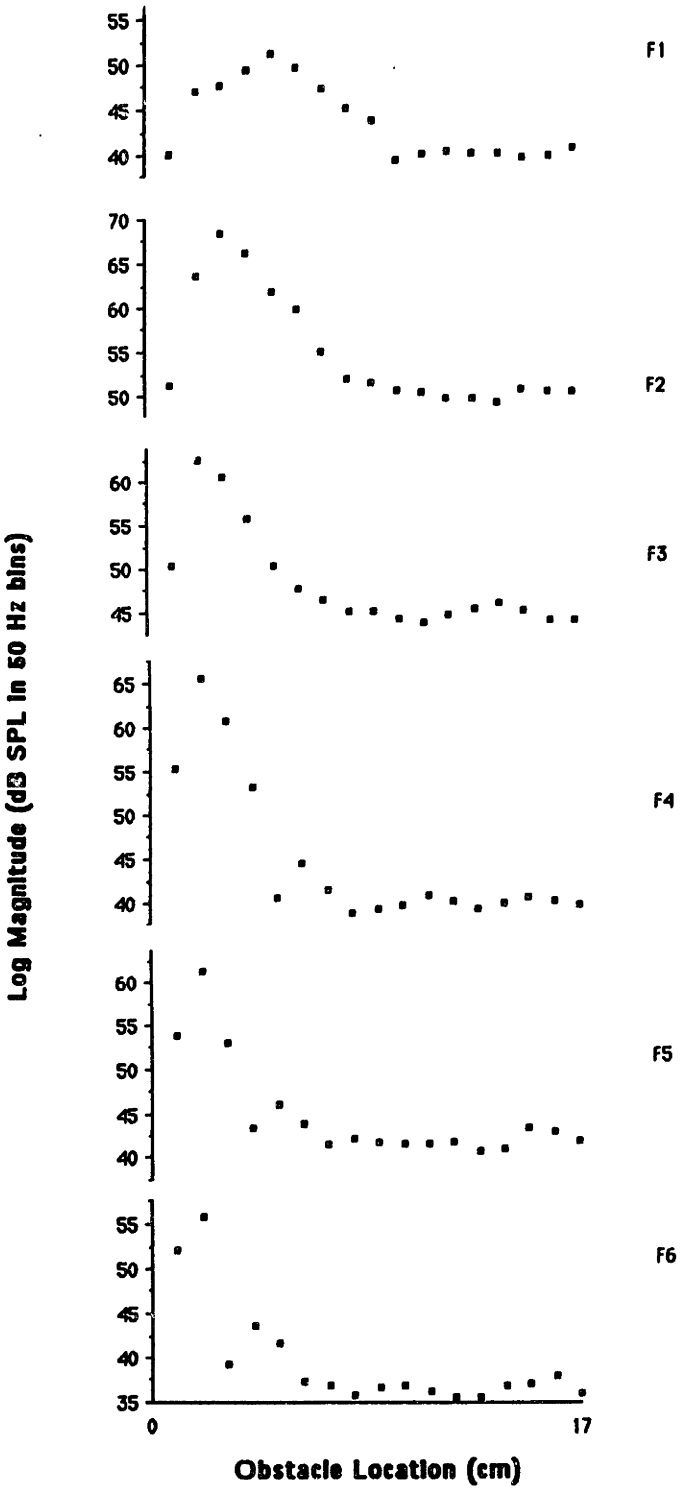

Figure 2.9 Data for the 19° jet models recorded at a distance of 26 cm from the mouth of the tube. The no-obstacle data points are plotted at 17 cm.

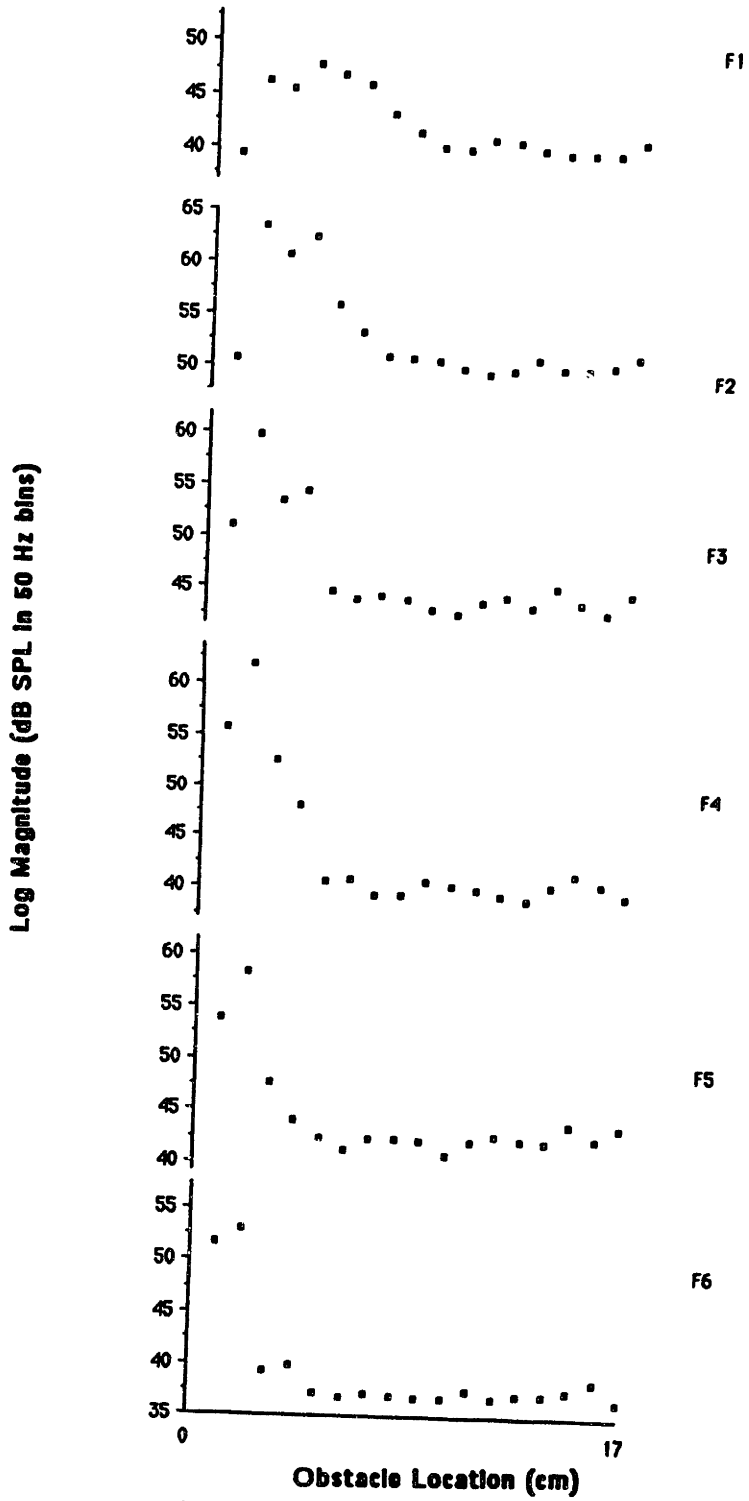

Figure 2.10 Data for the 27° jet models recorded at a distance of 26 cm from the mouth of the tube. The no-obstacle data points are plotted at 17 cm.

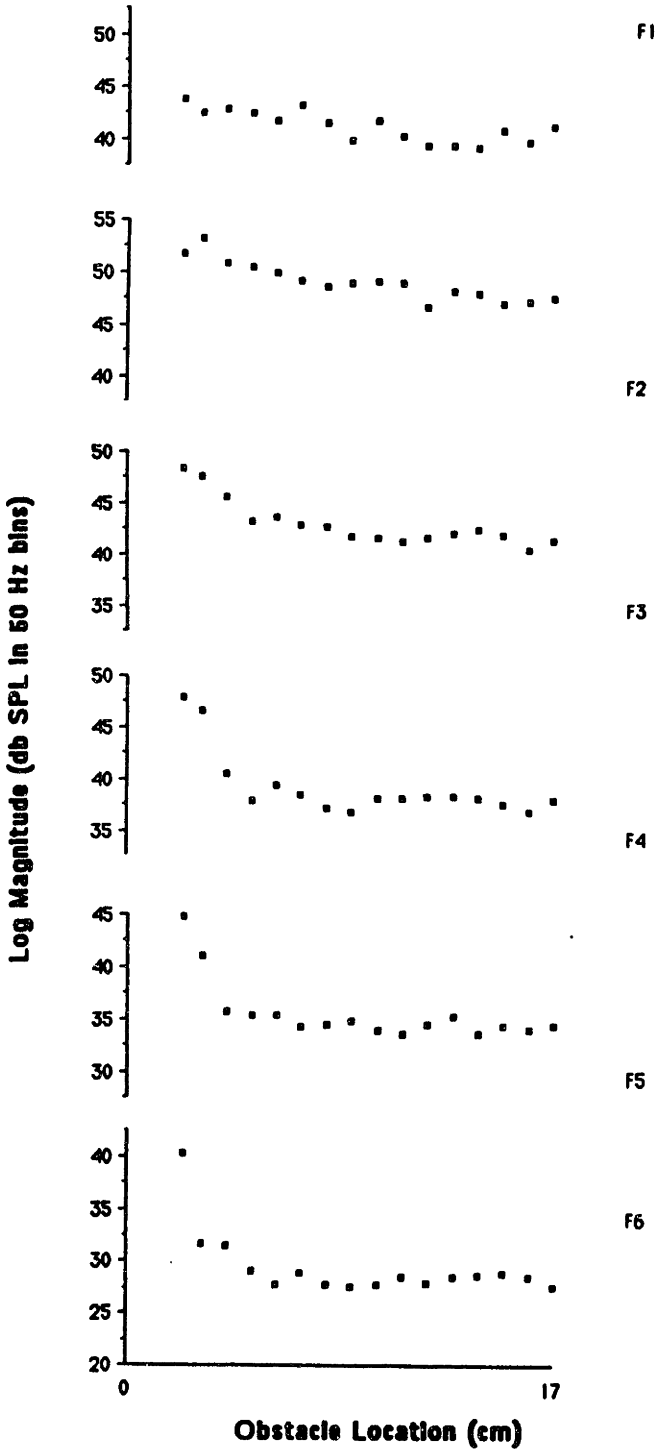

Figure 2.11 Data for the 90° jet models recorded at a distance of 26 cm from the mouth of the tube. The no-obstacle data points are plotted at 17 cm.

By placing the obstacle at a particular location in the tube, the radiated sound pressure produced by turbulent velocity fluctuations at that location is amplified. The obstacle locations that result in increased radiated sound pressure are the locations of the point sources responsible for radiated sound pressure production within the distributed source. From the data and knowledge of the approximate axial location of standing wave nulls in the tube, it is possible to determine roughly the axial extent of the distributed sound source for each jet angle and resonant frequency. The results are shown in figure 2.13.

For a given model and resonant frequency, the range of obstacle positions for which the amplitude of the spectrum at that frequency exceeded the amplitude of the spectrum for the no-obstacle model by 2.5 dB was determined. While making this determination, the approximate locations of zero volume velocity at that frequency were considered. Figure 2.12 illustrates the process for the 0° jet models and F4. When an obstacle is located near a point of zero volume velocity for a certain frequency, the pressure sources created there do not couple well to the sound field at that frequency. The radiated sound pressure due to pressure sources located near zeros of volume velocity for a given resonant frequency represents a position of low volume velocity, and not necessarily pressure sources of low intensity. The characteristics of the point sources that make up the distributed source are assumed to vary smoothly with the location of the point source in the distributed source. Thus, the distributed source is larger at the obstacle location than indicated by the resulting radiated sound pressure, and the relative level of the distributed source at that location can be estimated by the levels of its neighbors. For instance in figure 2.12, the obstacle location of 5 cm corresponds to a zero in volume velocity at F4. The spectral amplitudes of the points on either side are at least 2.5 dB greater than that of the no-obstacle case. Even though the amplitude at F4 for 5 cm is lower than the threshold, pressure sources located there are included in the distributed source.

The approximate locations of zero volume velocity may be determined. In these experiments, the tube end conditions are almost ideal. The impedance looking back at the flow inlet is much greater than the characteristic impedance of the tube, and the radiation impedance is small compared to the characteristic impedance for frequencies below about 5000 Hz. Thus, the positions of zero volume velocity can be predicted from the standing wave patterns of an ideal tube with one end closed and the other open. Figure 1.9 illustrates the standing wave envelopes for several modes in such a tube.

Two trends can be seen in figure 2.13 and to some extent in the corrected data. As the resonant frequency increases, the overall source length decreases. The position of peak sound pressure level moves toward the inlet of the tube for increasing resonant frequency.

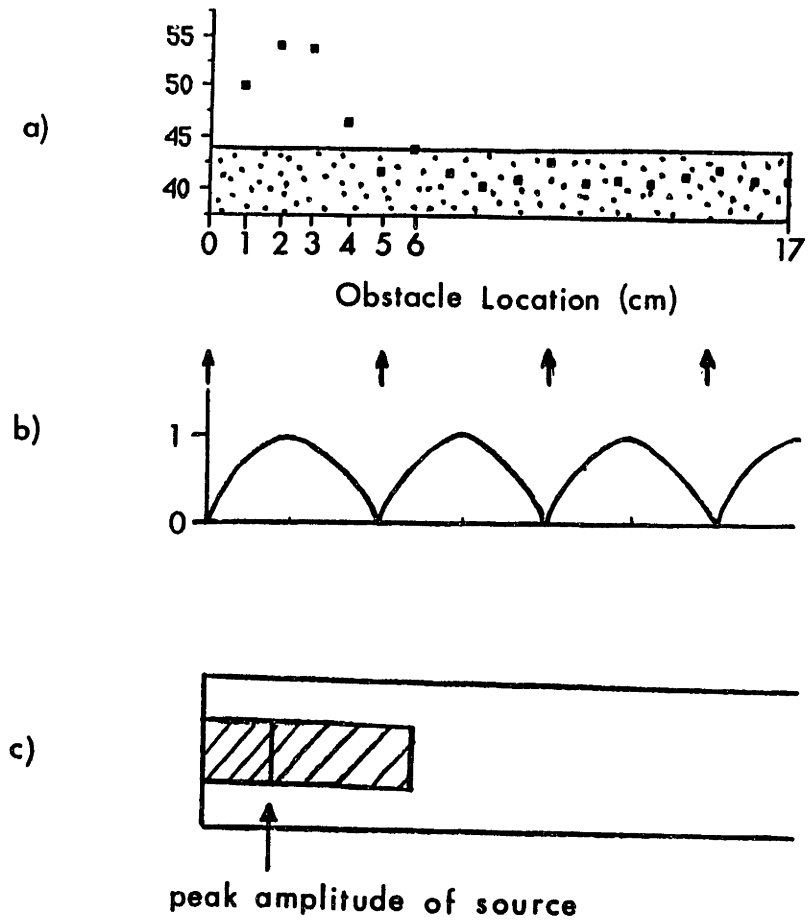

Figure 2.12 Determination of the distributed source region of F4 in 0° jet models from the corrected data. a) The corrected data (taken from figure 2.7). The data points with values within 2.5 dB of that for the no-obstacle model fall in the shaded region. The no-obstacle point is plotted at 17 cm. b) The envelope of the volume velocity standing wave of an ideal tube open on the right end and closed on the left. Arrows indicate approximate locations of volume velocity nulls in the data. c) The location of the distributed pressure source in the tube. The data point at 5 cm indicates low volume velocity, not low pressure source intensity. The source length is estimated to be 6 cm rather than 4 cm.

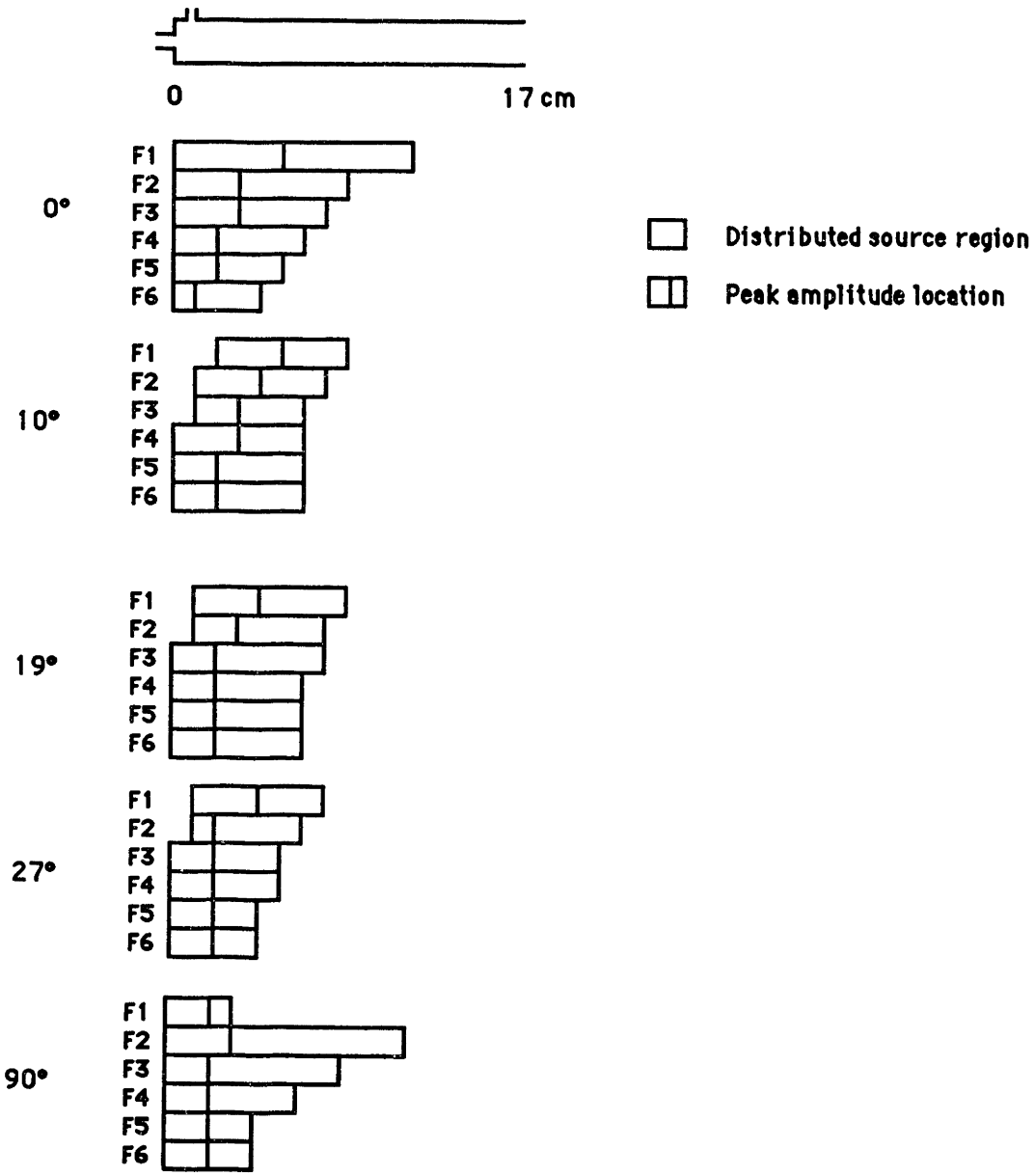

Figure 2.13 Distributed source regions and maxima. The source regions pictured are scaled consistently with the generalized model at the top of the figure. They were mapped by moving a small obstacle down the tube and recording the resultant sound pressure. The sound produced by a model with an obstacle located in the source region will have greater amplitude than that produced by the no-obstacle model. Data from obstacle locations with values within 2.5 dB of the corresponding no-obstacle model data point value were not considered for inclusion in the distributed source unless the obstacle location corresponded to a null in the volume velocity envelope. Source region lengths and peak amplitude locations are only approximate, since the obstacle was moved in centimeter increments.

2.5 Experimental Procedure: Dipole Orientation

In this experiment, the two configurations shown in figure 2.14 are studied and compared to the 0° jet no-obstacle results of the last experiment. The 90° configuration is that of the 90° jet no-obstacle model. The 0° configuration is that of the 0° jet impacting a long metal obstacle placed 1.1 cm from the jet nozzle. The obstacle width is 0.5 cm, which is roughly the same width as the 0° jet would obtain at z = 1.1 cm with no obstacle present. Sound pressure was recorded for the 0° and 90° configurations using the same procedure, equipment, and processing as discussed in section 2.2.

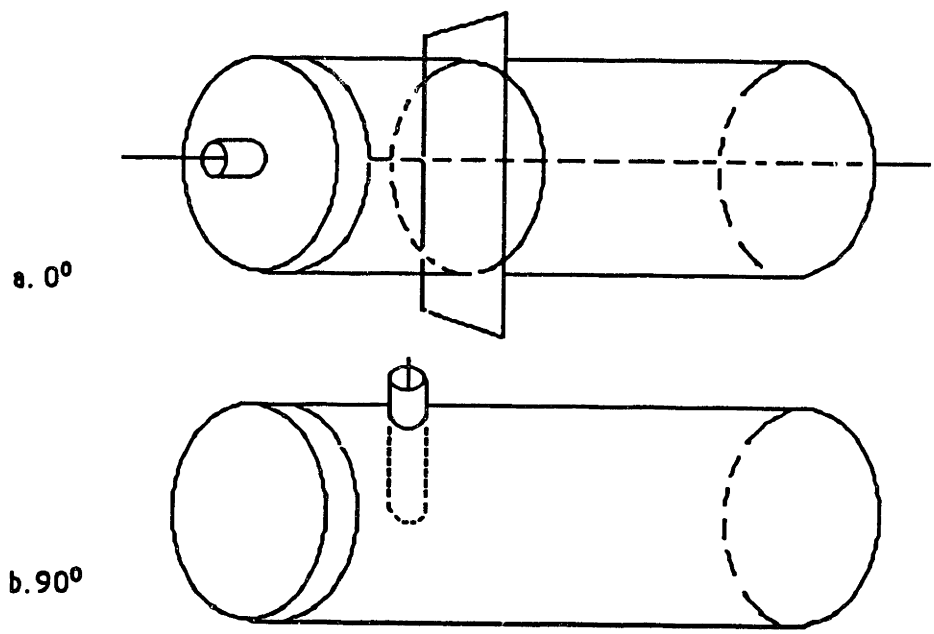

Figure 2.14 0° and 90° tube configurations.

2.6 Results: Dipole Orientation

The recorded spectra have resonant frequencies that correspond to those of the 0° jet no-obstacle spectrum of the previous experiment. In figure 2.15, the radiated sound pressure at the first six resonant frequencies is plotted for both configurations. Second order polynomial fits were made to both sets of data. The upper curve has a correlation coefficient R, of 0.99, and the lower curve has R = 0.98. Differences between 0° jet no-obstacle case and the spectra of this experiment were measured at 500 Hz frequency

intervals and at the peak and trough frequencies in the 350 to 7000 Hz range. These differences are plotted in figure 2.16. There is some scatter in the data, especially for points near troughs. The amplitude of the 90° configuration spectrum was comparable to the amplitude of the room noise spectrum at some of the trough frequencies. The trends are indicated by second order regression curves. The upper curve has a correlation coefficient R equal to 0.95, and the lower curve has R equal to 0.69. All curves were fit using the following equation

$$Y_i = a_1 X_i + a_2 X_i^2 + \text{error} \quad \text{[Rafferty and Norling, 1986].}$$

Scatter in the data plotted in figure 2.16 comes from two primary sources. Each point represents a difference between two sets of averaged data. Although the data have been averaged to surpress some of the noise in the measurement, the spectra still contain noise. At points near troughs, the signal-to-noise ratio (SNR) is smaller and more uncertainty in those measurements is to be expected. Finding the trough is especially difficult, since the minimum is a region of low sound power. The second source of error is in reading the data from the graphic output. Correctly determining the location of a point in a spectral region of high slope is difficult.

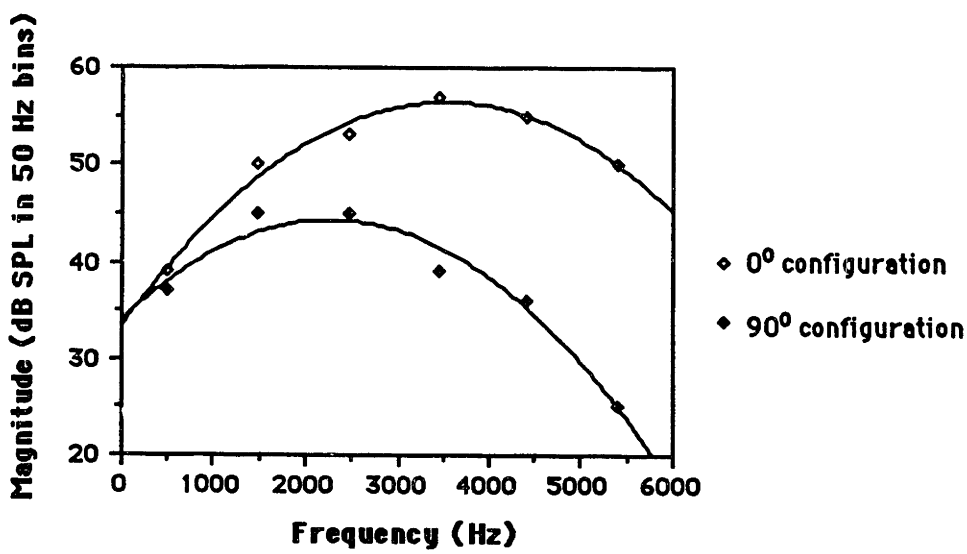

Figure 2.15 Radiated sound pressure for 0° and 90° configurations sampled at the first six resonant frequencies.

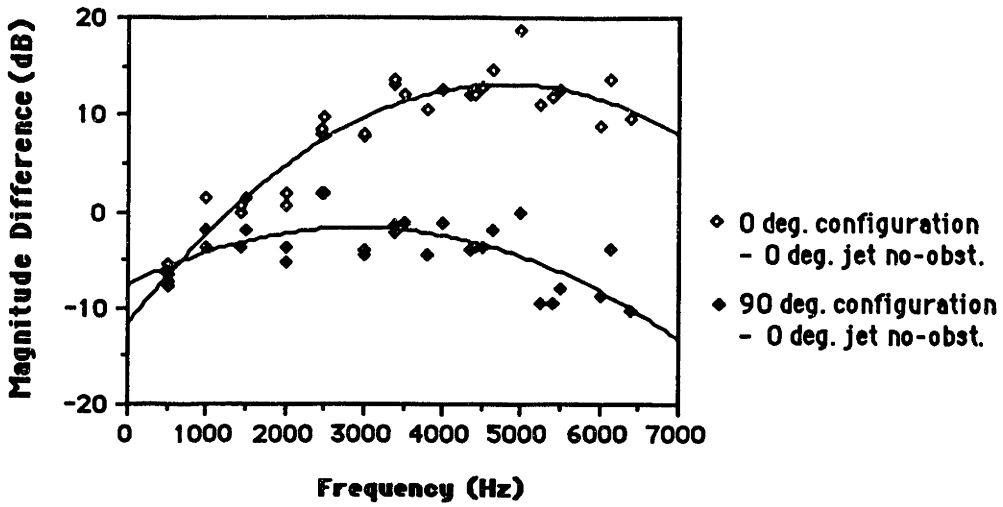

Figure 2.16 Differences in SPL for configurations with respect to the 0° jet no-obstacle model.

2.7 Discussion

The results of the first experiment in figures 2.7 to 2.11 and in a more general format 2.13 support observations in the literature that higher frequency components of turbulence decay more quickly than low frequency components [Thwaites and Fletcher, 1979, 1980, 1982, 1983]. The data support these observations in two ways. The source region length decreases as the source frequency increases. The position of peak amplitude occurs nearer the inlet as frequency increases. As the turbulence frequency varies from low to high, the turbulence decays more quickly and therefore closer to the inlet.

The length of the source region and position of the maximum in radiated sound pressure depend on jet angle as well as on frequency. In general, figure 2.13 shows that the region length decreases and the source peak moves towards the inlet as the jet angle increases. Figure 2.17 shows the peak amplitudes in radiated sound pressure for each resonant frequency and jet angle. From these curves, it can be seen that jet angles between 10° and 20° produce the maximum radiated sound pressures for each resonant frequency and radiated sound pressure is larger for the mid-frequency range (F_2, F_3, F_4) than higher or lower frequencies. The curves in figure 2.17 will be compared to the maximum amplitudes

of calculated source sound pressures shown in figure 3.13 in Ch. 3.

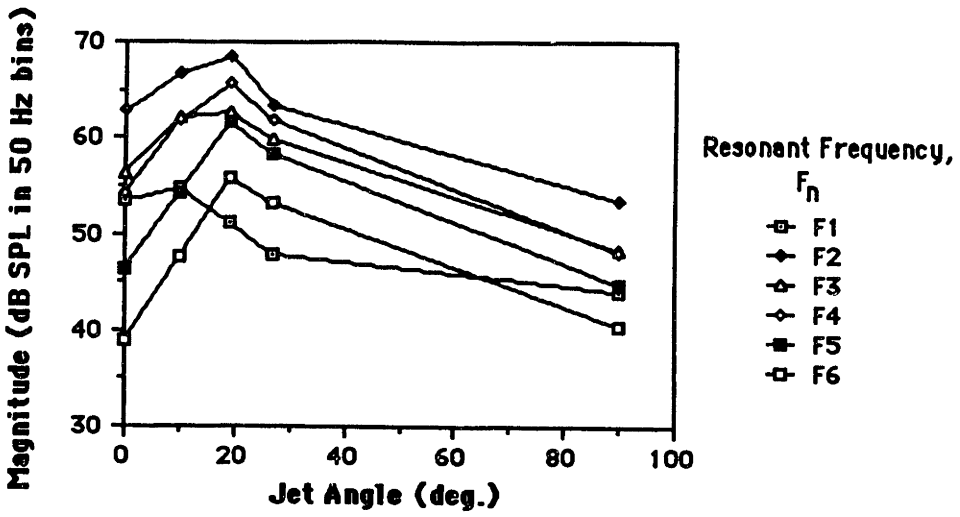

Figure 2.17 Radiated sound pressure peak magnitude versus jet angle.

In the second experiment, the importance of the geometric orientation of sound sources produced by an impinging jet is considered. Their orientation is important because it determines in part how well a source's energy will be coupled to the sound field. In an impinging jet, sound is produced by fluctuating normal and shear forces. The strength of the sound source depends on how it is produced.

Shear forces generally produce weaker sound than normal forces. Shear and normal forces produce sound by creating pressure and velocity variations in the air around them. Normal forces also cause changes from the ambient pressure or volume velocity as the flow stagnates near the surface. For instance, a pressure microphone at rest in a flowing medium with diaphragm perpendicular to flow will record a different pressure due to turbulent fluctuations than one with diaphragm oriented parallel to the flow. If the microphone does not disturb the flow, the ratio of turbulent pressure recorded is

$$\frac{\text{perpendicular}}{\text{parallel}} = \frac{2\,V_0}{v}$$

where $V_o \gg v$, V_o is the mean flow velocity and v is the rms fluctuation in velocity [Morse and Ingard, 1968]. A typical value of v is one-tenth of the mean flow velocity. If the rms value of the turbulent velocity fluctuations measured by the microphone is estimated to be one-tenth the mean flow velocity, this ratio gives a difference between perpendicular and parallel forces of 26 dB [Morse and Ingard, 1968]. In the experiment, normal and shear forces at a point on the impact surface are related to each other in the same way as the perpendicular and parallel forces on the microphone.

In the 0° and 90° configuration, air flow hits a surface roughly perpendicular to it and transitions into a wall jet. Figure 1.2 depicts an impinging jet. The two configurations have some minor differences and one major difference. The minor differences are due to differences in the obstacles. For instance, the 0° impingement zone is smaller than the 90° one. If the velocity fluctuations have significant normal components at the edges of the 0° impingement zone, the sound recorded from the 0° configuration will be less than that from the 90° configuration by a small amount. Similarly, the region for wall jet formation is smaller for the 0° configuration than for the 90° one. The wall jet produces dipoles oriented in the direction of shear forces. In the 0° case, the shear force produced by a wall jet would be perpendicular to the tube axis and would not be able to couple to the sound field in the tube. Likewise, the portion of the 90° wall jet perpendicular to the tube axis would not couple to the sound field. The difference between the curved wall and the flat 0° obstacle will have a second order effect on the sound pressure at each obstacle and is probably not important in this experiment. An important difference is due to the placement of the inlet noise monopole and free quadrupole sources in the tube. The monopole and quadrupole sources of each configuration couple differently because they are at different locations in the two configurations, as shown in figure 2.18. The sources couple to the tube like volume velocity sources. For frequencies below 6000 Hz, the farther the source is located from the tube inlet, the less well it will couple to the sound field (within 0 to 1.5 cm of the inlet). If the source is moved from the tube inlet to a position z cm from it, the coupling coefficient changes from unity to $\cos((2n-1)z\pi/2l)$, where n is the mode number. For z = 1.1 cm, the coupling coefficients are: 0.99, 0.95, 0.87, 0.76, 0.61, 0.44 for the first six modes and correspond to loss in dB: 0.1, 0.5, 1.2, 2.4, 4.3, 7.1, respectively.

The two curves in figure 2.16 are referenced to the radiated sound pressure produced by the 0° jet no-obstacle model. The sources produced by each configuration differ in location and orientation. The 0° and 90° configurations have less free quadrupoles than the 0° jet no-obstacle model because their free jet regions are much shorter. The radiated sound pressure produced by free jet quadrupoles is small compared to that produced by the

inlet monopole, as discussed eariler in this section. Thus, the SPL at a distance from the mouth of the tube will not be greatly affected by the absence of some free jet quadrupoles. The 0° configuration and 0° jet no-obstacle model also differ in that the 0° configuration contains an obstacle. The dipole sources in the 0° configuration impingement zone are important sound sources, and these are not produced in the 0° jet no-obstacle model. The spectrum of the 0° configuration is greater than that of the 0° jet no-obstacle model by at least 5 dB for frequencies greater than 2000 Hz. The high-frequency regions of the curves in figure 2.16 show a drop in amplitude with frequency. For the 0° configuration, the difference amplitude at high frequencies may fall due to increased dipole coupling losses at those frequencies.

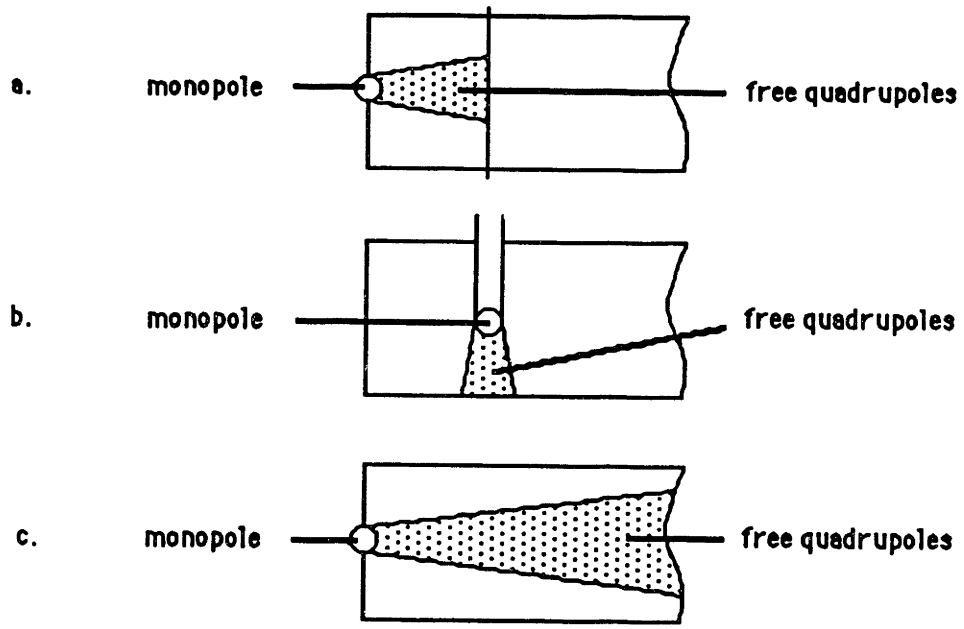

Figure 2.18 Positions of inlet monopole and free jet quadrupoles for a) 0° configuration, b) 90° configuration, and c) 0° jet no-obstacle model.

The 90° configuration produces less radiated sound pressure than the 0° jet no-obstacle model. The monopole and free quadrupole sources of the 90° configuration have lower coupling coefficients than their counterparts in the 0° jet no-obstacle model. The majority of dipole sources produced in the 90° configuration are perpendicular to the tube axis, and thus couple poorly to the sound field. If the sound pressure radiated by the 90°

configuration was primarily due to the monopole at its inlet, and the dipole sources contributed relatively no significant sound, the difference between the sound pressure radiated by the 90° configuration and that by the 0° jet no-obstacle model at high frequencies could be attributed to coupling loss due to the inlet location in the tube. If the difference curve for the 90° configuration in figure 2.16 is assumed to result from the different monopole locations of the 90° configuration and 0° jet no-obstacle model, it can be adjusted to compensate for the different locations. The adjustment is made by adding back the coupling loss due to placing the inlet at a location other than the closed end of the tube. The resulting curve is shown in figure 2.19. At frequencies above about 4000 Hz, the difference curve is approximately zero, which supports the idea that the inlet monopole is the most important sound source in the 90° configuration and that the dipoles produce a negligible amount of sound compared to it. The difference curve is not zero for frequencies below about 2000 Hz, since the 90° configuration and 0° jet no-obstacle model have different input impedances. As mentioned in section 2.3, the static pressure drop is 2 to 4 cm H_2O higher for the 90° configuration than for the 0° jet no-obstacle model, indicating a larger resistance to flow at the 90° configuration inlet. The position of the 90° configuration inlet divides the tube into two cavities, which adds a compliance element to the low-frequency lumped model of tne air inlet. The inlet monopole in the 90° configuration sees a larger input impedance at low frequencies than the 0° jet no-obstacle model monopole, and thus produces less radiated sound pressure at those frequencies.

The difference in radiated sound pressure produced by the 0° and 90° configurations is the difference in dB SPL between the curves in figure 2.15 or 2.16. The gap between them results from differences in source location and size. The relative contribution to SPL made by the shear dipole sources in the 90° configuration is difficult to assess, since the radiated sound pressure recorded from the 90° configuration is essentially due to the monopole at the inlet. The relative contribution to SPL made by the normal dipoles in the 0° configuration can be compared to the SPL due to the inlet monopole and free quadrupoles. The 0° and 90° configurations have similar input impedances. The contribution due to the normal dipoles is equal to the difference between the 0° curve of figure 2.16 and the 90° configuration curve of figure 2.19, which has been corrected for monopole location. The resulting curve is shown in figure 2.20. No data were taken a frequencies below 500 Hz. The curve in the region below 500 Hz is a continuation of the smooth curve drawn through the higher frequency data points. The normal dipole sources produced in the 0° and 90° configurations are both represented by the curve in figure 2.20; however, the normal dipoles in the 90° configuration do not contribute to the radiated sound pressure, since they

are oriented perpendicular to the direction of plane wave propagation in the tube. The curve shows how much the normal dipoles will raise the spectral density of the radiated sound pressure with reference to the level of the spectrum of the inlet monopole.

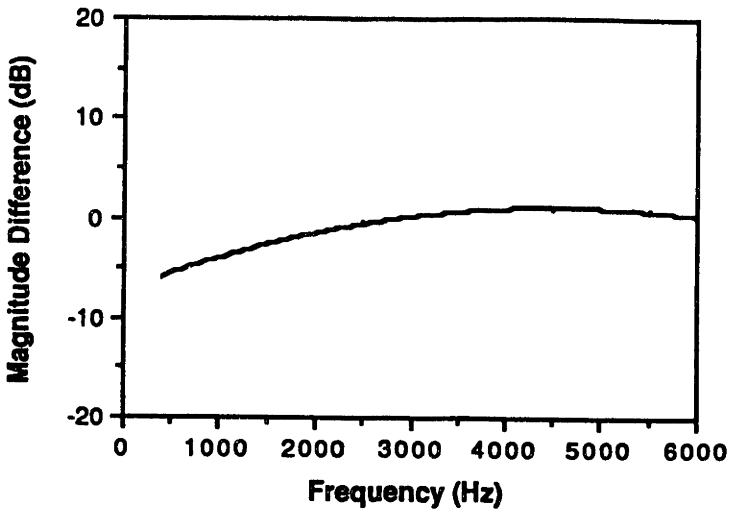

Figure 2.19 Difference in SPL of the spectrum of the 90° configuration corrected for the coupling loss due to the location of the monopole in the tube with respect to the spectrum of the 0° jet no-obstacle model.

The overall SPL of the radiated sound pressure from the 0° configuration is about 75 dB. The increase in the overall SPL due to the normal dipoles oriented parallel to the tube axis is about 28 dB.

In summary, the experiment emphasizes the influence of dipole position and orientation in the tube on SPL some distance from the tube mouth and thus its influence on speech sound produced in the vocal tract.

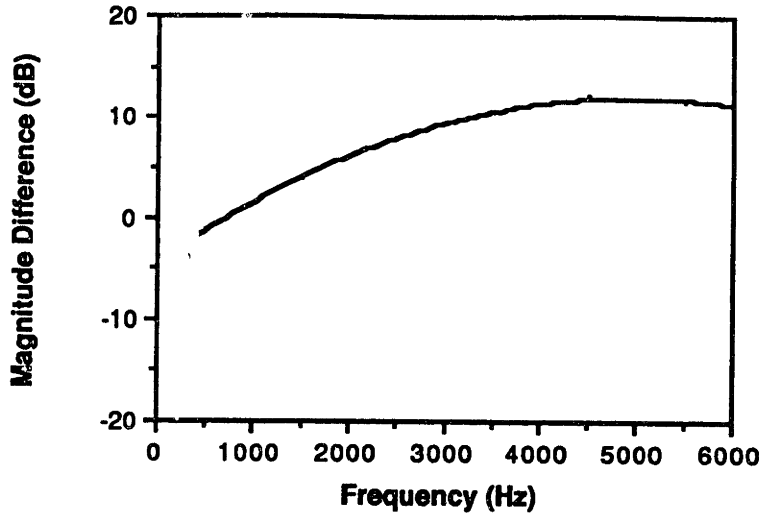

Figure 2.20 Difference in SPL of the spectrum of the 0° configuration with respect to that of the 90° configuration corrected for coupling loss due to the monopole location in the tube. The magnitude difference represents the additional spectral density due to the normal dipole sources produced in the 0° configuration.

Chapter 3
Theoretical Analysis of the Vocal Tract Models

3.1 Aerodynamic Analysis of the Mechanical Models

Flow in a tube with a jet at one end and an opening at the other can be classified by considering the input and output Reynolds number. For these experiments, Re_{nozzle} = 9500 and Re_{mouth} = 1900. These numbers indicate that a transition between turbulent and laminar flow occurs in the tube. The jet does not produce fully turbulent flow in the models. Turbulent disturbances in the flow must reach a threshold value to sustain themselves. In these models, the disturbances are damped on the way to the mouth of the tube. Laminar flow results if the tube is long enough to fully damp out all turbulence.

For the 0° jet no-obstacle model, the empirical formulas for dimensionless axial velocity and jet width may be used to find values of axial velocity and jet width versus axial distance from the jet nozzle. The results are graphed in figure 3.1. These calculations were made for a free jet with a core length of four diameters. If the core length were longer, the profiles in figure 3.1 would be translated to the right. Free jet formulas are appropriate as long as the jet width is small compared to the tube diameter. Otherwise, the numbers are only approximate. The lower graph in figure 3.1 indicates that the jet width will be on the order of the tube diameter 10 cm from the inlet of the tube. The corresponding axial velocity is 800 cm/s compared to 3900 cm/s at the nozzle. It can be concluded that the 0° jet does not interact appreciably with the tube walls.

The sound produced by the 0° jet no-obstacle model can be considered to be the sound from a free jet modulated by the tube. The sound sources for the 0° free jet can be modeled as a monopole located at the inlet due to turbulent noise produced in the air line, manometer, and model connections, together with free quadrupoles in the jet. Monopole sources are generally more acoustically efficient than quadrupoles for the velocities found in fricative production. Experimentally, the radiated sound pressure 26 cm from the jet nozzle produced by the monopole is 6 dB larger than that produced without the manometer connections for frequencies greater than 1000 Hz. The sound pressure recorded for the 0° jet no-obstacle model is larger than that recorded without the tube. The difference is attributed to different radiation characteristics. The 0° jet no-obstacle configuration can be represented by a volume velocity monopole located at the tube inlet and free quadrupoles distributed inside the tube.

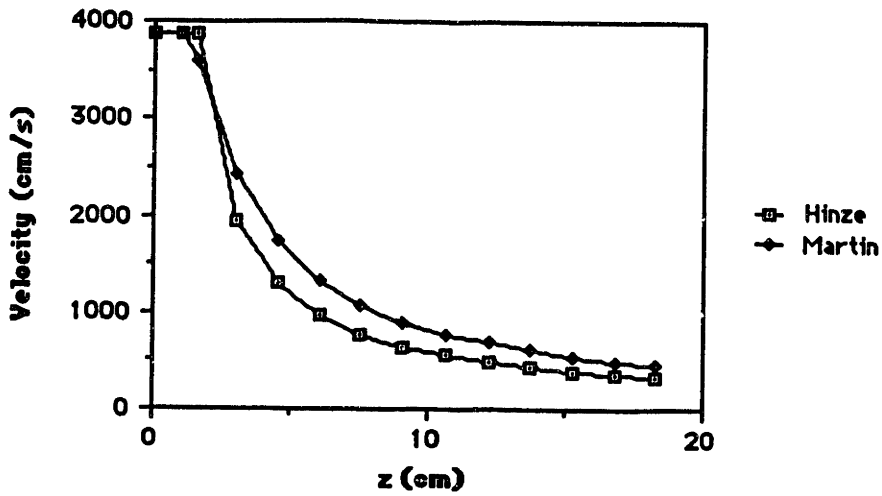

a) Axial velocity versus axial distance from the nozzle for a free jet.

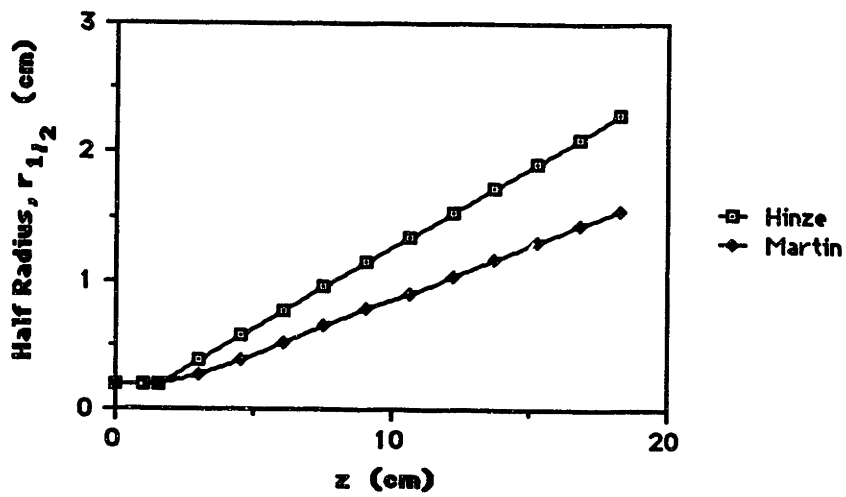

b) Half radius versus axial distance from the nozzle for a free jet.

Figure 3.1 Free jet axial velocity and half radius for a round nozzle of d = 0.381 cm and volume velocity, U = 442 cm^3/sec.

The following relationship between h, the perpendicular distance between the surface and nozzle, and the effective height, h_e, can be found for the angled jet models: $h_e = h/\sin\theta$. Figure 3.2 graphically depicts the jet height h, the effective height h_e, and the velocities of the free jet entering the impingement zone $u(z_w)$ and entering the wall jet $v(r_w)$. Effective heights and impingement zone velocities for perpendicular impact geometry have been calculated using the empirical equations cited in section 1.2 of this

paper. The results are presented in Table 3.1 for $z' = r = 0.6d$ and $r = 1.2d$, $u_o = 3880$ cm/s and $d = 0.381$ cm. No velocity results are given for $\theta = 10^o$, since $h_e/d > 10$ and does not meet the conditions under which the empirical equations are valid. Values of velocity parallel to the impact surface are given for two locations: one is within the region of flow where neither axial or radial velocity components are near zero in size (0.6d), and the other is near the boundary between the impingement zone and wall jet (1.2d). The velocity values greater than the initial free jet velocity of 3880 cm/sec may be due to narrowing of the flow as it moves through the impingement zone. The numbers in Table 3.1 indicate the effect of changing the distance the jet has to travel before impact. Stagnation flow velocities increase as jet height decreases.

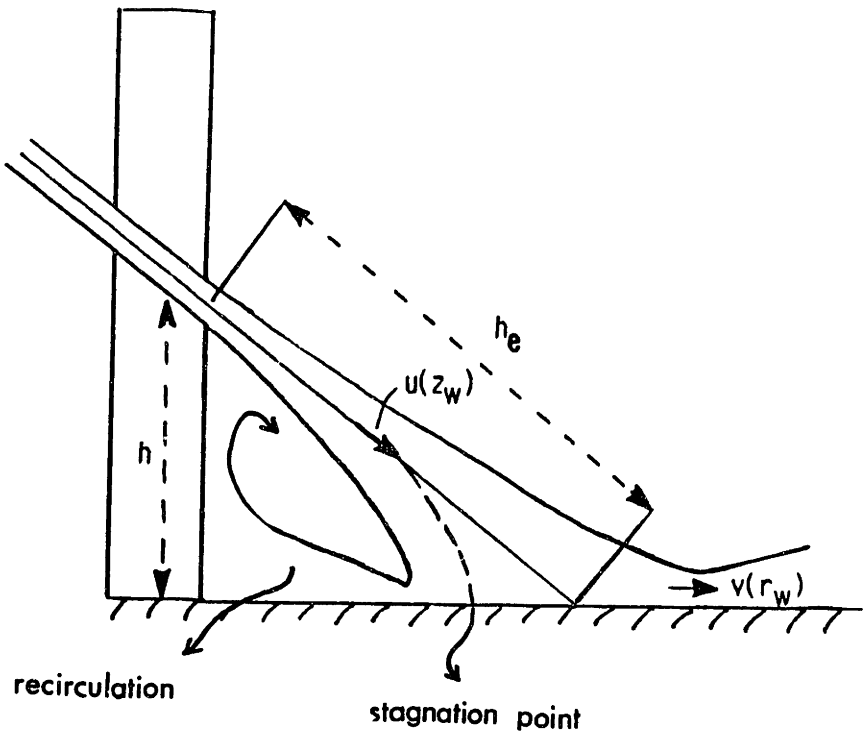

Figure 3.2 Angled jet impact. The relationship of the height of the jet above the impact surface, h and the effective height, h_e are illustrated. $u(z_w)$ is the axial jet velocity at the point above the surface where the jet is first influenced by the surface. $v(r_w)$ is the initial velocity of the downstream wall jet. The dashed line in the jet indicates the partition of flow between downstream wall jet and recirculation. It intersects the wall at the stagnation point. After [Martin, 1977].

Table 3.1 Impingement zone velocities using effective height and d = 0.381 cm.

Jet angle, θ (deg.)	Effective height, h_e (cm)	Velocity normal to the surface u(0.6d)	Velocity parallel to the surface v(0.6d)	v(1.2d)
10	5.5	-	-	-
19	2.9	3637	1819	3625
27	2.1	3970	1985	3970
90	0.95	4448	2224	4446

When the angle of impact differs from 90°, the flow is affected by factors other than the jet height. The flow volume may become distributed unevenly between the upstream and downstream wall jets. The position of the stagnation point moves upstream away from the projection of jet's axis as illustrated in figure 3.2. The number of stagnation points may change. A single stagnation point may become a line of stagnation points as the angle of impact decreases. The area of impact on a surface also changes with impact angle. As the impact angle increases the impact area decreases.

The flow which results from an angled jet in a tube depends on the distance from the jet nozzle to the tube walls, on the division of flow volume between upstream recirculation and downstream wall jet, and on the impact angle. For the angled models in this experiment, as θ increases the resulting force on the tube walls depends on a tradeoff between jet height and impact angle. The volume velocity in the downstream jet is constant because it is set via the air flow generating system and the whole system is allowed to come to steady state before recordings are made. The volume velocity of the flow returning to the jet is determined by the recirculation pattern of the impinging jet.

When the jet angle is varied in the tube, the proportion of sound sources produced from free jet turbulence to those produced by interaction with the tube wall or an obstacle change. As the jet angle increases, the free jet region of the air flow decreases and an impinging jet develops. The number of free jet quadrupole sources decreases as the length of the free jet portion decreases. Dipole sources produced upon impact with the wall or an obstacle become stronger with increasing jet angle because the axial flow velocity is increased. The effective number of dipoles produced depends on the impact area. For the model geometries, the area of impact is roughly proportional to 1/sin θ . There is a tradeoff between these two types of sources as jet angle changes. Free jet quadrupoles are

produced closer to the inlet of the tube than dipole sources. The sounds produced as the jet angle is varied are different because of this tradeoff between quadrupole and dipole production, differences in the locations and differences in the way quadrupoles and dipoles couple to the tube.

These differences in sound produced can be evaluated by using the 0° jet no-obstacle model as a threshold of comparison. The absolute level of radiated sound pressure from this model is a good level for comparison since most speech sounds have a higher SPL than this level at a distance of 26 cm from the mouth. As discussed in Ch. 2, the sound from this model is primarily due to the inlet noise monopole. To add more than 3 dB of SPL, the additional sound pressure must be greater than that of the monopole.

3.2 Acoustic Analysis of Mechanical Models

In this section, the theoretical transfer function, T(f) between a series pressure source and the volume velocity at the mouth of the tube is found for the mechanical models. A generalized representation of the mechanical models is shown in figure 3.3. The mechanical models can be represented by a tube of cross-sectional area A_t with one end open and the other joined to a short segment of tubing of area A_c. The air line attachment to the short tube can be represented by its characteristic impedance Z_1. The poles of T(f) are the natural frequencies of the model. Poles are independent of obstacle position. The obstacle perturbs the area function at the pressure source location, but the perturbation is small and to a first order can be neglected when calculating the poles and their bandwidths. The zeros of T(f) are a function of the pressure source (obstacle) location in the tube. Zeros must be calculated for each obstacle position. Zeros in the transfer function correspond to the natural frequencies of the configuration upstream of the source with a very large impedance at the source location. As a first approximation this impedance may be considered infinite. It also separates the back network from the radiation impedance. Therefore, the zeros are not affected by the radiation impedance.

The model may be analyzed as a distributed network for a certain range of frequencies. The upper frequency limit is defined by the frequency of the first cross mode in the large tube. For a rigid tube with radius a, the cutoff frequency for the $(m,n)^{th}$ mode is

$$f_{mn} = \alpha_{mn}\, c / 2a$$

The first cross modes to propagate are a pair for m = 1 and n = 0. $\alpha_{10} = 0.5861$ and corresponds to $f_{10} = 10{,}614$ Hz for a = 0.9525 cm [Morse and Ingard,1968]. For

frequencies below f_{10}, the model may be analyzed using transmission line analogies. A transmission line model is one-dimensional and the transmission line parameters depend on the cross-sectional area function, A(z). In applying this theory, assumptions will be made that lead to analytic expressions which are valid over a range of frequencies less than the cross mode. The large tube will be represented by two sections of transmission line, one on either side of the pressure source, and both sections will have characteristic impedance Z_0. The small tube will be grouped with the inlet (glottal) impedance.

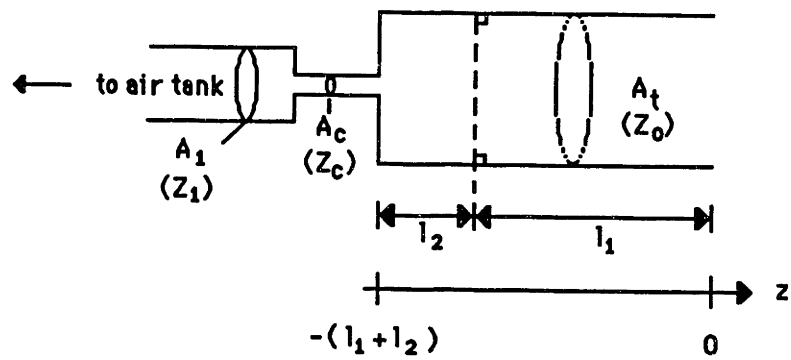

Figure 3.3 General model of the vocal tract. The characteristic impedance associated with each tube is given in parentheses next to the corresponding tube cross-sectional area. The z-axis and length variables for the analysis are indicated.

To begin, the transfer function will be found for the case of viscous and heat conduction losses only. The glottal and radiation impedances are taken to be ideally infinite and zero, respectively. Lumped elements can be used to model an incremental length of transmission line. Figure 3.4 contains diagrams of an incremental length of transmission line and the resulting circuit. Viscous losses are represented by the series resistance R, heat conduction losses by the shunt conductance G. The mass of the air in the tube is represented by the series inductance L and the compliance of the air by the capacitance C. These elements are per unit length quantities.

$$R = \frac{S}{A^2}\sqrt{\frac{\omega\rho\mu}{2}}$$

$$G = \frac{S(\eta - 1)}{\rho c^2}\sqrt{\frac{\lambda\omega}{2c_p\rho}}$$

$$L = \frac{\rho}{A}$$

$$C = \frac{A}{\rho c^2}$$

where ρ = air density = 1.19×10^{-3} g/cm^3 (1 atmos, 23°C)

A_t = tube area = 2.85 cm^2

S = tube circumference = $2\pi \cdot 0.9525$ cm

μ = viscosity coefficient = 1.86×10^{-4} dyne-sec/cm^2 (1 atmos, 20°C)

η = adiabatic constant of air = 1.4

c = velocity of sound = 3.45×10^4 cm/sec (1 atmos, 23°C)

λ = coefficient of heat conduction = 0.055×10^{-3} cal/cm-sec-deg (0°C)

c_p = specific heat of air at constant temperature

= 0.24 cal/g-deg (1 atmos, 0°C)

[Flanagan, 1972; Lange, 1949; Beranek, 1986]

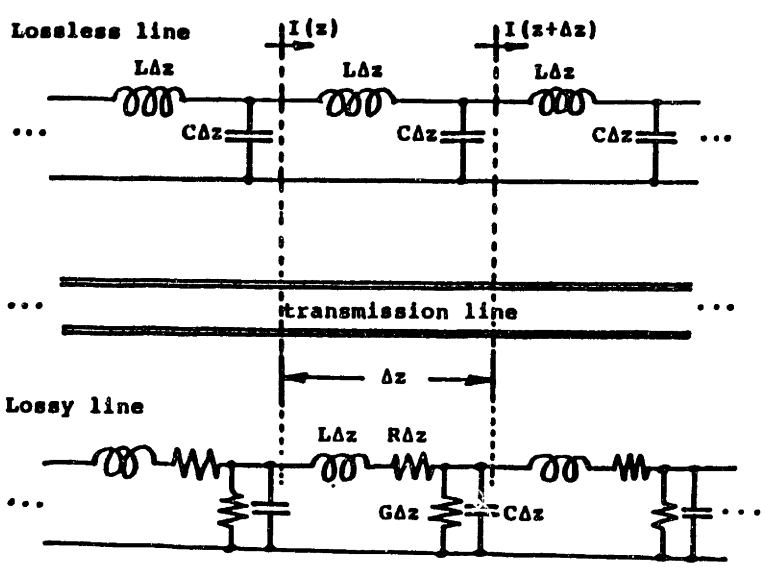

Figure 3.4 An incremental length of transmission line. After [Staelin and Kong, 1985].

With the ideal boundary conditions, one end open, one end closed, the transfer function between volume velocity at the mouth of the tube and a series pressure source for a lossy tube is

$$\frac{U(0)}{P(-l_1)} = \frac{1}{Z_0} \frac{\sinh \gamma l_2}{\cosh \gamma (l_1 + l_2)}$$

where l_1 and l_2 are defined in figure 3.3 and l_1+l_2 is equal to 17 cm, and Z_0 is the characteristic impedance of the tube of the model. The pole locations correspond to values of γ which make the denominator zero and the numerator non-zero.

$$\cosh \gamma(l_1+l_2) = 0$$
$$\text{where} \quad \gamma = \alpha + j\beta = \{(R + j\omega L)(G + j\omega L)\}^{1/2}$$

Using the parameter values on the previous page, the lumped elements become: $R = 6.14 \times 10^{-4}\ f^{1/2}\ g/cm^5\text{-sec}$, $G = 1.31 \times 10^{-6}\ f^{1/2}\ cm^3\text{-sec/g}$, $L = 4.18 \times 10^{-4} g/cm^5$ and $C = 2.01 \times 10^{-6}\ cm^3\text{-sec}^2/g$. The square root can be approximated if $R \ll \omega L$ and $G \ll \omega C$ [Potter and Fich, 1963; Staelin and Kong, 1985].

$$\gamma = j\omega\sqrt{LC}\left[\left(1 + \frac{R}{j\omega L}\right)\left(1 + \frac{G}{j\omega C}\right)\right]^{1/2}$$

$$\cong j\omega\sqrt{LC}\left(1 + \frac{R}{j2\omega L} + \frac{G}{j2\omega C}\right)$$

For these values, γ satisfies these conditions for frequencies greater than 1 Hz.

$$\gamma \cong \alpha + jB = \frac{R}{2}\sqrt{\frac{C}{L}} + \frac{G}{2}\sqrt{\frac{L}{C}} + j\omega\sqrt{LC}$$

γ is the complex wavenumber and as such has units equivalent to those of complex frequency divided by sound speed or inverse length. From linear system theory, the bandwidth of a pole or zero is twice the real part of the complex frequency. This relationship is shown is figure 3.5. The bandwidth of a pole or zero due to viscous and heat conduction losses, Δf_{vh} is equal to

$$\Delta f_{vh} = \alpha\, c/\pi.$$

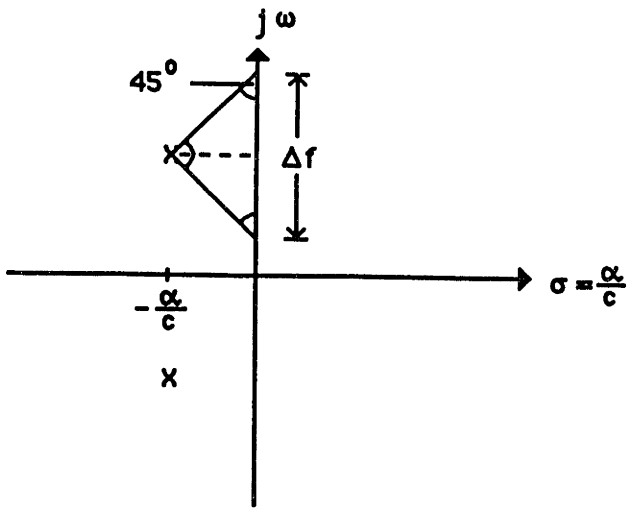

Figure 3.5 Complex pole - zero plane.

Next consider the addition of radiation impedance to the open end of the tube. Modeling the acoustic behavior of the tube as that of a piston in a long tube, the radiation impedance takes the following form for ka < 1.3, where k is defined as the wavenumber (cm^{-1}) [Beranek, 1986].

$$Z_R = Z_0 \, [\, 0.25 \, (ka)^2 \; + \; j \, 0.613 \, ka \,]$$

The formula is valid for frequencies up to 7500 Hz for a = 0.9525 cm. Including Z_R in the model, the denominator of the transfer function retains the same form it had previously [Shadle, 1985]. The poles satisfy

$$\cosh(\gamma + \gamma_R \,) \, (l_1 + l_2) = 0$$

$$\gamma_R = \alpha_R + j\beta_R = \tanh^{-1} \left(\frac{Z_R}{Z_0}\right)$$

The Taylor's series expansion of $\tanh^{-1} x$ is

$$\tanh^{-1} x = x + \frac{x^3}{3} + \frac{x^5}{5} + \ldots$$

For frequencies below 5000 Hz, the first term of the expansion makes a good approximation to the entire expression. At 5500 Hz, the first term is five times larger than the second. At 6000 Hz, the first is three times the second. In this analysis,

$$Y_R \cong \left(\frac{Z_R}{Z_0}\right)$$

$$\alpha_R \cong \left(\frac{1}{l_1 + l_2}\right) \mathrm{Re}\left(\frac{Z_R}{Z_0}\right) = \frac{0.25\,(ka)^2}{(l_1 + l_2)}$$

$$\beta_R \cong \left(\frac{1}{l_1 + l_2}\right) \mathrm{Im}\left(\frac{Z_R}{Z_0}\right) = \frac{0.613\,ka}{(l_1 + l_2)}$$

This is equivalent to scaling the complex pole frequencies, s_n [Flanagan, 1972].

$$s_n \cong \frac{1}{\left(1 + \frac{\beta_R}{\beta}\right)} \left(-(\alpha + \alpha_R) \pm j\frac{(2n+1)\pi}{2(l_1 + l_2)} \right)$$

where n = 0,1,2,...

$$\frac{1}{\left(1 + \frac{\beta_R}{\beta}\right)} = \frac{1}{1 + \frac{0.613\,a}{(l_1 + l_2)}}$$

The scaling factor is also known as the end correction. A mass moving out of a tube into a larger opening will proceed as if it was still surrounded by the tube for a short distance due to its inertia. The effect of this on resonant frequencies is the same as making the tube length slightly longer in the calculations [Beranek,1986; Morse and Ingard,1968; Stevens, 1987]. The resulting resonant frequency and corresponding bandwidth, Δf_r are

$$f = \frac{(2n+1)c}{4(l + 0.613a)}$$

$$\Delta f_r = \frac{(0.25)(ka)^2 c}{\pi(l + 0.613a)} \qquad , n = 0,1,2,\ldots \quad l = l_1 + l_2$$

The difference between the ideal resonant frequency and that calculated above is tabulated in Table 3.2 as Δf_n.

These results may also be found using the perturbation method of solution. The glottis impedance calculations will be derived in this way. The perturbation method assumes that the additional impedance does not substantially change the distribution of volume velocity and sound pressure in the tube at a natural frequency. For the radiation impedance this means that $Z_R \ll Z_o$. As has been seen, this condition is not absolutely true for frequencies greater that 5000 Hz and will result in slightly larger values of resonant frequency and bandwidth than exist.

Table 3.2 Poles and bandwidths for the mechanical models

Legend:

f_n	resonant frequency of a lossless tube
Δf_n	change in resonant frequency due to radiation
Δf_c	change in resonant frequency due to glottal inductance
Δf_{vh}	bandwidth contribution due to viscous and heat conduction losses
Δf_r	bandwidth contribution due to radiation loss
Δf_{cg}	bandwidth contribution due to glottal constriction loss
f_{tot}	resultant pole frequency
Δf_{tot}	resultant pole bandwidth

POLES: $f_n = (2n-1)c/4(l_1+l_2)$; $n = 1, 2, 3, \ldots$

n	f_n	Δf_n	Δf_c	Δf_{vh}	Δf_r	Δf_{cg}	f_{tot}	Δf_{tot} (Hz)
1	507	- 16	+10	8	1	46	501	55
2	1522	- 50	+13	13	11	20	1485	44
3	2537	- 82	+10	17	30	10	2463	57
4	3551	-117	+ 8	20	59	5	3442	84
5	4566	-151	+ 7	23	98	3	4422	124
6	5581	-185	+ 6	25	146	2	5402	173

The glottal constriction adds loss in two ways. One loss results from the air line and inlet structure connected to the short length of glottal tubing. The air line back to the air tank is long enough to attenuate any reflections back towards the glottis that may occur at a bend in the air line or at the flowmeter. Only a small percentage of the reflections in the

tube directed towards the glottis pass into the glottis opening, since the area of the glottis is much smaller than that of the tube. Of these reflections, some will be reflected at the manometer connections back towards the glottis and the rest will be attenuated by the air line leading to the air tank. Glottis bound reflections will be attenuated by passing through the air line section between the manometer and glottis tubing. They will also encounter the discontinuity in area of the air line glottis connection, dividing into a reflected wave and a transmitted wave. The reflected waves returning to the tube will contribute negligible flow compared to the flow in the tube. Therefore, for frequencies above about 750 Hz, the air line can be modeled as an infinitely long transmission line with characteristic impedance Z_l (A_l = 0.317 cm^2) looking into the glottal end of the air line. The glottis tubing constricts the air flow adding loss like any length of pipe containing fluid flow. The resistance of the glottal tubing, R, relates the instantaneous pressure and volume velocity. Sound results from fluctuations in pressure and volume velocity from their rms values; thus, the loss due to the constriction should be calculated from the incremental resistance of the tubing, $R_c = dR/dU$ [Flanagan,1972; Shadle, 1985]. The air mass in the tube is also included in the impedance. It has some inertia, which is accounted for in the inductance term of the glottal impedance. Figure 2.6a shows the details of the input flow connections. For this analysis, these elements will be modeled by the circuit elements in figure 3.6. The input air line characteristic impedance is in series with the incremental resistance and the mass of the constriction tubing. The fundamental equations for these elements are included in figure 3.6. Only slight coupling occurs between the inlet tubing and the tube, since the area difference between them is great. A series of pole-zero pairs due to the input structure result, but have very little effect on the transfer function.

The method of perturbation analysis is used to calculate the bandwidth and resonant frequency shift which result from a transmission line with small losses and small reactive end effects. The quality factor, Q can be used to calculate these quantities, and measures the number of cycles necessary to dissipate the energy stored in the system.

$$Q = \frac{2\pi f \cdot (\text{energy stored in circuit})}{\text{average power dissipated per cycle}} = \frac{f}{\Delta f}$$

The calculation of f and Δf for the poles of the tube will be used as an example, highlighting the steps of perturbation analysis. The glottal impedance deviates from the ideal case of infinite impedance; however, the deviation will not greatly influence the pressure at the end of the tube. $R_c >> Z_o$ and the pressure is a maximum at the glottal end of the tube. On

the other hand, the volume velocity there could deviate substantially from its value of zero in the ideal case. Figure 3.3 contains a schematic of the tube for this analysis. The inlet of the tube is located at z = -l and the mouth of the tube at z = 0. The following equations are used to find the bandwidth contribution due to the glottal constriction, Δf_{cg}, where P(-l) is sound pressure in phase notation at the inlet of the tube and where f is taken as the resonant frequency of the tube with ideal boundary conditions.

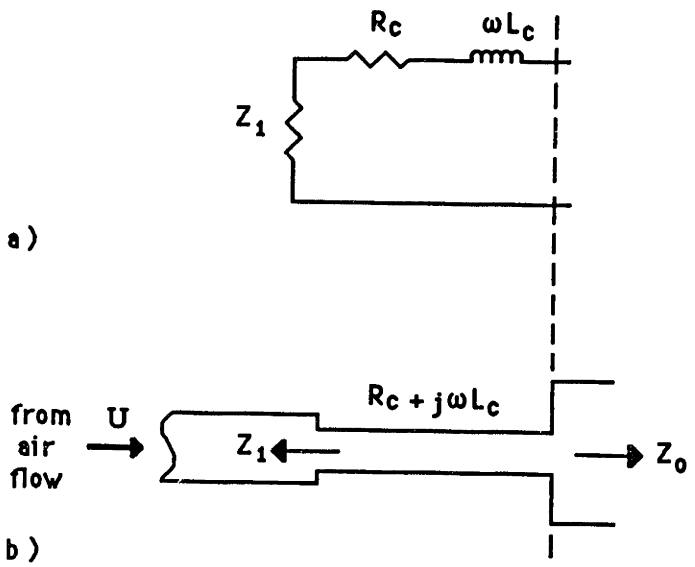

$$Z_1 = \frac{\rho c}{A_1}$$

$$Z_0 = \frac{\rho c}{A_t}$$

$$Z_c = R_c + j\omega L_c$$

$$R_c = \frac{\rho U}{A_c^2}$$

$$L_c = \frac{\rho l c}{A_c}$$

Figure 3.6 Inlet circuit and model.

$$\text{energy stored in tube} = \frac{A_t l\,|P(-l)|^2}{4\rho c^2}$$

$$\text{average power dissipated} = \frac{R_c}{2}\,\frac{|P(-l)|^2}{|(Z_1+R_c)^2+\omega^2 L_c^2|}$$

$$Q = \frac{\pi f A_t l\,|(Z_1+R_c)^2+\omega^2 L_c^2|}{\rho c^2 R_c}$$

$$\Delta f_{cg} = \frac{f}{Q} = \frac{\rho c^2 R_c}{\pi A_t l} \cdot \frac{1}{|(Z_1 + R_c)^2 + \omega^2 L_c^2|}$$

[Potter and Fich,1963; Staelin and Kong, 1985; Stevens, 1987; Shadle, 1985]

To find the fractional increase in resonant frequency,

$$\begin{matrix}\text{average energy} \\ \text{stored per unit time}\end{matrix} = \frac{\omega L_c}{2} \frac{|P(-l)|^2}{|(Z_1 + R_c)^2 + \omega^2 L_c^2|}$$

$$\Delta f_c = \frac{\rho c^2 L_c f}{A_t l \; |(Z_1 + R_c)^2 + \omega^2 L_c^2|}$$

The bandwidth and frequency shifts due to finite glottal impedance for poles and zeros were calculated in this manner. The following values were used: $Z_1 + R_c = 170$ g/cm^4-sec, $L_c = 0.023$ g/cm^4, $R_c = 40.5$ g/cm^4-sec, $A_t = 2.85$ cm^2 and $l = 17.0$ cm. The length of the back cavity varied for the zero calculations due to the position of the obstacle. Note that the sources produced at the obstacle are probably not at a single location so, in effect, the zero is spread out.

Tables 3.2 and 3.3 list the bandwidths and resonant frequency shifts for poles and zeros, respectively. The net resonant frequency f_{tot} and the total bandwidth Δf_{tot} are indicated. These numbers were used to calculate the transfer functions from a series pressure source input at the obstacle location to volume velocity at the tube mouth.

For each obstacle location, there is a low frequency zero not included in Table 3.3. To find the frequency of this zero a low-frequency model of the input flow connections can be made from lumped elements. A model containing the elements for each piece of tubing shown in figure 2.6a has a transfer function with a sixth order numerator and fifth order denominator: one unbound real zero, one real pole-zero pair and two complex pole-zero pairs. The unbound zero is located below 100 Hz for each obstacle location. For the frequency range of 1000 to 6000 Hz, the low frequency response can be represented by a single zero at 0 Hz indicative of the capacitance of the back cavity. The transfer function between volume velocity at the mouth of the tube, U(0) and the series pressure source, $P(-l_1)$ is

Table 3.3 Zeros and bandwidths for the mechanical models

Legend:

Δf_c	change in resonant frequency due to glottal inductance
Δf_{vh}	bandwidth contribution due to viscous and heat conduction losses
Δf_{cg}	bandwidth contribution due to glottal constriction loss
f_{tot}	resultant zero frequency
Δf_{tot}	resultant zero bandwidth

ZEROS: $f_n = nc/2l_2$; $n = 0, 1, 2, 3, \ldots$
For all l_2, there is a real zero located below 100 Hz.

l_2 (cm)	n	f_n	Δf_c	Δf_{vh}	Δf_{cg}	f_{tot}	Δf_{tot} (Hz)
3.0	1	5750	+31	26	13	5781	38
4.0	1	4313	+30	22	16	4342	38
5.0	1	3450	+28	20	19	3478	39
6.0	1	2875	+27	18	22	2902	40
	2	5750	+15	26	6	5765	32
7.0	1	2464	+26	17	25	2490	42
	2	4929	+15	24	7	4944	31
8.0	1	2156	+25	16	27	2181	42
	2	4313	+15	22	8	4327	30
9.0	1	1917	+23	15	28	1940	43
	2	3833	+15	21	9	3848	30
	3	5750	+10	26	4	5760	30
10.0	1	1725	+22	14	30	1747	44
	2	3450	+14	20	10	3464	30
	3	5175	+10	24	5	5185	29
11.0	1	1568	+20	13	31	1589	44
	2	3136	+14	19	10	3150	29
	3	4705	+10	23	5	4715	28
12.0	1	1438	+19	13	31	1457	44
	2	2875	+14	18	11	2889	29
	3	4313	+10	22	5	4322	28
	4	5750	+ 8	26	3	5758	29
13.0	1	1327	+18	12	32	1345	44
	2	2654	+13	17	12	1667	29
	3	3981	+10	21	6	3991	27
	4	5308	+ 8	25	3	5315	28
14.0	1	1232	+17	12	32	1249	44
	2	2464	+13	17	12	2477	29
	3	3696	+10	21	6	3706	27
	4	4929	+ 8	24	4	4936	27
15.0	1	1150	+16	11	32	1166	43
	2	2300	+13	16	13	2313	29
	3	3450	+10	20	7	3460	26
	4	4600	+ 7	23	4	4607	27
	5	5750	+ 6	26	3	5756	28
16.0	1	1078	+15	11	32	1093	43
	2	2156	+12	16	13	2168	29
	3	3234	+ 9	19	7	3244	26
	4	4313	+ 7	22	4	4320	26
	5	5391	+ 6	25	3	5397	27

$$\left|\frac{U(0)}{P(-l_1)}\right| = \frac{2\pi f\, l_2 A_t}{\rho c^2} \cdot T'(f) = T(f)$$

where the higher order zero and pole terms are represented by T'(f). For frequencies from 350 to 750 Hz, error may result from using the above expression because the real pole-zero pair may be located in this frequency range. The closer the pole and zero in the complex frequency plane, the more completely they will cancel each other, and the smaller the error in this approximation.

The pole and zero values listed in Tables 3.2 and 3.3 were inputted into transf.for, a program written by Shadle, residing on MIT Speech (Dec-20). This program calculates the transfer function, T'(f), from the input poles and zeros with a higher pole, zero correction option. T'(f) is tabulated in Appendix B, Table B.6. The results of this analysis will be used in the following section.

3.3 Analysis of the Corrected Data

In each set of models with the same jet angle, the sound originates from several sources in the tube and from the inlet monopole source. Most of the sound sources in the tube are the same for models with the same jet angle. Sources rising from flow-obstacle interactions differ from model to model and depend on the location of the obstacle for models with the same jet angle. The ambient sound field for a given jet angle is due to the fixed sources: the inlet monopole, quadrupoles in the free jet region of flow, and sources produced at the smooth walls of the tube by an impinging jet. It was calculated from the corrected data by averaging the data of the 12 to 16 cm and no-obstacle models for each jet angle. The resulting SPL are listed in Table 3.4.

Table 3.4 Average magnitude (dB SPL in 50 Hz bins) for no-obstacle models.

Jet angle, θ (degs.)	Resonant frequencies, F_n F1	F2	F3	F4	F5	F6
0°	43.3	50.1	44.0	41.9	41.1	36.6
10°	42.7	50.1	44.5	41.7	41.8	34.9
19°	40.3	50.4	45.0	40.0	41.7	36.6
27°	40.0	50.3	44.0	39.9	43.0	37.4
90°	39.9	47.6	41.4	37.8	34.2	28.5

For jet angles 0° to 27° the values of average SPL are comparable. The largest spread for any resonant frequency, excluding F1, is 2.5 dB for F6, which is probably due to the lower SNR for F6 data. The average SPL for F1 decreases consistently with increasing jet angle, corresponding to decreasing effective jet height, h_e. Effective height is illustrated in figure 3.2. Large changes in effective height are reflected in large changes of F1 average SPL. For jet angles larger than about 25°, the effective height changes much less with angle than for smaller jet angles and the F1 average SPL becomes stable at about 40 dB. The average SPL is more dependent on effective height at F1 than at other frequencies, since turbulent sources farther from the nozzle have relatively more low frequency content than those close to the nozzle. For all jet angles, the average SPL reaches a maximum amplitude at F2 and decreases as a function of F_n for frequencies greater than F2.

For a jet angle of 90°, the average SPL decreases more rapidly with F_n than for other jet angles. The locations of the inlet monopole and free quadrupole sources near the inlet of the 90° jet no-obstacle model differ from those of the other no-obstacle models. Inefficient coupling results at higher frequencies, as discussed in section 2.7. The sound recorded from the 90° jet no-obstacle model is attributed to the inlet monopole. The difference between it and that of the 0° jet no-obstacle model at high frequency should be due solely to coupling. Shear dipole sources do not significantly add to the SPL.

The data for models with annular obstacles were analyzed within the context of a linear input-output system with negligible source-tract interaction. The spectrum of pressure sources $S_i(f)$ produced by flow-obstacle interactions at obstacle locations z_i will be estimated using the experimental results of Ch. 2, the transfer functions calculated in the previous section, and a point source approximation of the radiation characteristic of the tube, R(f). The portion of the transfer function associated with a pressure source located at z_j which does not include the low-frequency zero term is called $T_j(f)$. $N_j(f)$ is its numerator. Its denominator is D(f), which is the same for all sources.

The recorded sound due to sources in the tube other than those present in the corresponding no-obstacle model, $P_i(f)$ can be described by:

$$P_i(f) = \frac{R(f)}{D(f)} \cdot \frac{2\pi f l_2 A_t}{\rho c^2} \cdot \underbrace{\sum_j S_j(f) N_j(f)}_{\text{additional sources in tube}}$$

$$T_j(f) = \frac{N_j(f)}{D(f)}$$

The only significant additional sources in a model with an annular obstacle occur at the obstacle, and thus $z_i = z_j = l_2$. The total sound pressure recorded P(f) results from the root of the sum of the squares of the no-obstacle SPL and $P_i(f)$, assuming that sources from different locations are incoherent.

To isolate the portion of the total sound pressure P(f) due to the obstacle at z_i, P(f) and the numbers in Table 3.4 were squared and subtracted from each other for each particular model, respectively. The data with values greater than or equal to the no-obstacle averages are noted. These are the points (θ, l_2, F_n) which have significant additional sound pressure due to the obstacle at location l_2. Points with values lower than those given in Table 3.4 may contribute sound energy from obstacle sources, but for the purposes of this analysis the sound is masked by the ambient noise and is more uncertain due to low SNR.

In the next step of calculating the pressure source spectrum from the energy density spectrum for each obstacle location, the radiation characteristic was approximated as that of a monopole at the mouth of the tube. The monopole model is valid for several reasons. The distance between the tube mouth and the microphone r is large compared to the tube diameter; the tube mouth is a small source. For frequencies of interest, the tube has a circular directivity pattern and the radiation can be considered isotropic. A small isotropic source is a monopole. The radiation characteristic is given by

$$|R(f)| = \frac{\rho f}{2r}$$

To calculate the source spectra $S_i(f)$, terms due to radiation and the common low-frequency zero are subtracted from $P_i(f)$. The spectrum of the pressure source $S_i(f)$ located at the obstacle location is described by the following equation.

$$\left| \frac{S_i(f) N_i(f)}{D(f)} \right|_{dB} = |P_i(f)|_{dB} - 20 \log_{10} \frac{2\pi f l_2 A_t}{\rho c^2} \cdot R(f)$$

$S_i(f)$ can be found by subtracting $T_i(f)$ from the result. The resulting $S_i(f)$ are corrected for the 50 Hz bandwidth of the cosine window by subtracting 17 dB. These manipulations yield valid data for the points which have significant additional sound pressure. $S_i(f)$ are listed in Tables B.7 to B.11 in Appendix B. Plots of $S_i(f_n)$ for each angle and several obstacle locations are shown in figures 3.7 to 3.11. The smooth curves in each graph result from fitting a logarithmic curve to the data [Rafferty and Norling, 1986]. The

graphs of figures 3.7b and 3.8b contain curves fitted to data of more than one obstacle location. These graphs illustrate the general trends of the data. The equations of the fitted curves in figures 3.7a and 3.8a were used to group obstacle locations together. The equation parameters are listed in Table B.12 in Appendix B. For instance in figure 3.7b, obstacle locations 3 and 4 cm and 1, 2 and 5 cm are grouped together. The corresponding equations are:

Equation: $y = a \cdot (freq)^b$

Obstacle location (cm)	a	b
1	207.6	-0.149
2	205.5	-0.147
3	226.8	-0.152
4	229.0	-0.158
5	193.6	-0.139

Figures 3.7b and 3.8b indicate that above about 1000 Hz, the source spectra of the 0° and 10° jet models have approximately the same shape. Thus, the spectra of pressure sources located 1 to 6 cm from the tube inlet differ approximately by an additive constant (dB). Figure 3.11 shows the source spectra for the 90° jet models. No curves are fitted to the data. The F3 data points for all jet angles appear to be lower in value than would be predicted from the data points on either side of them. The F1 data points are less reliable than the data at other frequencies since the low-frequency assumptions used to calculate the tube transfer function were not valid for frequencies less than 750 Hz. The transfer function was only approximate for frequencies less than 750 Hz. Consequently, the low-frequency behavior of the curve fitted to the source spectra data is probably not correct.

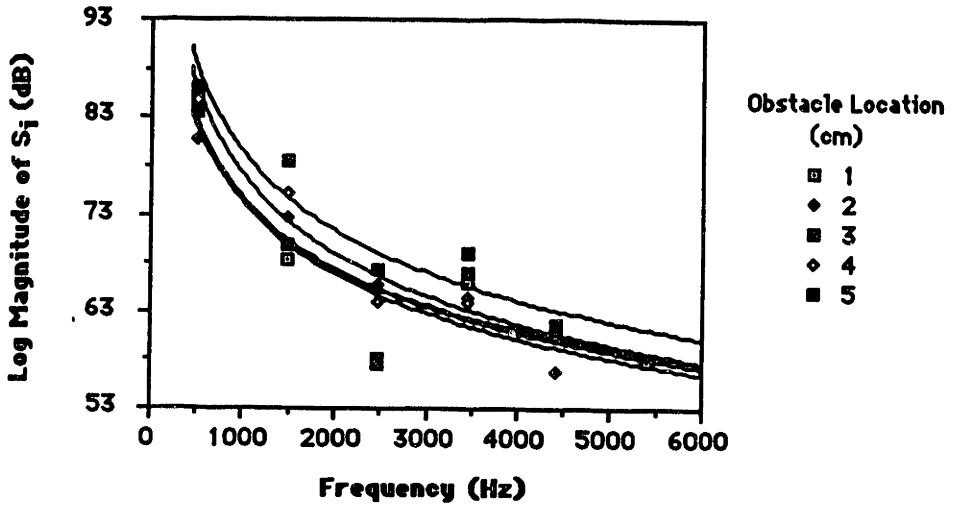

a) Source spectra for 0° jet models with obstacle locations of 1 to 5 cm.

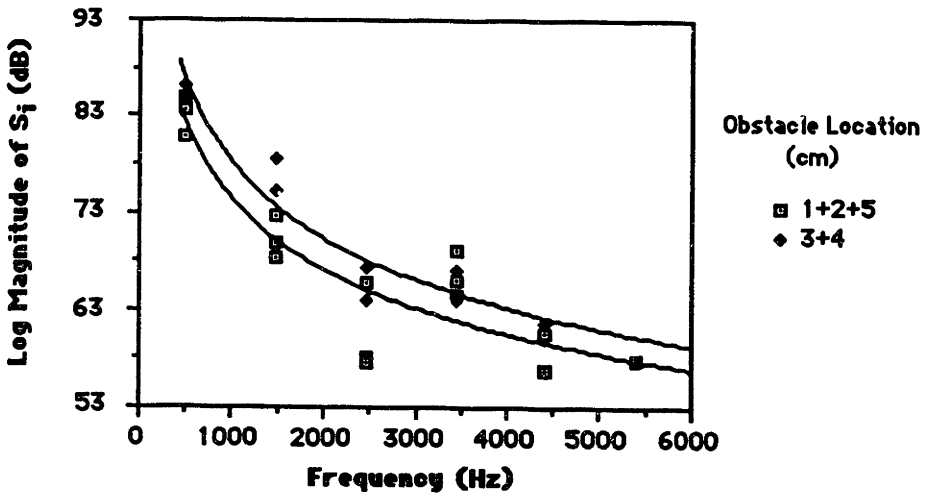

b) Combined source spectra for 0° jet models

Figure 3.7 Source spectra for 0° jet models.

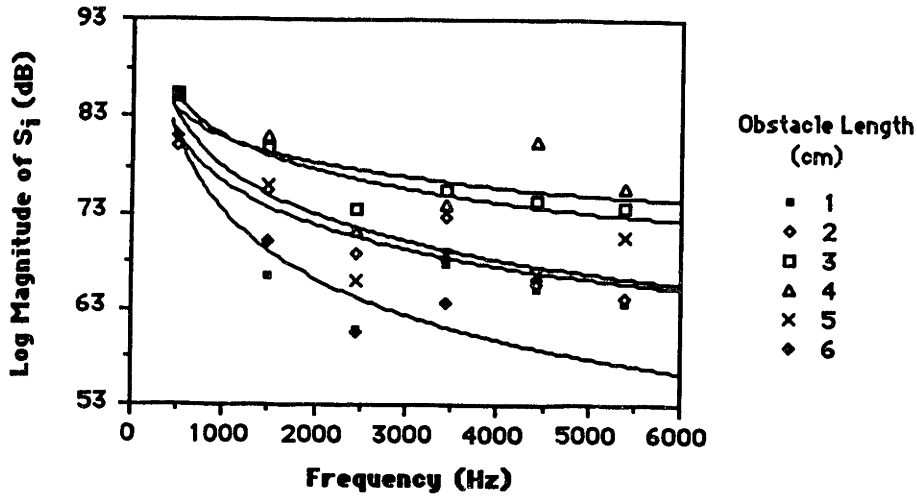

a) Source spectra for 10° jet models with obstacle locations of 1 to 6 cm.

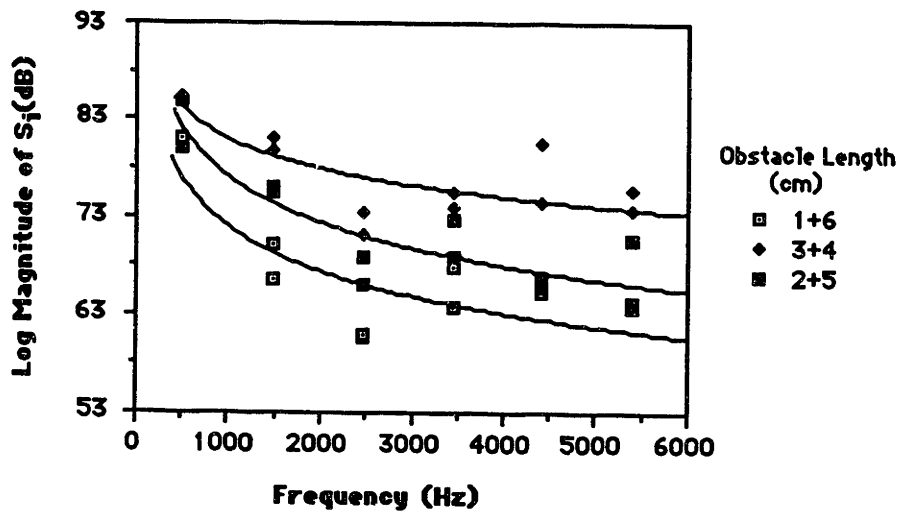

b) Combined source spectra for 10° jet models

Figure 3.8 Source spectra for the 10° jet models.

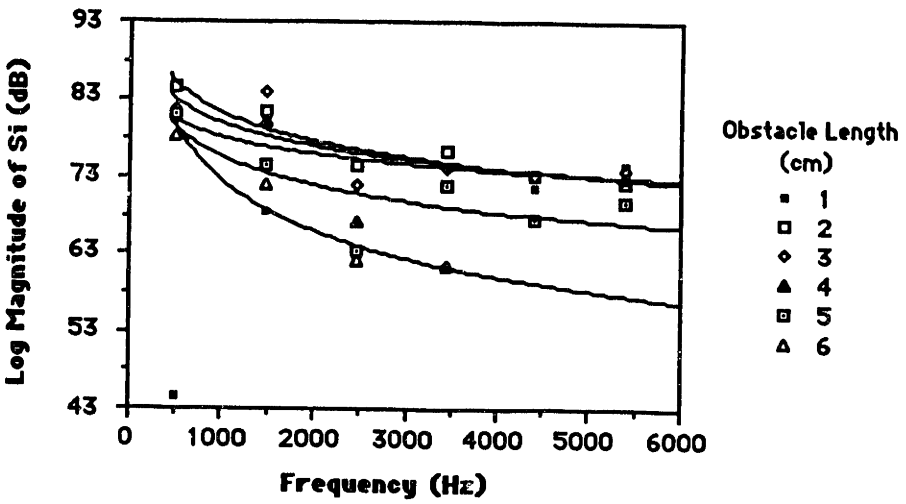

Figure 3.9 Source spectra for 19° jet models with obstacle locations of 1 to 6 cm.

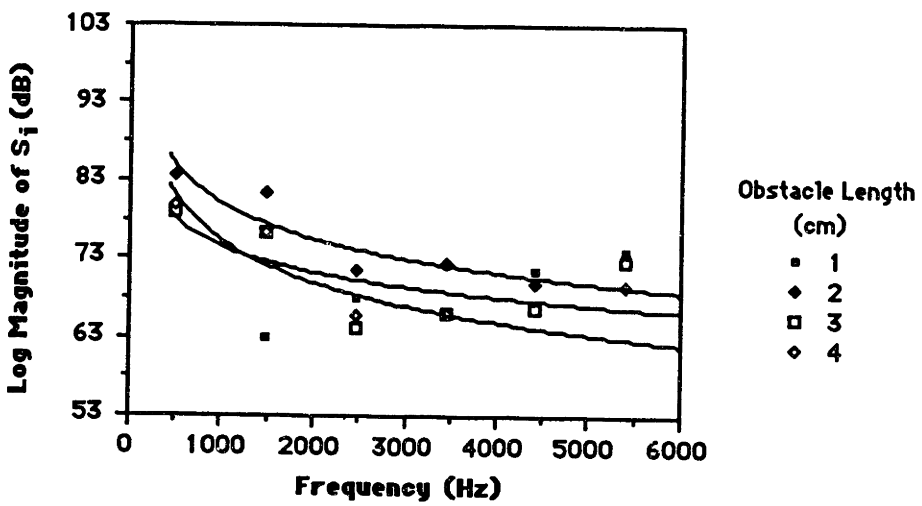

Figure 3.10 Source spectra for 27° jet models with obstacle locations of 1 to 4 cm.

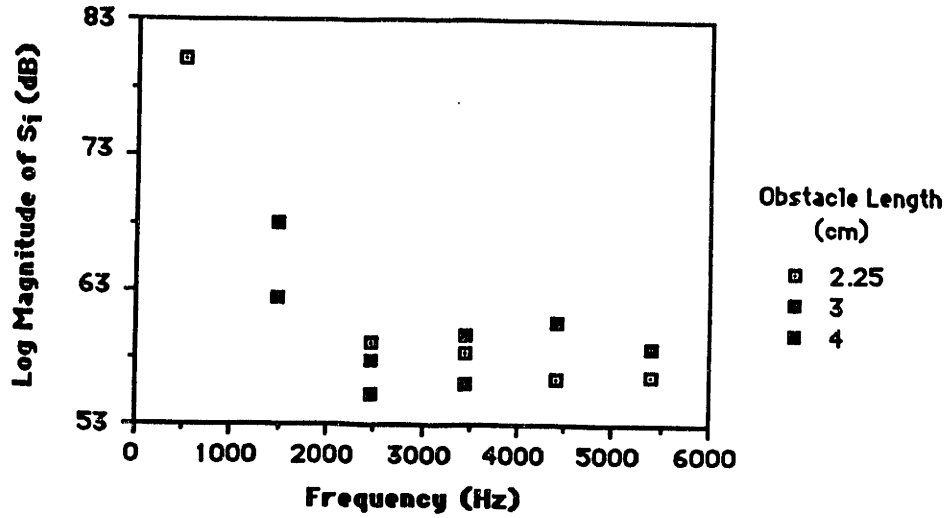

Figure 3.11 Source spectra for 90° jet models with obstacle locations of 2.25 to 4 cm.

3.4 Discussion

The radiated sound pressure spectra of the no-obstacle models are not greatly affected by jet angle. Table 3.4 lists SPL values for the no-obstacle models. As the jet angle increases from 0°, the spectral energy density of the first six resonant frequencies decreases or stays constant. The spectral energy density of the first resonant frequency is roughly proportional to effective jet height, as shown in section 3.3. Energy density peaks at the second formant. For angles 0° to 27° and frequencies above F1, the spectra are approximately the same within 2.5 dB of scatter. However, the 90° case decreases faster than the others as a function of F_n. The location of the monopole is different in the 90° configuration, which results in a change in coupling coefficient from unity to $\cos((2n-1)z\pi/2l)$, where n is the mode number. For the most part, the sound due to the inlet monopole and free quadrupoles dominates that due to shear dipoles at the wall in the smooth wall no-obstacle case.

After the calculations described in sections 3.2 and 3.3, the source spectra can be considered. Figures 3.7 to 3.11 give an indication of the shape and level of each spectrum. For each angle, spectra from several obstacle locations are plotted. The figures contain smoothed curves. Formulas of these curves are listed in Appendix B, Table B.12. Curves of this type will be used to approximate the source spectra of the speech sound /h/.

The pressure source produced by a jet of air impinging upon a large obstacle in the

mouth of a tube was calculated from sound recordings from an experimental model by Shadle [Shadle, 1985]. The obstacle was located 3 cm from the constriction, in the tube where the jet of air was formed. The pressure source from Shadle's model can be compared to that of the 0° jet 3 cm model. Smooth curves representing both source spectra are shown in figure 3.12a. The placement and size of the obstacle in each model are compared in figure 3.12b. The amplitude of Shadle's pressure source is approximately 20 dB greater than that of the 0° jet 3 cm model. The difference in amplitude can be explained by the differences in the obstacles. The annular obstacle in the 0° jet 3 cm model has very little surface area compared to that of the obstacle in Shadle's model. It also is placed farther than a half radius from the center of the jet, while the obstacle in Shadle's model covers one-half of the jet. The average changes in amplitude of the source spectra between 2000 and 6000 Hz are 3.25 dB/ 1000 Hz for Shadle's source and 3.13 dB/ 1000 Hz for the 0° jet 3 cm model. The source spectra have approximately the same shape above 2000 Hz. The third curve in figure 3.12a shows the result of extrapolating the low-frequency spectrum of the 0° jet 3 cm model using the spectral shape of Shadle's pressure source as a guide.

As previously discussed in Ch. 2 , the maximum amplitudes of the radiated spectra are greatest between 10° and 20° of jet angle for all F_n. Figure 2.17 shows the radiated sound pressure peak magnitude versus jet angle for the first six resonant frequencies. A similar graph for source spectra peak magnitude is shown in figure 3.13. Source amplitude is greatest for F1 and F2 and lowest for F3, F4, and F6. The amplitude of the radiated sound pressure at a particular frequency depends on the energy density of the source at that frequency and on how well the source couples to the sound field at that frequency. For instance, in the 10° to 20° jet angle range, the peak source magnitude for F4 is about the same as that of F6. The peak radiated sound pressure at F4 is much greater than that of F6. The peak source of F4 coupled to the sound field much more efficiently than did the peak source of F6.

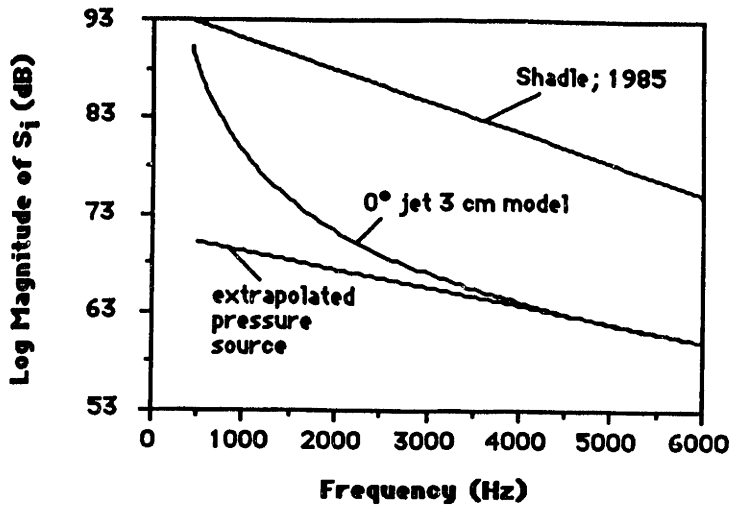

a) Smooth curves representing source spectra produced in flow-obstacle interactions in the models shown in b) and c).

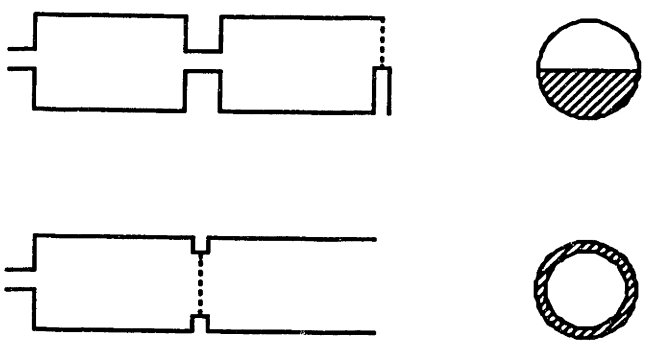

b) Schematic views of the two models compared in a). The upper schematic is a drawing of Shadle's model. The lower is a drawing of the 0° jet 3 cm model. Cross-sectional views are taken at the obstacle location (dashed line) in each model. Obstacles are located 3 cm from the constriction in Shadle's model and 3 cm from the inlet in the 0° jet 3 cm model.

Figure 3.12 Comparison of the source spectra of Shadle's model and the 0° jet 3 cm model. [Shadle, 1985].

In figures 3.14 to 3.17, the source spectra amplitudes for a particular F_n are plotted versus obstacle location for the five values of jet angle. For any single angle, the data are a good fit to a second order polynomial. For the first four resonant frequencies, the source sound pressure passes through a maximum between 0° and 19° jet angle. There are not enough data to determine any pattern for the fifth and sixth resonant frequencies. If

changing the jet angle increases the source magnitude at a particular obstacle location, the source magnitude generally is increased at all obstacle locations. When the source level at all locations increases, the overall length of the source region increases. For angles near 0°, a large area of impact is present, but velocity is small. As the angle increases to the 10° to 25° range, the area is still fairly large and collision velocity is large. From 25° to 90°, the area falls off and dipole orientation becomes an important factor in determining how much sound pressure is radiated from the tube.

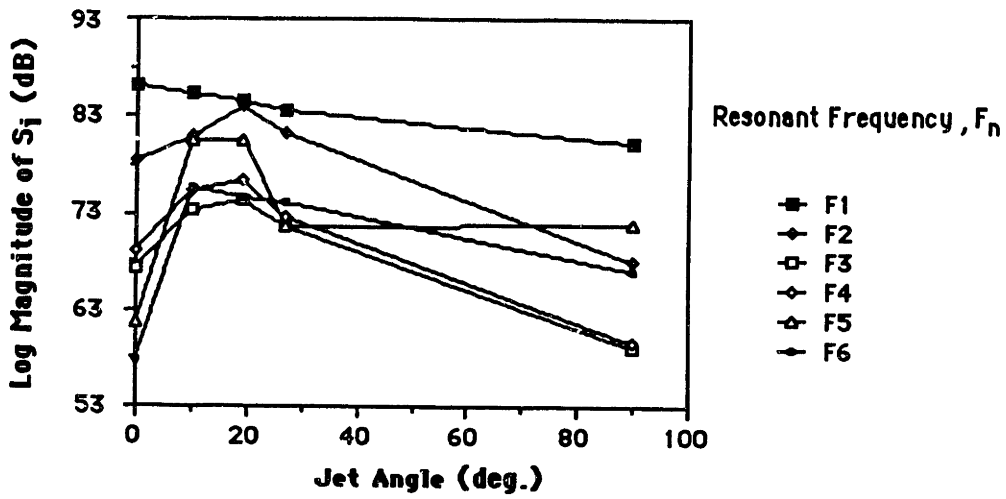

Figure 3.13 Source spectra peak magnitude versus jet angle.

The sound pressure increase due to the obstacle in these experiments can be compared to the increase due to the larger obstacles Shadle introduced into the tube during her experiments. Depending on its shape and location, Shadle found the obstacle could add 20 dB or more to the absolute sound pressure level [Shadle, 1985] . The approximate maximum increase due to the annular ring jet for each jet angle is between 10 to 15 dB except for the 90° model which adds about 5 dB. The absolute sound pressure level due to sources at an obstacle depends on the shape and placement of the obstacle, and thus on the strength and orientation of the resulting source.

In summary, the source spectra calculated in these experiments represent the spectra at points along the distributed pressure source created by an impinging jet.

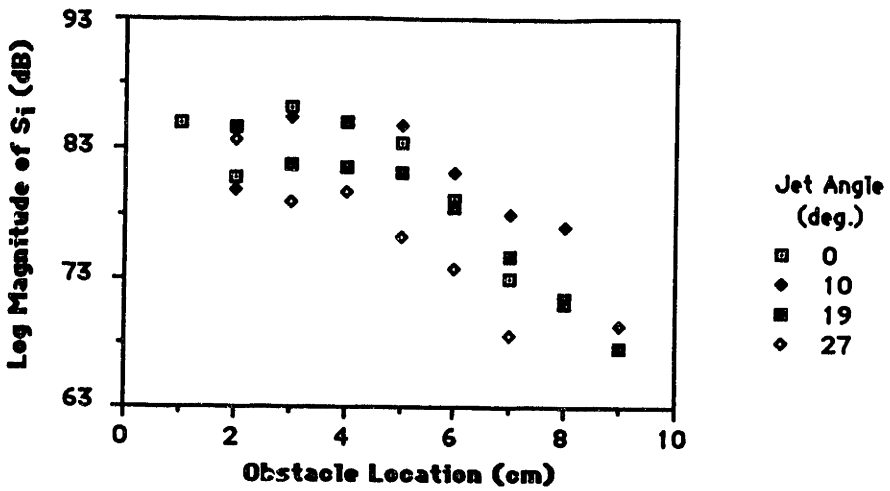

Figure 3.14 Source energy density at F1 versus the distance from the source to the inlet of the tube for several jet angles.

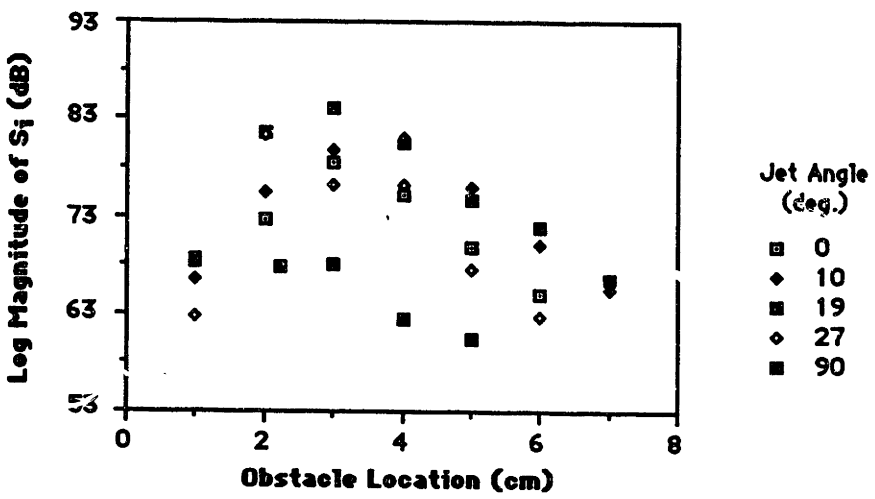

Figure 3.15 Source energy density at F2 versus the distance from the source to the inlet of the tube for several jet angles.

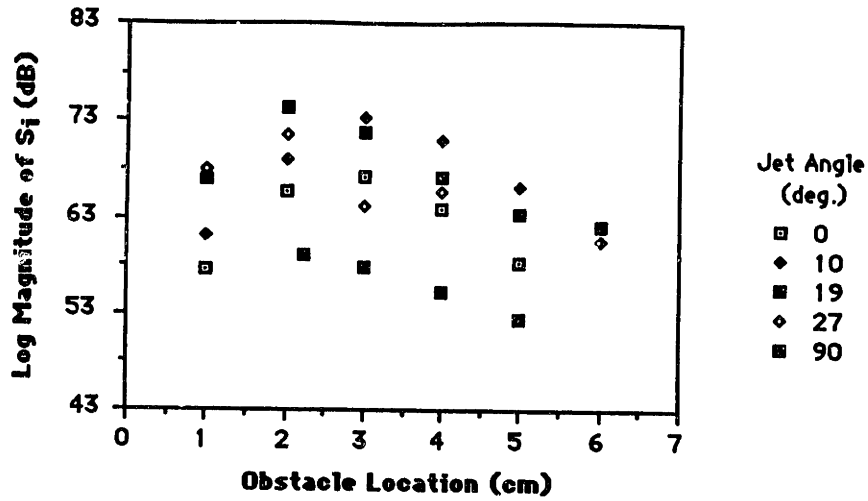

Figure 3.16 Source energy density at F3 versus the distance from the source to the inlet of the tube for several jet angles.

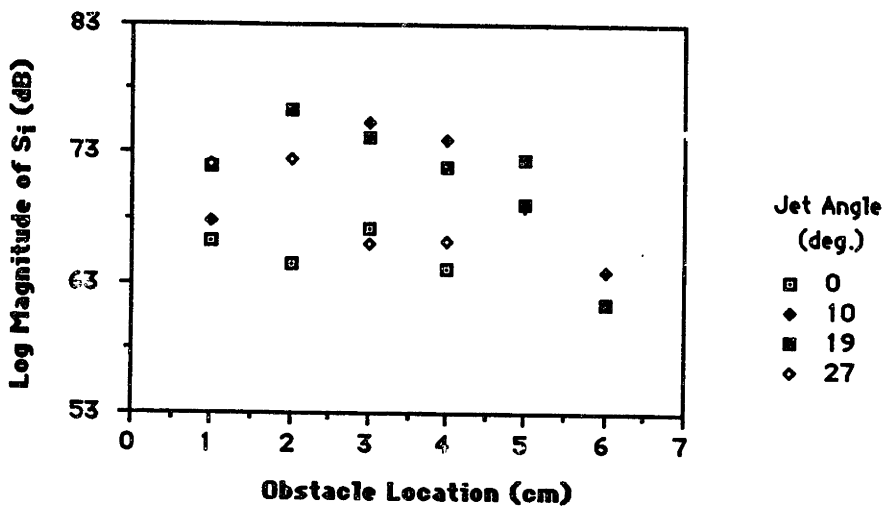

Figure 3.17 Source energy density at F4 versus the distance from the source to the inlet of the tube for several jet angles.

Chapter 4
/h/-like Sound Spectra

4.1 The Speech Sound /h/

The speech sound /h/ is produced by turbulent noise sources in the vicinity of the glottis. When the sound is created in this way, the resulting noise is called aspiration noise. The anatomy of the glottal region determines the air flow pattern, and hence provides a guide in determining the distribution of sources resulting from turbulent air flow. During aspiration, the glottis is more open than during the production of frication noise at a supraglottal constriction. Most fricatives have articulatory configurations with relatively narrow constrictions. The area function of the tract in front of the constriction then shapes the sound. /h/ sounds result from articulatory configurations with relatively wider glottal openings and there is often more than one source location in the vocal tract. The formant locations depend on the entire vocal tract [Fant,1960; Stevens,1987]. A close look at the vocal tract anatomy near the glottis reveals structural details that are relevant to estimating the sources.

The anatomy of the vocal tract is shown in figure 1.12. The glottis does not, of course, have a perfectly circular opening leading into a smooth straight tube. There are several obstacles to air flow within 4 cm of the opening. The epiglottis is angled relative to a line drawn perpendicular to the glottal slit. The base of the epiglottis creates an obstruction to the flow. On either side of the vocal folds are the vestibular folds or false vocal folds and the aryepiglottic folds. They are located above and lateral to the vocal folds. The vocal tract area near the glottis can be changed to some extent by contraction of the constrictor muscles surrounding the pharyngeal wall. Air flow impinging on the epiglottis, vestibular and aryepiglottic folds, and pharyngeal wall can create additional noise sources.

The spectral characteristics of /h/ result from the spectrum of the turbulent noise source and the filtering by of the vocal tract. /h/ sounds are generally produced with the vocal tract in the articulatory configuration for the following vowel [Fant, 1960]. Coupling to the subglottal impedance through the glottal opening causes acoustic loss in the first and second formants. The loss becomes smaller for higher frequencies because of the increased inductive component of the glottal impedance at higher frequencies [Stevens, 1987] . The amplitude of the first formant peak is reduced since the noise sources are located near the glottis, and because the first formant has a wide bandwidth. As described in Ch. 1, a sound pressure source located near the closed end of a tube will not couple well to the first mode [Stevens, 1987]. In general, the spectrum of /h/ is weak in intensity

especially in the first formant region, due in part to the absence of any pronounced obstacle to the flow, high frequency attenuation due to turbulence decay and low frequency reduction due to source location in the vocal tract.

4.2 Calculation of /h/-like Spectrum

The source spectra determined in Ch. 3 were used as a starting point in calculating the radiated sound pressure spectrum for a possible distribution of point sources during the production of the speech sound /h/ preceding /ʌ/ or /ə/. There were three major points of consideration and several approximations in the calculation of the spectrum of /h/. The first consideration was how to model the anatomy near the glottal opening. A single angle was chosen to characterize the jet impingement. The angle the epiglottis makes with a line perpendicular to the glottal slit is in the range of 25° to 45° and depends on the speaker and the following vowel. The 27° source spectra were chosen to represent the spectra of pressure sources produced on impingement with the base of the epiglottis. The tissue folds near the glottis are not located directly in the jet path and were not specifically dealt with here. There is no doubt that some turbulent flow interacts with the vestibular and aryepiglottic folds, but the sources will be weak compared to those produced by the impact on the surface of the impinging jet. The interactions may be of the same sort as the flow interactions with tube walls not in the immediate area of actual impingement.

Generally, turbulent jet flow is difficult to characterize and particularly so for complicated flow and nozzle geometries. The next consideration was how to model the glottal opening and the glottal jet. Two possible jet geometries were considered: a round jet with circular nozzle and a planar jet with an infinitely long slit for a nozzle. The glottal opening is not circular, but nevertheless, it was modeled by a circular opening, and thus the glottal jet was modeled as a round jet. The finite geometry of the round nozzle was deemed to be a more appropriate model of the glottal opening than the finite width infinite slit for several reasons. The geometry and symmetry of the vocal tract are more similar to those of a round jet than those of a planar jet. During aspiration, the aspect ratio of the glottal opening (length to width) is not large enough to allow one to consider the glottal opening to be an infinitely long slit. The planar jet description does not allow characterization of interactions between the air flow at the ends of the glottal opening and anatomical features near the glottis.

Figure 4.1 shows a schematic representation of the jet opening and impingement zone. The narrowest jet dimension is perpendicular to the vestibular and aryepiglottic folds described above and therefore reduces their involvement in source production.

Approximate dimensions of the glottal region of an adult male are shown in figure 4.2 [Diehl, 1968; Fink, 1975]. Enough space for a small recirculation zone must be retained anterior and superior to the jet. Impingement occurs before the jet has grown appreciably laterally. The distance between the glottal opening and the epiglottis is about five nozzle diameters in length, which is slightly larger than the core length. The downstream wall jet is directed around the base of the epiglottis and aligned with the axis of the vocal tract. The wall jet flows along the epiglottis due to the convex curvature of its base. Thus the jet travels farther along the epiglottis before separation than it would if the vocal tract had continued straight. A distributed source from approximately 1 to 4 cm above the glottis is created. Upon separation from the epiglottis, the flow may interact with the anterior pharyngeal wall producing an additional source region farther down the tube.

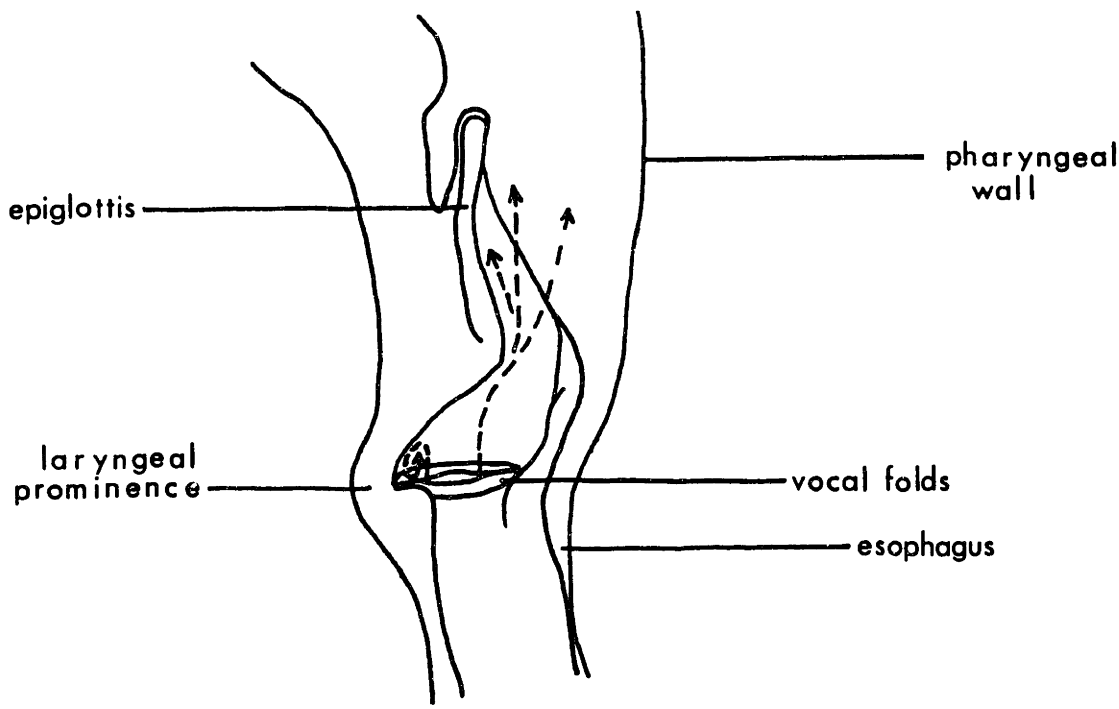

Figure 4.1 The glottal jet is shown superimposed on a sagittal view of the larynx.

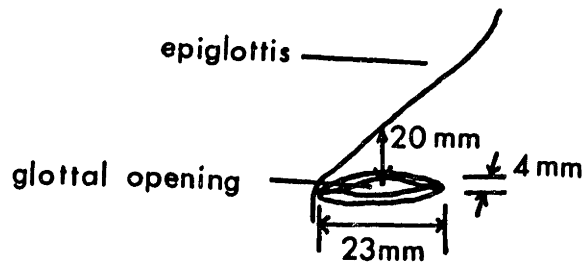

Figure 4.2 Dimensions of the glottal region of an adult male [Diehl, 1968; Fink, 1975].

The individual source spectra for jet angle 27° and obstacle locations 1, 2, 3 and 4 cm were used to model the pressure source spectra at different points in the distributed source. The smooth curves used in these calculations are shown in figure 4.3. The SPL scale in figure 4.3 is the absolute SPL recorded during the annular obstacle experiments. The annular obstacle intensified the sound produced when it was present in the tube, and hence, the scale represents only relative spectral amplitudes of pressure sources located at different positions in the tube or tract if no annular obstacle is present. Radiated SPL spectra were found by reversing the calculations described in Ch. 2. The flow rate and glottal area used in the calculations were 442 cm^3/sec and 0.114 cm^2. The transfer functions from pressure source to radiated sound pressure 26 cm from the mouth of the tube derived in section 3.2 were used to calculate radiated sound pressure due to the sound pressure sources, which are shown in figure 4.4. p^2 was calculated for each location, summed and converted to dB re 20 µPa. The resulting SPL spectrum is in figure 4.5.

The absolute SPL of source spectra formed in the glottis region during /h/ sound production is not necessarily the same as that produced in the experimental obstacle models. The exact level is unknown. The curves in figure 4.3 are plotted from 500 Hz to 6000 Hz. For frequencies lower than 750 Hz, the experimentally determined source spectra are inaccurate. No data points are taken below 500 Hz and external noise sources were largest below 350 Hz. Thus, the first formant is not reliably portrayed by the radiated pressure curves calculated above.

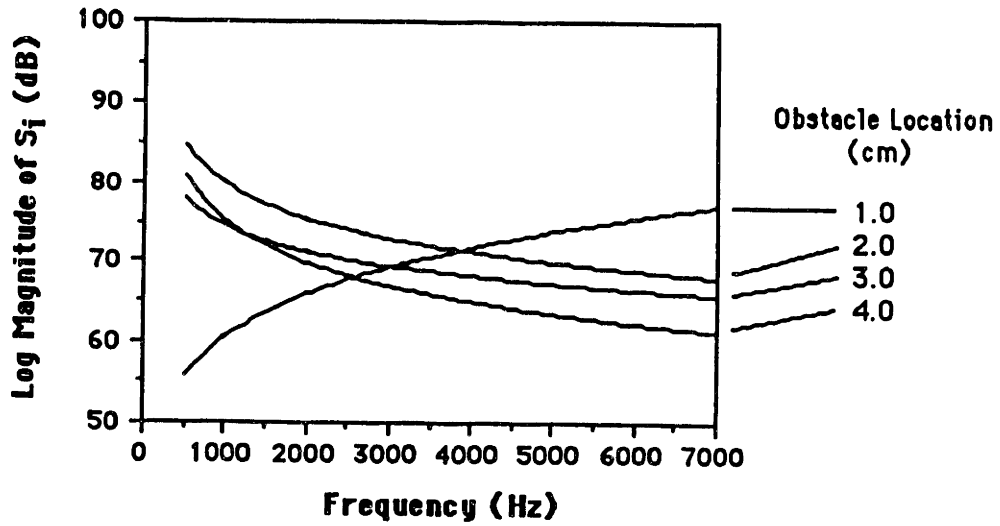

Figure 4.3 Modeled Source Spectra. Smoothed curves are shown for point sources used to model the distributed line source in /h/-like sounds.

4.3 Discussion

The spectrum in figure 4.5 is similar to that derived by Stevens using a distributed source located in the first 5 cm of a straight tube and source spectra modeled from pressure source spectra experimentally derived by Shadle [Stevens, 1987; Shadle, 1985]. In both radiated sound pressure spectra, the formants are evenly spaced about 1000 Hz apart. Stevens' spectrum has slightly different SPL amplitudes at the formant frequencies partially due to larger formant bandwidths. SPL amplitudes of the troughs between the first four formants are approximately the same [Stevens, 1987]. Stevens' spectrum begins to fall off at about 4000 Hz. The calculated spectrum in figure 4.5 begins to decrease above 5000 Hz.

The spectrum pictured in figure 4.5 has the general characteristics of the spectrum of the speech sound /h/, which were described in section 4.1. The resonant structure of the calculated spectrum resembles that of the intended preceding vowel (/ʌ/ or /ə/).The uniform vocal tract used in the calculations is the approximate articulatory configuration of vowels /ʌ/ or /ə/. The values of the spectrum near the first formant are not accurate enough to allow a detailed discussion of the first formant. However, the relative amplitude of the first formant is significantly less than that of the next five formants as shown in figure 4.5. The speech sound /h/ has a weak absolute level compared to that of strong fricatives such as /s/ or /ʃ/. The annular obstacle was used to amplify the sound produced by pressure sources in a small region of the tube. The absolute SPL of the pressure sources produced there with no obstacle is unknown. The SPL of the calculated spectrum of an /h/

like sound can not be greater than that calculated using the amplified source spectra. Thus, the relative magnitude scale in figure 4.5 represents an upper limit in SPL amplitude. The calculated spectrum of the speech sound /h/ is weak compared to the overall SPL of speech. In summary, the source spectra experimentally determined earlier can be used to approximate the turbulence noise sources produced during speech.

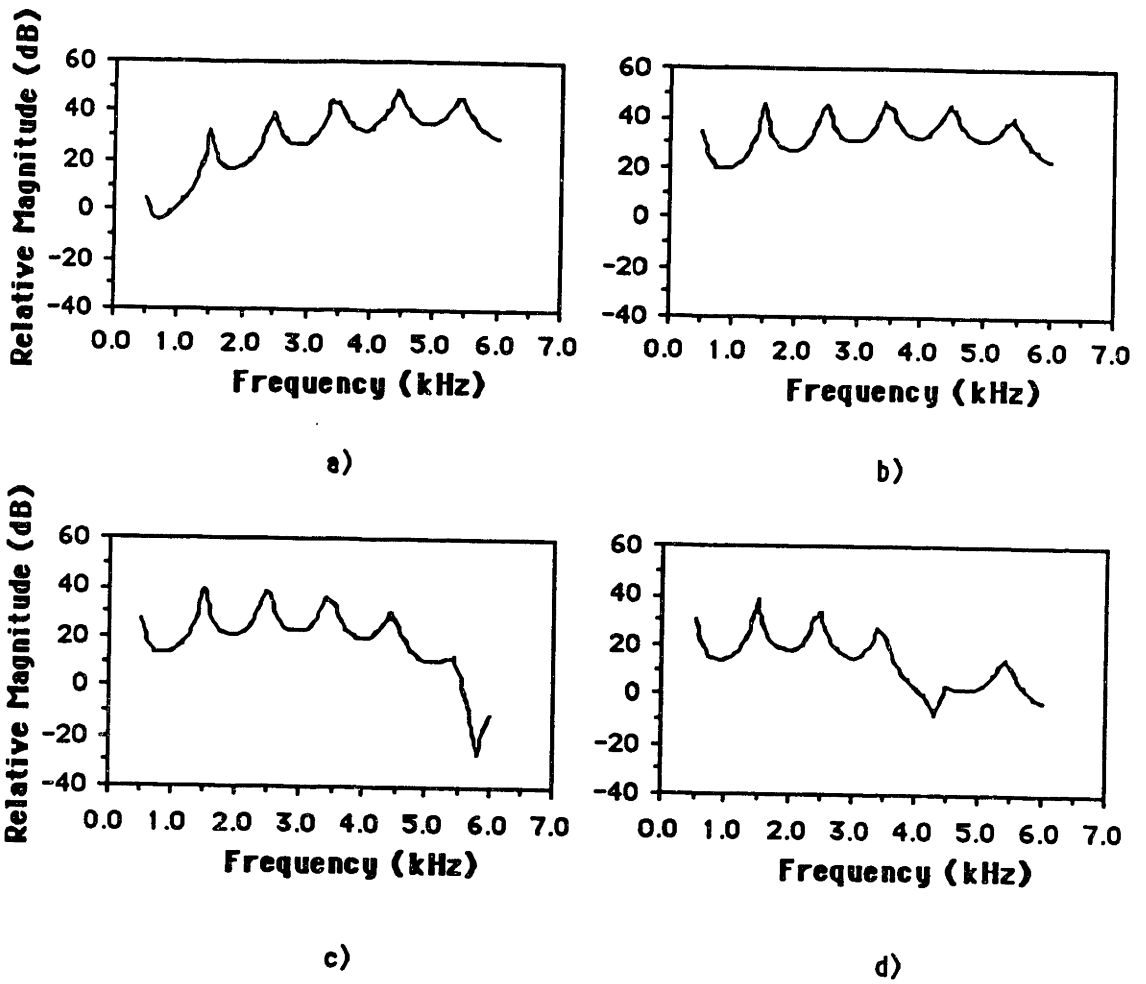

Figure 4.4 Radiated sound pressure with a 1 Hz bandwidth versus frequency due to pressure sources located at different axial positions along the tract. a) is located 1.0 cm, b) is located 2.0 cm, c) is located 3.0 cm, and d) is located 4.0 cm from the glottal opening.

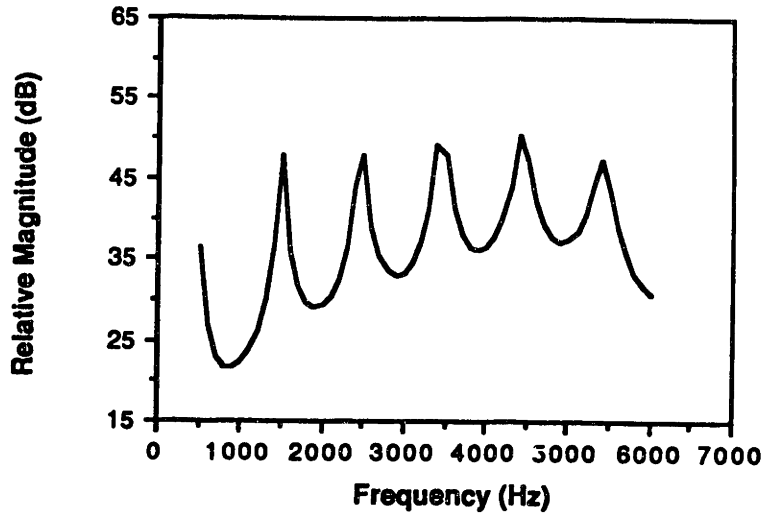

Figure 4.5 /h/-like spectrum of the radiated sound pressure 26 cm from the mouth of the tract. The amplitude is relative since the overall SPL of the pressure sources producing the sound is not known. The scale is consistent with that of the source spectra produced at the annular obstacle and used to estimate the pressure sources and with a 1 Hz bandwidth.

Chapter 5
Conclusions

In Chapters 2, 3 and 4, the turbulent noise sources created by an impinging jet in a tube have been investigated. A small obstacle was used to amplify the sound pressure produced by fluctuating shear forces at the tube walls. Source spectra were determined from the radiated sound pressure and these were used to calculate the spectrum of a /h/-like sound followed by /ɴ/ and /ə /.

In the future, work needs to be done in specifying the appropriate locations of turbulence noise sources in the vocal tract for /h/ sounds preceded by different vowels and other fricative speech sounds which do not have a single well defined obstacle in their vocal tract configuration. For instance, /x/ is produced by air from a posterior constriction hitting the wall of the vocal tract in the vicinity of the major bend in the tract. In this case, more of the dipoles produced are oriented with the flow and consequently the radiated sound has a greater amplitude than it would have been with a straight tract, but the dipoles are spread throughout a region in the vocal tract. It is important to understand which anatomical features are involved in sound source creation and how the air flow interacts with them. It may be possible to apply experimental methods from fluid dynamics to visualize the flow in a particular configuration of the vocal tract. For instance, the flow produced during the production of the speech sound /x/ might be made visible by adding smoke to the air flow through a glass tube appropriately shaped in the articulatory configuration of the vocal tract during the production of /x/. Visualizing the turbulent flow in the vocal tract would provide information on the structure of the turbulent flow and the location of points of attachment and separation in the flow. For instance, visualization of a jet impinging on the vocal tract wall would give information on where the resulting wall jet separates from the wall of the tract.

A monopole sound source may be present in the vocal tract during frication and aspiration. A noise monopole located at the glottal opening may contribute significant sound pressure especially during aspiration. The presence and contribution of such a source needs to be considered in modeling aspiration of healthy speakers as well as that of impaired speakers.

Future research should include study of pressure sources produced under transient flow conditions. This paper dealt with pressure sources produced by air flow with constant mean volume velocity.

Pressure source spectra have been experimentally determined for some flow conditions and vocal tract models as described in this paper and by Shadle (1985). More research needs to be done in this area. Direct measurements of sound pressure sources using pressure or flow probes in the vocal tract or models might be made, as well as estimates of coherence between different sources in the tract or tube. From knowledge of the spectral shape and overall SPL of pressure sources located at various points in the vocal tract during production of a certain fricative, the radiated sound pressure of that speech sound at a specific distance from the mouth of the vocal tract can be estimated and compared with the radiated sound pressure produced by a human uttering the fricative. From these sorts of experiments, the mechanisms of frication and aspiration can be discerned.

Appendix A
Calibration Set-ups and Curves

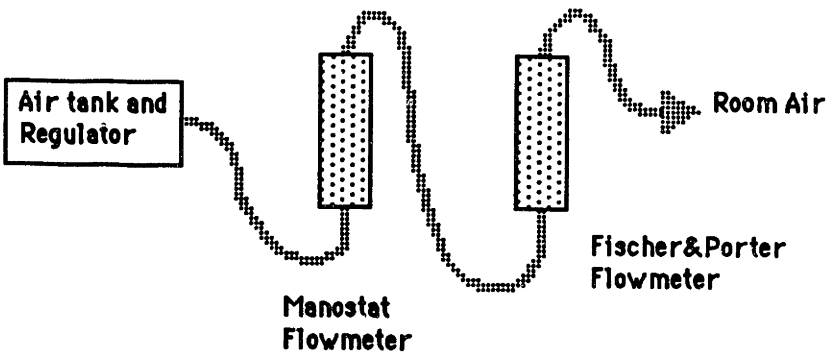

Figure A.1 a) Flowmeter circuit for calibration.

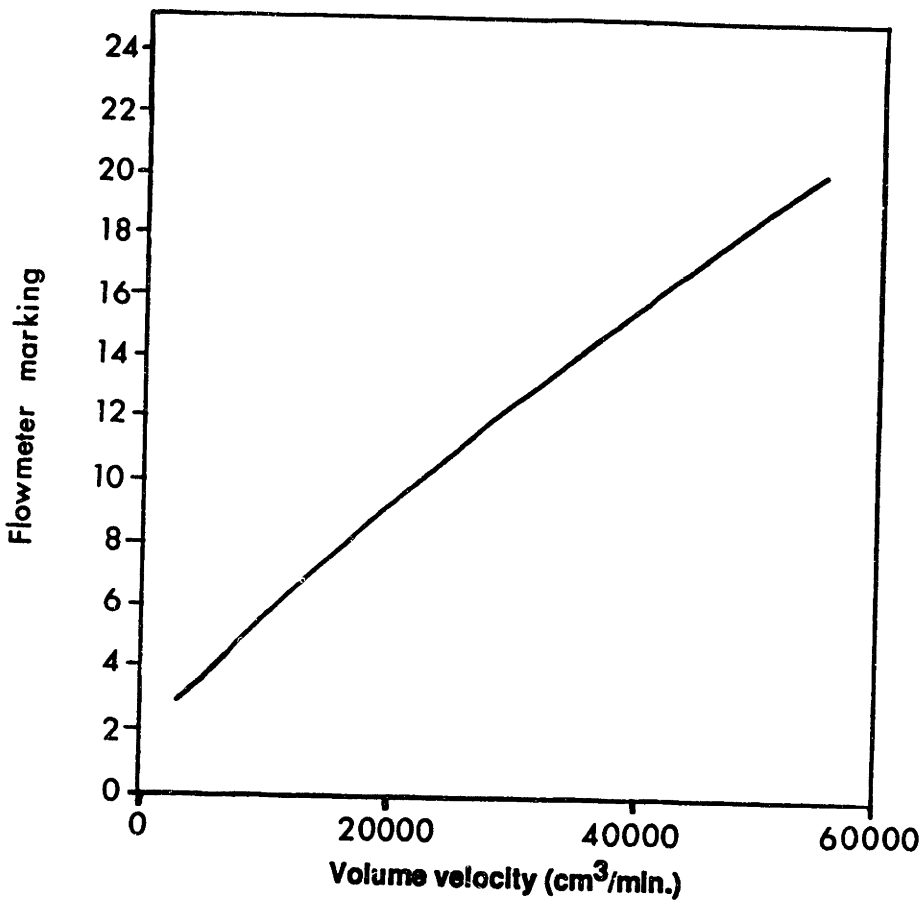

Figure A.1 b) Calibration curve for Manostat flowmeter (cat. no. 36-541-31 with 3/8" steel ball) determined with the experimental set-up in a).

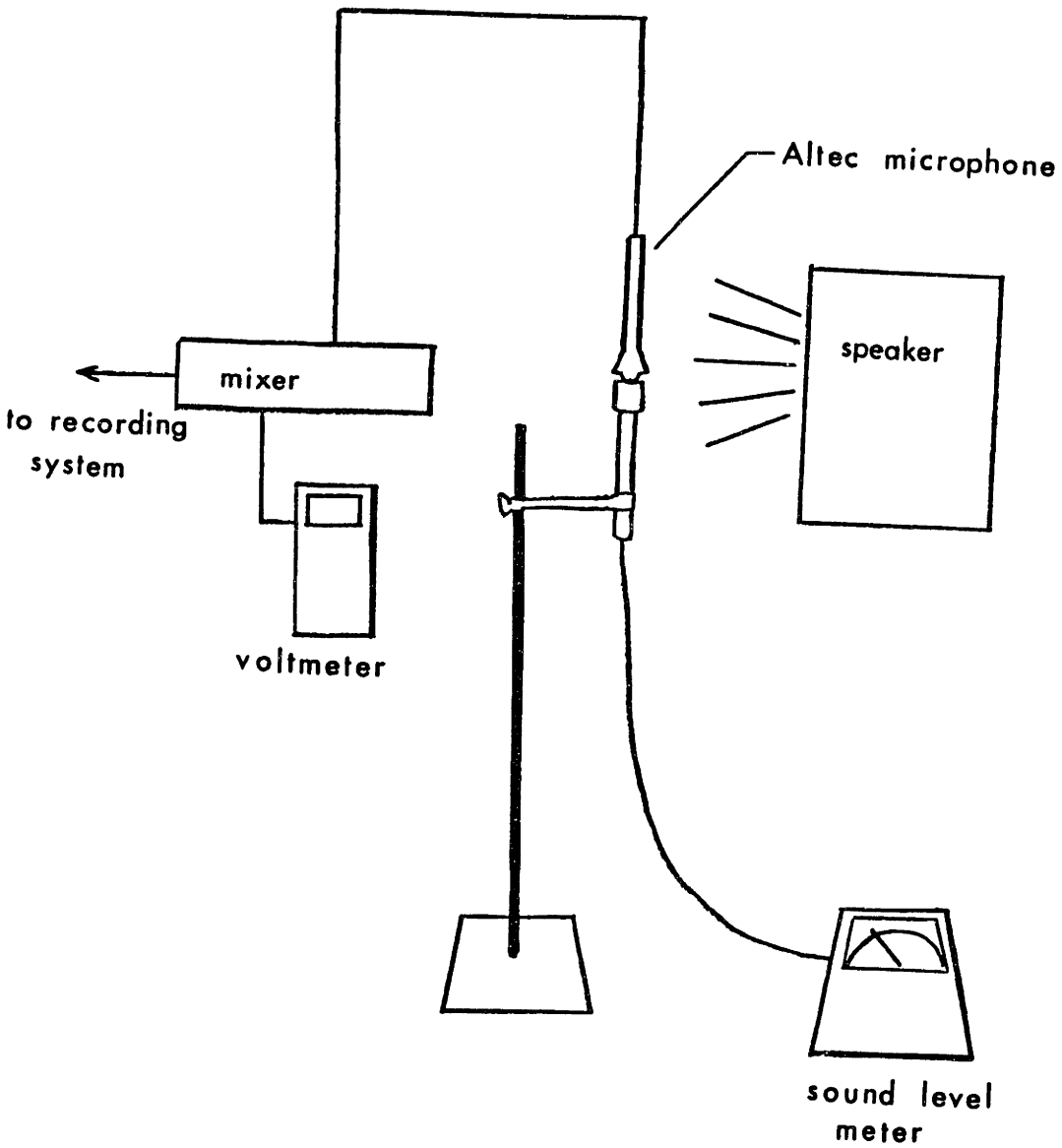

Figure A.2 Schematic of the system and microphone/mixer calibration set-up.

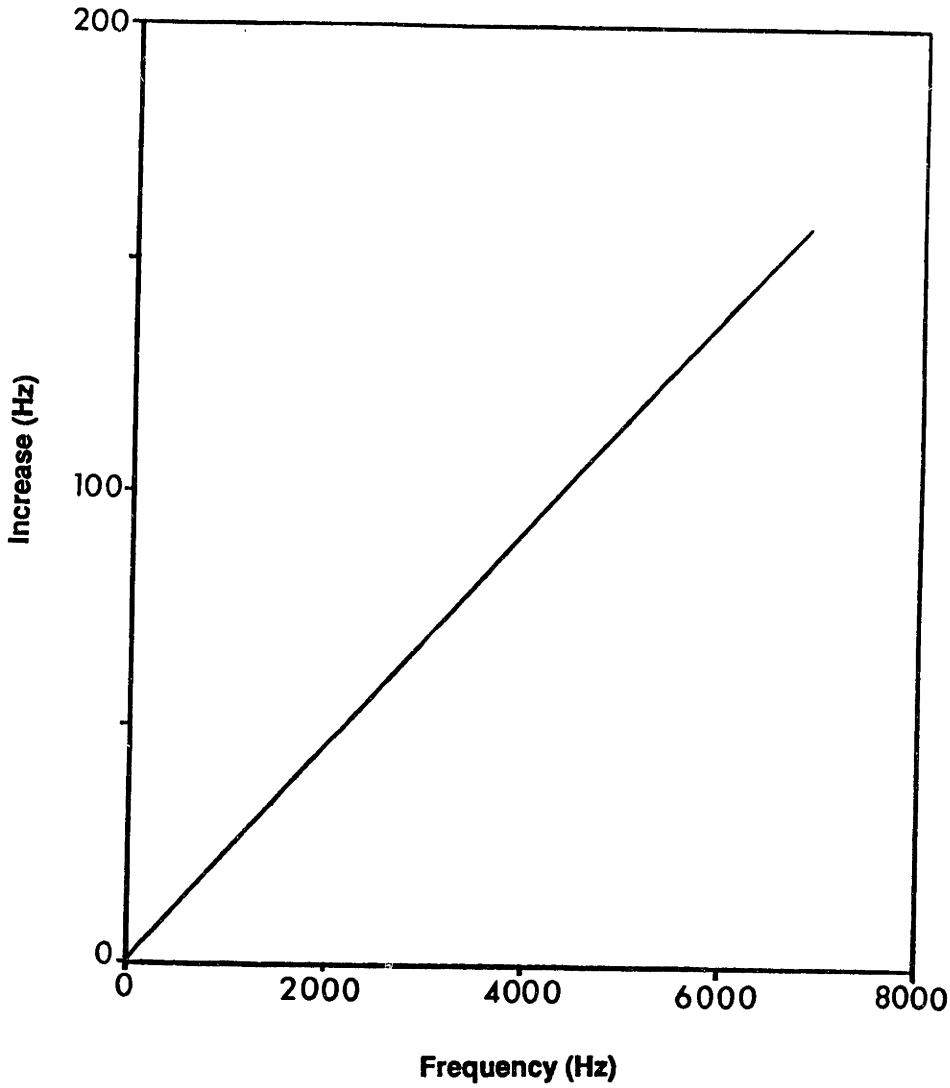

Figure A.3 The relationship between tone frequencies recorded on the Yamaha K-1000 tape deck and played back on the Nakamichi LX-5 tape deck. The frequency discrepancy is due to inaccurate head speed.

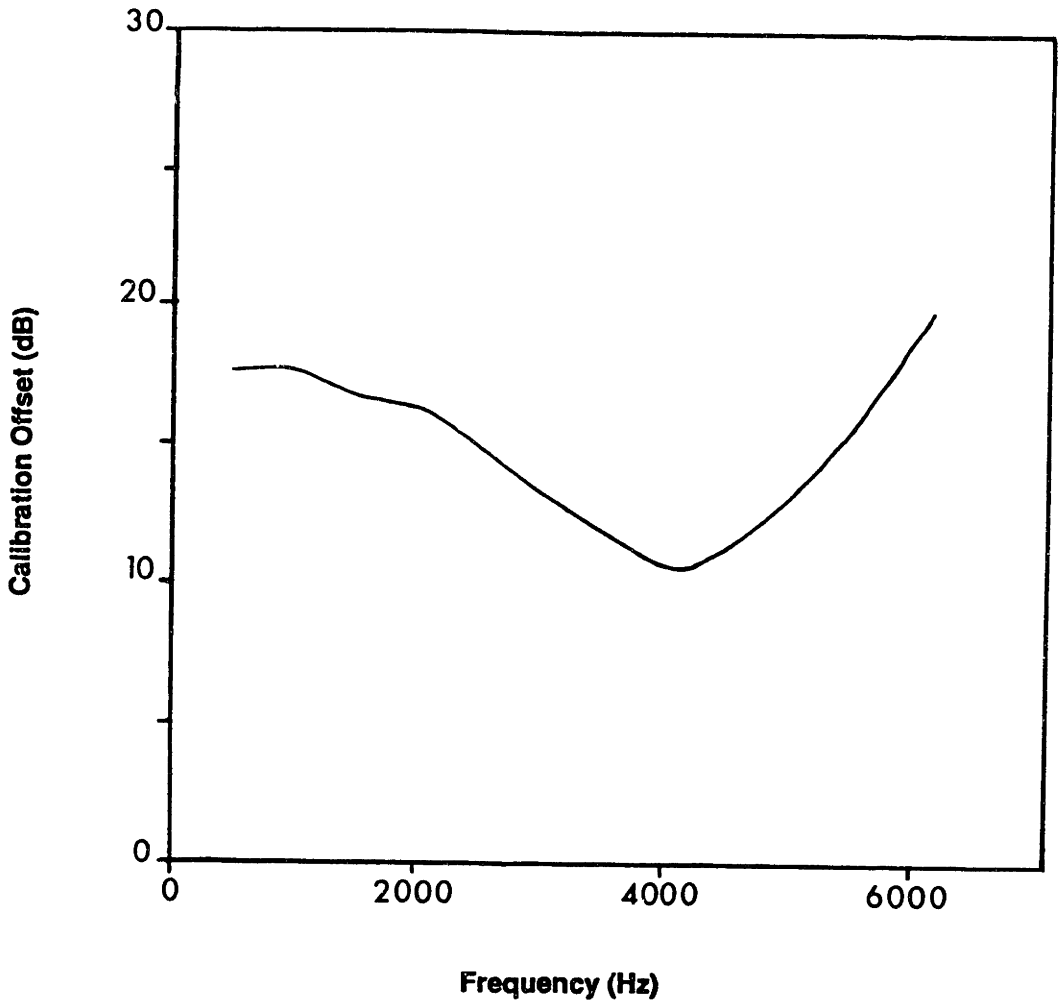

Figure A.4 The system offset curve. The above curve indicates the number of dB offset versus frequency it is necessary to add to the radiated sound pressure spectra calculated by KLSPEC from sound recorded by the recording system described in this paper. The shape of the highpass filter near its cut off frequency was not included in the curve, though a 1.5 dB drop over the filter at all frequencies was. The curve was determined using the recording set-up shown in figure A.2.

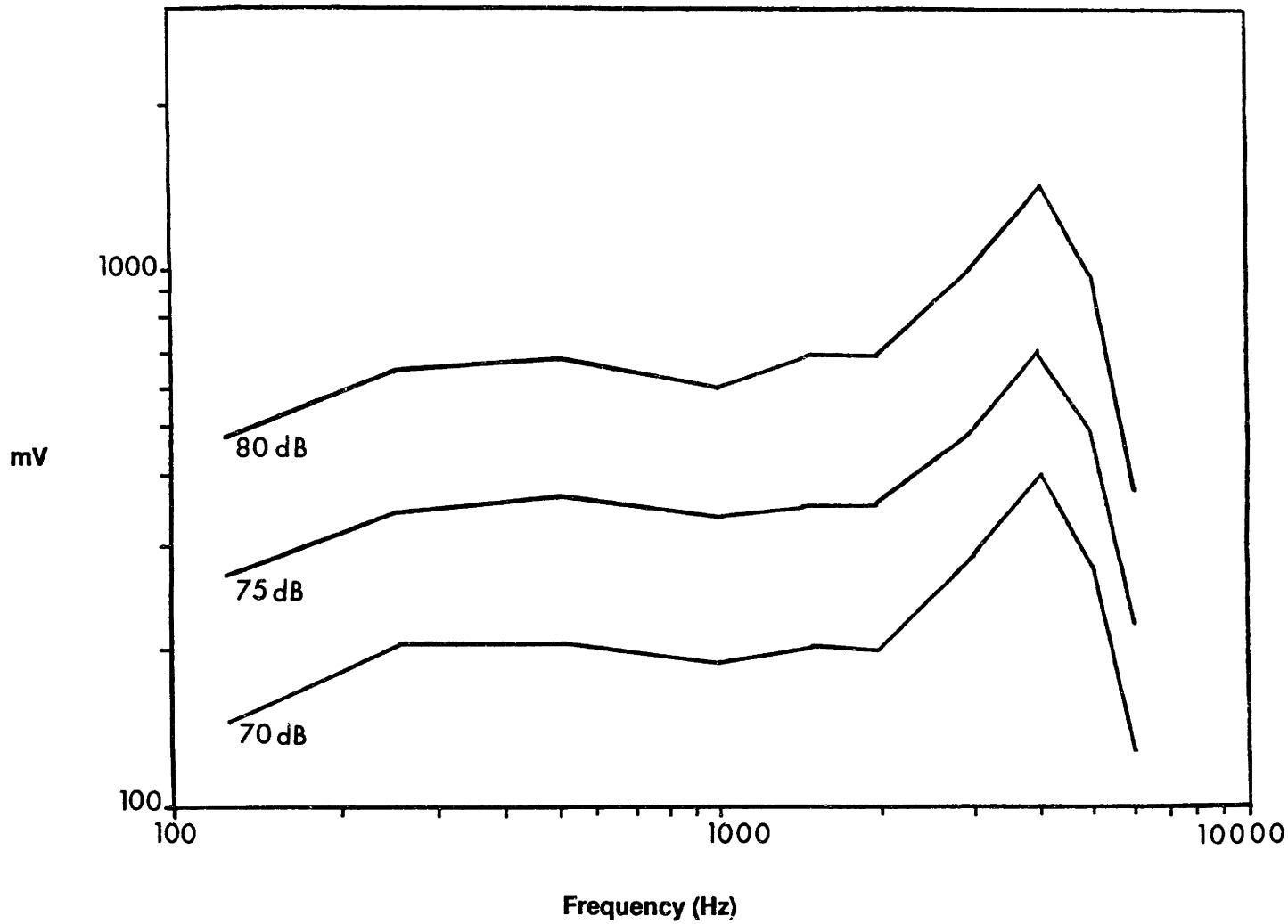

Figure A.5 The frequency response of the microphone and mixer. It was determined using the set-up pictured in figure A.2.

Appendix B
Tables of Data, Transfer Functions and Source Spectra

Table B.1 Corrected data, 0° jet models, magnitude (dB SPL in 50 Hz bins)

Obstacle Location(cm)	F1	F2	F3	F4	F5	F6
1	45.10	51.10	45.40	50.10	45.00	39.00
2	45.80	55.90	54.30	54.10	46.40	37.10
3	52.10	62.80	56.20	53.90	44.00	37.20
4	52.80	61.30	52.80	46.90	40.90	38.60
5	53.50	57.70	47.00	42.10	43.00	37.80
6	50.80	54.60	43.50	44.30	40.90	36.40
7	47.10	52.40	44.30	42.00	40.40	37.20
8	46.60	51.30	43.10	40.80	40.60	35.80
9	44.70	49.80	43.60	41.50	42.20	35.60
10	44.30	50.30	44.30	43.40	40.50	37.00
11	44.50	51.50	44.30	41.40	41.60	37.10
12	44.50	51.50	43.90	41.50	41.30	36.70
13	44.10	50.20	44.90	41.20	41.80	36.60
14	42.80	50.20	44.30	42.10	41.50	36.40
15	43.30	49.80	43.70	42.80	41.30	35.80
16	42.20	49.60	43.90	41.90	40.90	37.50
none	43.00	49.10	43.30	41.90	40.00	36.70

Table B.2 Corrected data, 10° jet models, magnitude (dB SPL in 50 Hz bins)

Obstacle Location(cm)	F1	F2	F3	F4	F5	F6
1	41.70	50.80	46.90	51.50	48.40	42.00
2	45.10	58.10	57.30	61.80	54.10	47.70
3	51.30	64.00	62.20	61.90	53.90	38.40
4	52.90	66.80	59.40	55.40	43.50	46.00
5	54.70	63.20	52.60	41.90	45.70	41.90
6	52.50	58.30	46.90	46.80	43.90	36.00
7	50.60	54.50	44.40	43.70	41.80	36.40
8	50.20	51.50	44.10	43.00	41.90	35.80
9	45.90	51.50	43.50	41.90	42.60	35.10
10	44.30	50.30	42.30	42.10	42.20	35.10
11	42.20	50.20	43.50	41.50	41.80	34.70
12	43.60	49.90	43.30	41.80	41.50	34.40
13	41.70	49.90	44.80	40.30	42.20	35.80
14	42.80	49.80	44.20	41.00	42.60	34.90
15	41.70	51.10	44.30	42.10	41.50	34.40
16	42.00	50.30	44.90	42.40	40.90	35.20
none	44.60	49.60	45.20	42.30	41.80	34.50

Table B.3 Corrected data, 19° jet models, magnitude (dB SPL in 50 Hz bins)

Obstacle Location(cm)	F1	F2	F3	F4	F5	F6
1	40.30	51.40	50.50	55.40	53.90	52.10
2	47.10	63.80	62.70	65.70	61.50	55.80
3	47.80	68.40	60.70	60.80	53.00	39.40
4	49.50	66.30	55.80	53.30	43.40	43.80
5	51.20	62.00	50.50	40.60	46.10	41.70
6	49.80	60.00	47.80	44.60	43.90	37.40
7	47.40	55.30	46.50	41.50	41.30	36.90
8	45.20	52.10	45.30	39.00	42.00	35.80
9	43.90	51.80	45.30	39.30	41.70	36.70
10	39.50	50.80	44.40	39.80	41.40	37.00
11	40.20	50.60	43.90	40.80	41.30	36.40
12	40.50	49.90	44.70	40.30	41.50	35.60
13	40.30	50.00	45.50	39.40	40.60	35.60
14	40.30	49.60	46.10	39.90	40.70	36.90
15	39.80	51.00	45.30	40.60	43.10	37.20
16	40.00	50.90	44.10	40.20	42.60	38.10
none	40.90	50.80	44.20	39.70	41.70	36.10

Table B.4 Corrected data, 27° jet models, magnitude (dB SPL in 50 Hz bins)

Obstacle Location(cm)	F1	F2	F3	F4	F5	F6
1	39.30	50.60	51.10	55.60	53.90	51.70
2	46.30	63.50	59.80	61.80	58.20	53.20
3	45.60	60.80	53.40	52.60	47.70	39.30
4	47.90	62.30	54.30	48.00	44.10	39.90
5	46.80	55.90	44.60	40.50	42.50	37.20
6	45.90	53.30	43.90	40.70	41.40	36.90
7	43.20	51.10	44.40	39.30	42.40	37.20
8	41.50	50.80	43.90	39.20	42.50	37.10
9	40.10	50.70	43.10	40.50	42.20	36.80
10	40.00	49.90	42.60	40.20	40.90	36.80
11	40.80	49.30	43.70	39.80	42.20	37.70
12	40.60	49.70	44.30	39.30	42.80	36.80
13	39.90	50.80	43.30	38.90	42.50	37.20
14	39.50	49.90	45.30	40.20	42.20	37.20
15	39.60	49.90	43.70	41.30	44.00	37.60
16	39.60	50.30	42.90	40.40	42.60	38.60
none	40.60	51.20	44.70	39.20	43.70	36.70

Table B.5 Corrected data, 90° jet models, magnitude (dB SPL in 50 Hz bins)

Obstacle Location(cm)	F1	F2	F3	F4	F5	F6
2.25	43.90	51.90	48.30	48.00	44.90	40.40
3	42.50	53.40	47.60	46.70	41.00	31.80
4	42.80	50.90	45.50	40.50	35.60	31.60
5	42.50	50.50	43.10	37.80	35.40	29.20
6	41.80	50.00	43.50	39.30	35.30	27.90
7	43.20	49.30	42.70	38.40	34.10	29.00
8	41.60	48.70	42.60	37.10	34.30	27.90
9	40.00	49.00	41.60	36.70	34.80	27.70
10	41.70	49.30	41.40	38.00	33.90	27.90
11	40.20	49.10	41.00	38.00	33.40	28.60
12	39.30	46.80	41.50	38.20	34.30	28.10
13	39.30	48.30	41.80	38.20	35.20	28.60
14	39.10	48.10	42.10	38.00	33.40	28.80
15	40.90	47.20	41.60	37.60	34.20	29.00
16	39.70	47.40	40.10	36.70	33.90	28.60
none	41.20	47.80	41.00	37.90	34.10	27.60

Table B.6 Log magnitude $|T_i'(f)|$ (dB)

Obstacle Location(cm)	F1	F2	F3	F4	F5	F6
1	21.3	22.9	20.3	15.6	10.0	1.9
2	21.3	22.9	20.3	15.6	10.0	1.9
3	21.5	21.5	17.3	9.3	-2.3	-22.9
4	21.1	20.7	14.3	1.5	-26.0	-17.7
5	21.4	20.0	9.9	-22.1	-9.4	-19.2
6	21.1	18.9	5.2	-1.9	-5.1	-24.1
7	20.8	17.1	-15.9	0.6	-11.9	-24.1
8	20.2	14.4	-0.1	-1.0	-25.1	-20.2
9	20.5	12.1	5.1	-4.1	-10.6	-23.9
10	20.4	7.6	6.0	-21.6	-11.0	-28.8
11	20.1	0.2	5.5	-7.7	-16.9	-20.7
12	19.4	-8.5	3.2	-3.8	-23.4	-24.1
13	19.2	1.7	-2.1	-3.8	-13.8	-32.9
14	19.1	5.5	-15.8	-8.9	-13.1	-21.6
15	18.3	8.4	-4.6	-22.9	-18.6	-23.9
16	18.5	9.1	1.5	-10.6	-23.5	-35.0
none	21.[illegible]	22.9	20.3	15.6	10.0	1.9

Table B.7 Log magnitude source spectra, $|S_i(f)|$ (dB), 0° jet models (+17 dB offset)

Obstacle Location (cm)	F1	F2	F3	F4	F5	F6
1	101.9	85.2	74.6	83.1	77.7	74.9
2	97.7	89.6	82.7	81.5	73.8	
3	103.2	95.5	84.2	84.1	78.6	
4	101.9	92.2	81.0	81.0		
5	100.5	86.8	75.2	86.0		
6	96.0	82.1				
7	89.9					
8	88.4					

Table B.8 Log magnitude source spectra, $|S_i(f)|$ (dB), 10° jet models (+17 dB offset)

Obstacle Location (cm)	F1	F2	F3	F4	F5	F6
1	-	83.5	78.0	84.7	82.3	80.7
2	96.9	92.4	85.9	89.5	82.7	81.1
3	102.4	96.7	90.4	92.4	91.3	90.6
4	102.1	97.9	88.1	91.0	97.5	92.7
5	101.8	92.9	83.1	85.8	83.8	87.6
6	98.1	87.0	77.6	80.8		
7	94.9	82.4				
8	93.9					
9	86.3					

Table B.9 Log magnitude source spectra, $|S_i(f)|$ (dB), 19° jet models (+17 dB offset)

Obstacle Location (cm)	F1	F2	F3	F4	F5	F6
1	61.5	85.5	83.9	89.0	88.6	91.6
2	101.6	98.6	91.4	93.4	90.4	89.3
3	98.7	101.2	88.9	91.3	90.4	91.0
4	98.5	97.4	84.2	88.9	97.4	90.0
5	98.2	91.6	80.3	89.1	84.5	86.8
6	95.4	88.9	79.0	78.4		
7	91.6	83.5				
8	88.0					
9	84.6					

Table B.10 Log magnitude source spectra, $|S_i(f)|$ (dB), 27° jet models (+17 dB offset)

Obstacle Location (cm)	F1	F2	F3	F4	F5	F6
1	-	79.8	85.0	89.2	88.5	91.1
2	100.6	98.3	88.5	89.5	87.0	86.7
3	95.9	93.3	81.2	82.9	83.6	89.6
4	96.7	93.2	82.7	83.1		
5	93.2	84.4				
6	90.7	79.7				
7	85.5					

Table B.11 Log magnitude source spectra, $|S_i(f)|$ (dB), 90° jet models (+17 dB offset)

Obstacle Location (cm)	F1	F2	F3	F4	F5	F6
1	97.2	84.9	76.1	75.3	73.4	73.7
2		85.0	74.7	76.6	77.7	83.9
3		79.4	72.2	73.0	88.9	75.8
4		77.3	69.4			

Table B.12 Parameters of regression fits to source spectra data for $0^o, 10^o, 19^o$ and 27° jet models. The fits are of the form $y = a \cdot (\text{freq.})^b + \text{error}$. R is the regression coefficient.

Degrees	Obstacle Length (cm)	a	b	R
0	1	207.5596	-0.1494	0.90
	2	205.5459	-0.1469	0.96
	3	226.8351	-0.1523	0.97
	4	229.0199	-0.1580	0.97
	5	193.6249	-0.1389	0.80
10	2	140.1467	-0.0880	0.92
	3	126.3678	-0.0642	0.94
	4	112.0516	-0.0472	0.63
	5	149.3574	-0.0944	0.87
	6	196.9548	-0.1434	0.95
19	2	129.9454	-0.0676	0.94
	3	117.6350	-0.0557	0.75
	4	104.1958	-0.0415	0.47
	5	124.1414	-0.0718	0.74
	6	184.2711	-0.1352	0.96
27	2	143.7346	-0.0848	0.93
	3	117.2609	-0.0656	0.68
	4	157.5708	-0.1069	0.91

Bibliography

Abramovich, G.N., The Theory of Turbulent Jets. Cambridge: MIT Press, 1963.

Birkhoff, G. and Zarantonello, E.H., Jets, Wakes, and Cavities. New York: Academic Press, 1957.

Beranek, L.L., Acoustics. New York: American Institute of Physics, Inc., 1986.

Catford, J.C., Fundamental Problems in Phonetics. Bloomington: Indiana University Press, 1977.

Close, C.M., The Analysis of Linear Circuits. New York: Harcourt, Brace, and World,1966.

Diehl, C.F., Anatomy and Physiology of the Speech Mechanism. Springfield: Charles C. Thomas, 1968.

Donaldson, C. duP., Snedeker, R.S., and Margolis, D.P., "A Study of Free Jet Impingement.Part 2. Free Jet Turbulent Structure and Impingement Heat Transfer". J. Fluid Mech. 45, 477-512, 1971.

Dyer, I., Fundamentals and Applications of Underwater Sound. MIT 13.851 notes, January 1986.

Fant, G., Acoustic Theory of Speech Production. The Hague: Mouton, 1960.

Fink, B.R., The Human Larynx: A Functional Study. New York: Raven Press, 1975.

Flanagan, J.L., Speech Analysis Synthesis and Perception. New York: Springer-Verlag, 1972.

Fletcher, N.H. and Thwaites, S., "The Physics of Organ Pipes". Scientific American. 248(1) 94-103, 1983.

Fletcher, N.H. and Thwaites, S., "Wave Propagation on an Acoustically Perturbed Jet". Acustica 42, 323-334, 1979.

Hinze, J.O., Turbulence: An Introduction to Its Mechanism and Theory. New York: McGraw-Hill,1959.

Jakobson, R., Fant, C.G.M., and Halle, M., Preliminaries to Speech Analysis: The Distinctive Features and their Correlates. Cambridge: MIT Press, 1969.

Klatt, D.H., MIT Speechvax User's Guide. 1984.

Kuethe, A.M. and Chow, C., Foundations of Aerodynamics: Bases of Aerodynamic Design. New York: John Wiley and Sons, 1976.

Lange, N.A., Handbook of Chemistry. Sardusky: Handbook Publishers, 1949.

Martin, H., "Heat and Mass Transfer between Impinging Gas Jets and Solid Surfaces". In J.P. Hartnett and T.F. Irvine, Jr. (Eds.), Advances in Heat Transfer, New York: Academic Press, 1977, 1-59

Morse, P.M. and Ingard, K.U., Theoretical Acoustics. New York: McGraw-Hill Book Co., 1968.

Potter, J.L. and Fich, S. J., Theory of Networks and Lines. Englewood Cliffs: Prentice-Hall, 1963.

Rafferty, J. and Norling, R., "Cricket Graph: Presentation Graphics for Science and Business". Version 1.1. Philadelpia: Cricket Software, 1986.

Reynolds, A.J., Turbulent Flows in Engineering. New York: John Wiley and Sons, 1974.

Ribner, H.S., "The Generation of Sound by Turbulent Jets". Advan. Appl. Mech. 8, 103-182,1964.

Rodi, W., "A Review of Experimental Data of Uniform Density Free Turbulent Boundary Layers". In Launder, B.E.(Ed.), Studies in Convection: Theory, Measurement and Applications. New York: Academic Press, 1975, 79-165.

Rouse, H., Advanced Mechanics of Fluids. New York: John Wiley and Sons, 1959.

Russell, P.J. and Hatton, A.P., "Turbulent Flow Characteristics of an Impinging Jet". Proc. Instn. Mech. Engrs. Vol. 186(52/72), 635-644, 1972.

Shadle, C.H., The Acoustics of Fricative Consonants. MIT Technical Report 506, March 1985.

Staelin, D.H. and Kong, J.A., Electrodynamics. MIT 6.014 notes, January 1985.

Stahl, B. and Michalke, A., "On Noise Generated by Turbulence in a Pipe Downstream of a Discontinuous Area Enlargement". In Comte-Bellot, G. and Ffowcs William, J.E. (Eds.), Aero- and Hydro-Acoustics. New York: Springer-Verlag, 1985, 385-392.

Stevens, K.N., "Airflow and Turbulence Noise for Fricative and Stop Consonants: Static Considerations". JASA 50(4, Part 2), 1180-1192, 1971.

Stevens, K.N., Acoustic Phonetics. In preparation, 1987.

Stevens, K.N., "The Quantal Nature of Speech: Evidence from Articulatory-Acoustic Data". In Denes, P.B. and David, E.E. Jr. Eds., Human Communication: A Unified View. New York: McGraw-Hill, 1972, 51-66.

Streeter, V.L. Fluid Mechanics. New York: McGraw-Hill , 1962.

Thwaites, S. and Fletcher, N.H., "Wave Propagation on Turbulent Jets". Acustica 45, 175-179, 1980.

Thwaites, S. and Fletcher, N.H., "Wave Propagation on Turbulent Jets: II. Growth". Acustica 51, 44-49, 1982.